Studies of texture and mechanical properties of 6xxx automotive alloy extrusions

A thesis submitted for the degree of Doctor of Philosophy

by

Chrysoula Tzileroglou

BCAST

Department of Mechanical and Aerospace Engineering

Brunel University

January 2022

Abstract

The use of aluminium in the automotive industry has increased during the last decades, since aluminium alloys show some advantages compared to more traditional structural materials. Their light weight can result in a total vehicle weight reduction and enhance the reduction of CO_2 emissions and fuel consumption. Extrusion is a leading process for wrought aluminium alloys, capably to provide finished or semi-finished components.

The effect of preferred crystallographic orientation (texture) on rolled aluminium alloys has been widely studied, but there is limited literature on extruded materials. Moreover, since extrusion is a complex procedure, involving various parameters, there is still a lack of understanding of how these parameters affect texture and final mechanical properties. In this thesis a deeper understanding of this effect is attempted. An industrial high strength 6xxx aluminium alloy, provided by Constellium, was extruded and investigated. Microstructure and texture were studied with the use of EBSD, OIM and XRD. Mechanical properties were obtained by standard tensile testing.

Experimental results showed the role of extrusion speed and extrusion exit temperature. It was shown that the increase of speed, and furthermore the increase of exit temperature, increased the average grain size. The overall texture was not affected by the speed, but the changes of the amount of various texture component was noticed. The decrease of Cube and increase of S component resulted in an increase of 13 MPa in yield strength.

The effect of extrusion geometry on microstructure, texture and mechanical properties was found to be significant. Four profiles were chosen, a flat bar, a hollow rectangle, a round bar and a tow nut, based on their different extrusion ratios (ER). It was found that both microstructure and texture were grouped into two profiles with low ER (round bar and tow nut) and the two profiles with high ER (flat bar and hollow rectangle). The texture of the higher ER profiles resembled rolling texture with a combination of Brass, S and Cube components while for the lower ER profiles, the texture was reported Cu-Brass-Cube. Moreover, the mechanical properties followed the same division, with the strength of round bar and tow nut being higher than the other two.

To decouple the effect of geometry from that of ER, two investigations were introduced. An investigation of same geometry with various ER using different diameter of round bar was performed. Another investigation of similar ER with various geometries using

small/large round bar, flat bar and tow nut was performed. For the first investigation, it was discovered that the effect of ER on the three round bars was limited to small microstructural changes, while the overall texture remained the same. On the other hand, the comparison of different geometries with similar ER resulted in completely different microstructure and texture for the profiles with high ER. These differences were also reflected on the mechanical properties.

The investigation of a complex profile, a hollow rectangle with fins at the bottom, showed that observed strength differences from side to side are related to differences in crystallographic texture and grains morphology.

The effect of further thermomechanical treatment (aDA) after extrusion on texture was found to be limited and it was mainly resulted from the deformation part of the aDA.

Acknowledgement

I would like to thank my supervisor Prof. Isaac T.H Chang for providing me with the opportunity to pursue the PhD degree. I gratefully acknowledge the financial support from the ICASE PhD studentship provided by both the Engineering and Physical Sciences Research Council (EPSRC) and Constellium which enabled me to focus on my research.

I would also like to express my deepest gratitude towards my co-supervisor, Prof. Zhongyun Fan, for his guidance. I am indebted to Dr. Chamini Mendis whose experience and friendship were invaluable additions to my work.

To Dr. Carla Barbatti, for all the support and direction. I am also grateful for the opportunity to spend time at Constellium Technology Centre in Voreppe, France, for which I would like to thank Dr. Carla Barbatti and Philippe Bridot.

To Mr. Stephen Cook, Dr. Loredana Saccone, Ms. Sam Melvin and Mrs. Aneta Walsh for their guidance and assistance provided in the laboratories. Also, to Dr. Shohreh Khorsand, Dr. Susanna Venditti, Dr. Qing Cain, Dr. Ewan Lordan, Mr. Vincenzo DeStefano and Ms. Kyriaki Katikaridou who have accompanied me during this journey.

Finally, I would like to thank my family for all their unconditional love and support.

Publication list

[1] C. Tzileroglou, I.T.H. Chang, C.L. Mendis, C. Barbatti, S. Hogg, Z. Fan, The effect of die geometry on crystallographic texture of extruded 6xxx high strength aluminium alloy, Electron Backscatter Diffraction meeting 2019, National Physical Laboratory (2019)

[2] C. Tzileroglou, I.T.H. Chang, C.L. Mendis, C. Barbatti, M. Jarrett, Z. Fan, Role of extrusion speed of a 6xxx high strength aluminium alloy, TMS (2020)

[3] C. Tzileroglou, I.T.H. Chang, C.L. Mendis, Z. Fan, C. Barbatti, M. Jarrett, The effect of extrusion speed on a 6xxx high strength aluminium alloy, ICAA (2020)

ER	Extrusion ratio
SFE	Stacking fault energy
HAGB	High angle grain boundaries
LAGB	Low angle grain boundaries
GND	Geometrically necessary dislocations
OM	Optical microscope
SEM	Scanning electron microscopy
EBSD	Electron backscatter diffraction
FIB	Focused ion beam
TEM	Transmission electron microscope
ODF	Orientation distribution function
XRD	X-ray diffraction
FCC	Face-centred cubic
KAM	Kernel average misorientation
YS	Yield strength
UTS	Ultimate tensile strength
EL	Uniform elongation
GDRX	Geometric dynamic recrystallization
TMA	Thermomechanical processing
aDA	Pre-ageing, deformation, post-ageing
Cu	Copper
CTE	Columnar to equiaxed transition
d_c	Particle's critical diameter
C	Geometrical factor
σ_y	Yield strength
G	Shear modulus
b	Burgers vector
α	Form of alumina
DC	Direct chill casting
PCG	Peripheral coarse grain
AMCC	Advanced metal casting centre
IQ map	Image quality map
SDAS	Secondary dendrite arm spacing
GP zone	Guinier–Preston zone

Table of Contents

Chapter 1 Introduction

1.1 Background

Aluminium is a light metal with a density of 2.7 g/cm^3 and moderate strength, which varies between 40-700 MPa, depending on the alloying additions and the processing conditions. Its high strength to weight ratio makes it a metal with great opportunities for use and at the same time is fully recyclable and nontoxic. It has applications in packaging, containers, electrical conductors and household appliances [1]. Its durability and light weight make it the perfect candidate for many industries, such as aerospace, automotive and infrastructures. It is a material that can be processed in a variety of ways, with many possibilities of final surface finish. In addition to that, its natural oxide coating provides it with good corrosion resistance, which can be further enhanced with specific surface treatments [2-4].

In recent years, the use of aluminium in the automotive industry has increased, as shown in Fig. 1.1 and 1.2. Aluminium alloys have some advantages compared to more traditional structural materials, such as steel. Their light weight can result in a total vehicle weight reduction of up to 28% [5]. In an era with the trend of increasing number and size of vehicles, aluminium alloys can help to reduce CO_2 emissions and fuel consumption.

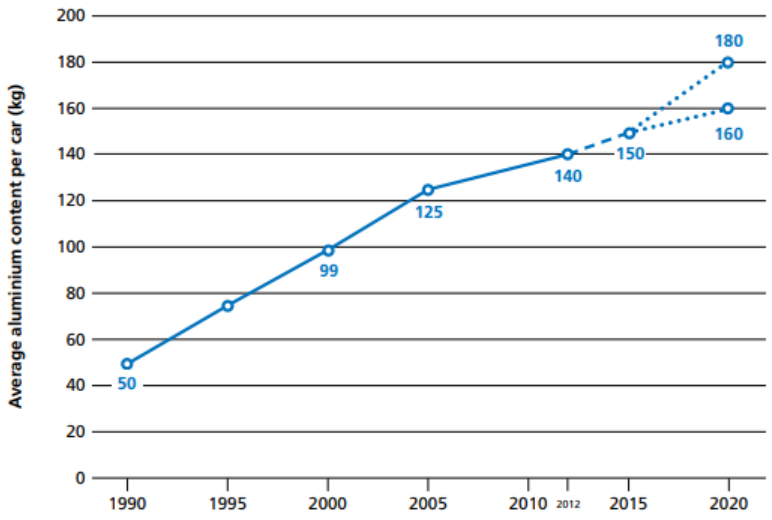

Fig 1.1 Evolution of average aluminium content per car produced in Europe [6].

System PPV	2016	2020	2022
Engines	110	104	103
Transmissions & Drivelines	83	85	86
Wheels	65	72	72
Heat Exchangers	32	30	30
Heat Shields	6	6	6
Suspensions/Cradles/Subframes	21	25	27
Steering Components	8	8	8
Brakes	8	8	8
Closures	41	59	62
CMS	7	9	11
Body Stamping	11	20	23
Other Body	14	28	31
All others	5	5	5
Total	***411***	***459***	***471***

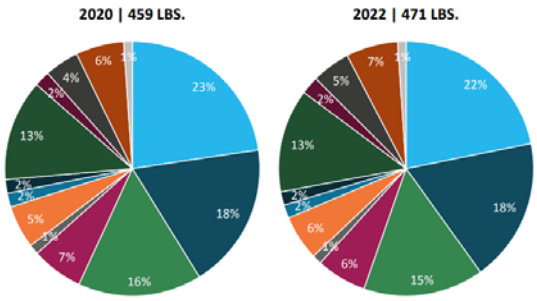

Fig 1.2 Evolution of aluminium content in car per application in North America [7].

Extruded aluminium parts are widely used in the automotive sector. The preferred crystallographic orientation (texture) of the extruded grains is linked to the mechanical properties [8]. A lot of work is focus on the texture of rolled aluminium but the increased need for extruded parts makes the fundamental understanding of these parts' texture necessary.

1.2 Research Aim

The overall aim of this research is to extend the fundamental understanding of microstructure property relations in an extruded high strength Al-Mg-Si-Cu automotive alloy through the extruded procedure developed within Constellium. This is achieved by

understanding: 1) The effect of various extrusion parameters (extrusion speed, extrusion exit temperature, geometry and extrusion ratio) on the development of texture. 2) The relationship of produced microstructure and texture. 3) The effect microstructure and texture have on mechanical properties. 4) The role of texture on the ageing-deformation-ageing (aDA) thermomechanical treatment response.

1.3 Outline of the thesis

The thesis is divided into 9 chapters. Chapter 2 is an introduction to aluminium alloys and their division to cast and wrought classifications. The processing of wrought aluminium alloys, starting with direct chill casting followed by hot extrusion is described. In addition, the strengthening mechanisms of aluminium are presented. Finally, 6xxx aluminium alloys are presented. Chapter 3 describes the materials and the methodologies used in the production and characterization of the investigated profiles. Chapter 4 presents the results and discussion of the effect of extrusion speed on a hollow rectangle profile. Chapter 5 is focused on the studies of different geometry and extrusion ratio profiles. Chapter 6 consists of two parts, in order to decouple the effect of geometry from that of extrusion ratio. The first one is focused on the effect of extrusion ratio for a given geometry while the second is focused on the effect of geometry on a given extrusion ratio. Chapter 7 presents the results and discussion of a complex profile, as a case study, trying to apply the understanding from the previous chapters. Chapter 8 is focused on the effect of further thermomechanical treatment after extrusion on texture. Finally, in Chapter 9, the main conclusions of the whole study are summarized and suggestions for future work are presented.

Chapter 2 Literature review

2.1 Introduction to Aluminium alloys

Aluminium alloys are usually divided in two major categories, cast and wrought. Most aluminium alloys are used as wrought, with these alloys being based on α-Al solid solution phase. Usually wrought alloys are used as foils, sheets or plates. Aluminium casting alloys contain the same alloying elements as typically found in wrought alloys but in greater amounts. With the use of different types of casting, such as sand casting, high-pressure or low-pressure die casting, they are made into components with required shapes. Both wrought and cast alloys are further subdivided into heat treatable and non-heat treatable categories.

2.2 Cast aluminium alloys

Cast aluminium alloys are well known for their relatively low melting temperatures, small solubility for gases, except hydrogen, and good surface finish. There is a wide range of cast Al alloys but the most commonly used are the Al-Si, Al-Si-Cu and Al-Si-Mg. Also, there are many different casting processes such as sand casting, gravity die casting, hot chamber and cold chamber pressure die casting. Despite the many advantages of Al casting, e.g. formation of complex geometries, the high shrinkage during solidification is a major problem. Also, it is usual for cast Al alloys to have inferior mechanical properties than the wrought alloys [9]. Table 2.1 presents the designation of the different series for cast aluminium alloys.

Table 2.1 Designation of cast aluminium and its alloys [3].

Alloying elements	Series designation
Pure aluminium	AA1XX.X
Copper	AA2XX.X
Silicon, with copper and/or magnesium	AA3XX.X
Silicon	AA4XX.X
Magnesium	AA5XX.X
Zinc	AA7XX.X
Lithium	AA8XX.X

2.3 Wrought aluminium alloys

Wrought alloys (extruded, rolled, bended, wired or forged) are strengthened either by work hardening and/or by heat treatment depending on their chemical composition. Fig 2.1 presents a summary of the relationships between the different wrought alloy systems. Also, Table 2.2 presents the designation of the different series for wrought aluminium alloys.

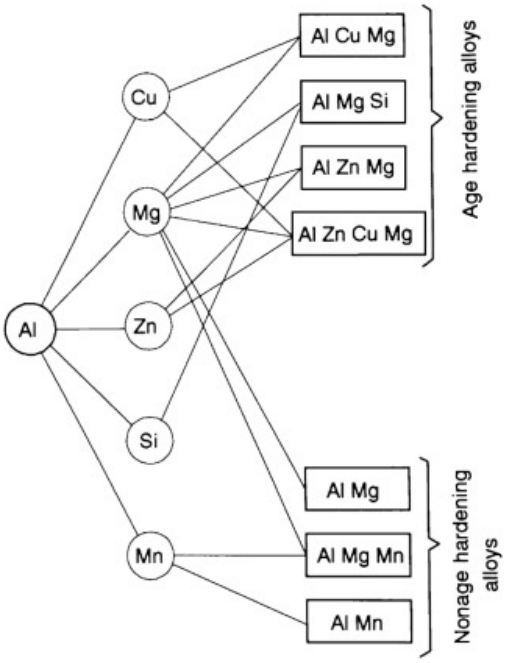

Fig 2.1 Representation of alloying addition relationships summarized in major wrought aluminium alloys [9].

Table 2.2 Designation of wrought aluminium and its alloys [3].

Alloying elements	Series designation
Pure aluminium	AA1XXX
Copper	AA2XXX
Manganese	AA3XXX
Silicon	AA4XXX
Magnesium	AA5XXX
Magnesium and silicon	AA6XXX
Zinc	AA7XXX
Lithium	AA8XXX

Temper designation refers to variations of the physical properties that are achievable within an alloy. There are five basic temper designations for aluminium alloys, which appear as a hyphenated suffix to the alloy number. The temper designation for both wrought and cast alloys is as presented below, Table 2.3.

Table 2.3 Temper designations for cast and wrought aluminium [1].

F	As fabricated (by cold, hot working or casting)
O	Annealed (from cold worked or cast state)
H	Strain hardened by cold working (for wrought products)
T	Heat treated
W	Solution treated (unstable temper)

2.4 Processing of Al wrought alloys

2.4.1 Direct chill casting

Direct chill (DC) casting is one of the oldest methods of large-scale casting, started used in the '30s, producing cylindrical (billets or logs) and rectangular ingots of non-ferrous billets. In aluminium industry, DC casting is the most popular process of casting for billets and ingots further to be extruded or rolled.

Usually, the DC casting procedure is vertical and semi-continuous. The molten alloy is poured into one or more fixed, bottomless, initially closed by a dummy block, water cooled moulds. The ram is lowering as the melt increases in the mould and the solid billet is obtained downwards. A schematic representation of the process is presented in Fig 2.2.

There are two stages of solidification: first the outer layer of metal solidifies within the water-cooled mould. After that, the solid part starts to develop through the bottom of the

mould. Water is directly sprayed on to the produced ingot to remove heat and to continue the solidification of its remaining molten cross section [10].

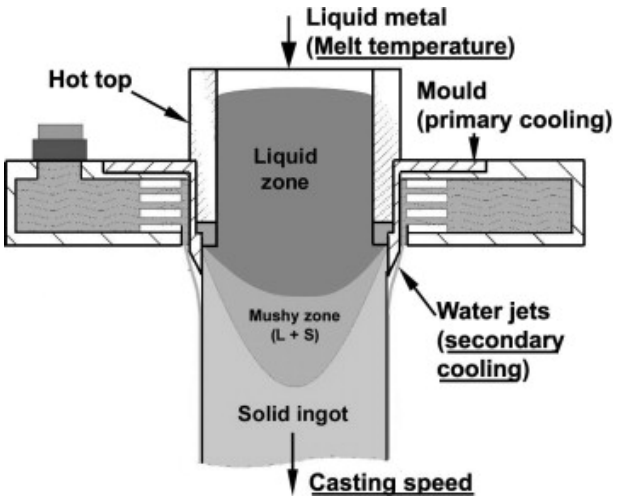

Fig 2.2 Schematic representation of DC cast process [11].

2.4.2 The effect of DC casting on the solidified microstructure

The liquid and solid regions during DC casting will be determined by the process variables and the alloy composition. The different zones during solidification include the liquid pool, the transition region, and the mushy zone. The sum of liquid pool depth and transition region is called the sump and its depth is one the DC casting characteristic features, Fig 2.3.

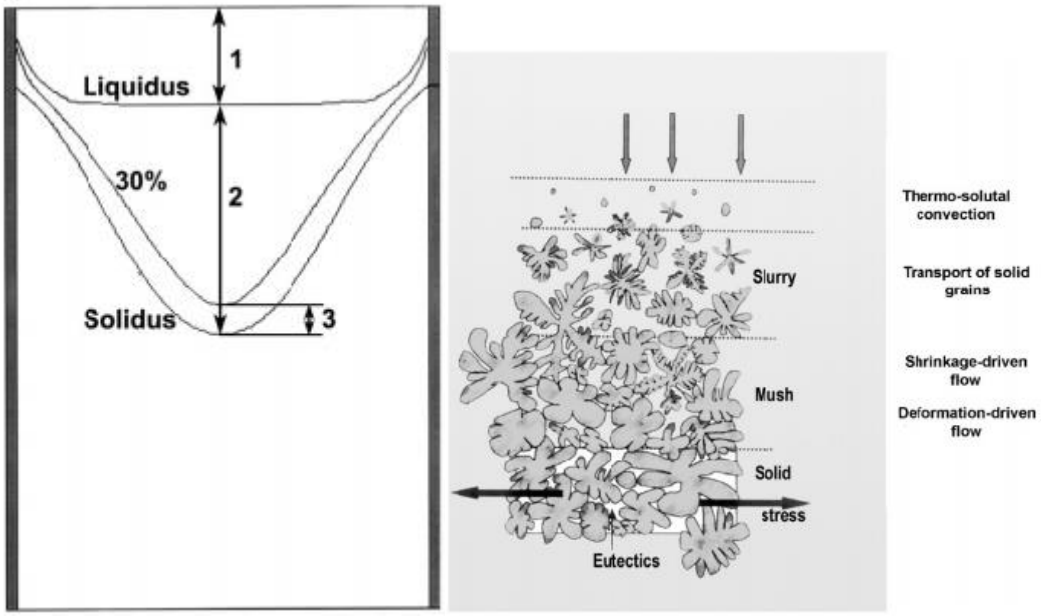

Fig 2.3 Schematic representation of the transition region (a) illustration of the liquidus (L) and solidus (S) isotherms in a typical DC cast round billet. Coherency isotherm is marked as 30 %. The liquid pool depth (1), transition region (2), mushy zone (3), and the sump depth (1+2) are indicated in the diagram, and (b) regions in which different macro-segregation mechanisms are opening [11].

Cooling rate is fundamentally important for DC cast process. It is correlated to heat extraction and affects the final structure of the as-cast material. Other important variables are casting speed and melt temperature.

The solidification microstructure strongly affects the quality of the DC cast billets. There are two main parameters for this: the grain size and secondary dendrite arm spacing (SDAS) and the second phase particles (size, shape, and dispersion).

Grain size depends on alloy composition and cooling rate. The mechanism controlling grain structure is heterogeneous nuclei and growth. Grain refinement has a major effect on grain size and morphology.

Secondary dendrite arm spacing is a parameter of local solidification conditions and depends on the billet's size. Non equilibrium solidification within the dendrites will result to micro-segregation. Final mechanical properties are affected by SDAS, with fine dendritic structure improving final strength.

The main two defect formations during solidification of DC cast billets are macro-segregation and hot tearing. Macro-segregation is attributed to the existence of coarse cell grains in the centre of the DC cast billets. These coarse grains are often called

floating grains, indicating the way they form. Their nucleation starts at an area of the sump, then they flow and grow in the slurry zone and finally locate in the mush. Hot tearing or hot cracking occurs when the semi-solid material fails and loses its integrity due to inadequate compensation of solidification shrinkage and melt flow. Hence, pores can develop into cracks under the presence of thermal stresses. Hot tearing will not occur if there is enough amount of non-equilibrium in the alloy. So, the alloy composition as well as the casting parameters that affect the non-equilibrium amount are very important.

Grain refinement can be described as the deliberate suppression of columnar grain growth and the formation of fine, equiaxed, solidification structure in castings [12]. In general, grain refinement is desirable in DC casting since it can improve the properties and characteristics of the billet. Commonly, Al-Ti and Al-Ti-B master alloys are added to the aluminium alloys in order to refine the grains by chemical inoculation. Grain refinement is directly connected to the nucleation and grain growth. The potent nucleation sites that are inserted into the melt increase the heterogeneous nucleation of primary α-Al grains and enhance the columnar to equiaxed transition (CTE). The refined microstructure reduces the probability of hot tearing and macro-segregation.

2.4.3 Extrusion

The process of aluminium extrusion is one of the most important in metallurgical industry since it can produce a variety of profiles with different shapes and complicated geometries. There are different types of extrusion and they can be classified according to the metal flow direction or according to the process temperature. Direct, indirect, hydrostatic and lateral extrusion are extrusion types regarding the material flow, with most common the direct one. Regarding the process temperature, there is hot and cold extrusion [13]. In direct extrusion a billet that is in the extrusion container is forced through a die. It can be carried out at room temperature (cold extrusion) or higher temperatures (hot extrusion), depending on the material's properties." Hot extrusion occurs at temperatures above the material's recrystallization temperature, preventing work hardening. The advantage of hot extrusion is that the elevated temperature makes it easier to push the material through the die. At the same time the high temperatures and pressures are detrimental to die life. Cold extrusion occurs at room or near to room temperatures. By this way cold working takes place, leading to high strength. Also, compared to hot extrusion, there is lack of oxidation and better surface finish. The disadvantage of cold extrusion is the lack of shape complexity, higher loads, and the extensive lubrication. The most important extrusion parameters

include the extrusion ratio, material's flow stress, strain rate distribution, extrusion speed and thermal conditions [14].

The necessary force, F, for extrusion to happen is given by equation 2.1.

$$F = A_0 k \ln \frac{A_0}{A_f} \tag{2.1}$$

where

A_0, A_f are the cross-sectional areas of billet and extruded profile.

K is the extrusion constant.

High strains and significant friction occur during extrusion process, in particular in direct extrusion, causing various defects, with the most important being surface and internal cracking and pipe. Hence, aluminium flow pattern is an important process factor since it influences the mechanical properties and further the final quality of the extruded product. Different types of metal flow are presented in Fig. 2.4, depending on the level of friction during the extrusion process [1].

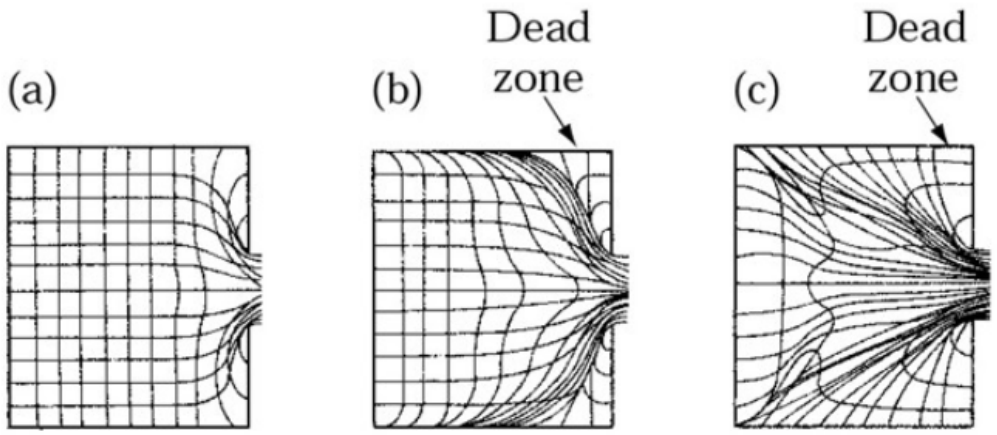

Fig 2.4 Types of metal flow in square die extrusion, a) Low friction flow pattern, or indirect extrusion b) High friction pattern at the billet-chamber interface c) High friction and/or cooling at the outer skin of the billet [1].

2.4.3 Hot extrusion

Hot extrusion is one of the most popular extrusion methods. The extrusion process takes place at elevated temperatures (below solidus temperature of the alloy), resulting in reduced necessary extrusion force and it is preferred for materials with insufficient ductility at room temperature. Simultaneously, it is a way of keeping the material away from work hardening but it also raises some problems. Inhomogeneous deformation can result because of the hot billet cooling in the cooler die. Moreover, heating of the billet results in an oxide layer that can increase the friction and leads to unacceptable surface finishes for many applications. Good lubrication and pre-heating of the die are necessary in order to avoid die wear [1].

2.4.4 Texture

Crystallographic orientation is the positioning of atomic planes of a crystal relatively to a fixed reference. In polycrystal materials grains orientation is rarely random and a tendency of crystallographic preference exists. This preferred orientation of the grains is called texture. Texture is important in materials because a lot of material properties are connected with it. Some of the properties that are texture dependent are strength, ductility, young's modulus and Poisson's ration [8].

Texture may significantly influence the final mechanical properties of a material. The final microstructure, consequently mechanical properties, mainly depends on the deformation and recrystallization processes during the hot extrusion process. The crystallographic textures are split into two categories, deformation and recrystallization textures. Subsequently, the final product's texture depends on the fabrication procedure [15]. The role of the texture in determining the microstructure property relationship is important. But this has not been investigated fully in details.

There is a strong dependence of the deformation textures on the stacking fault energy (SFE) for many FCC metals and alloys. The SFE depends on the material and is affected by the alloying elements. Moreover, it affects the deformation mechanisms, for example deformation twins and dislocation slip. At materials with low SFE, twinning is the predominant deformation mechanism since the critical twinning stress decreases along with SFE. Materials with high SFE are more prone to cross-slip at dislocations. Recrystallization is accomplished by the nucleation of new grains and their subsequent growth into the matrix. Dynamic recrystallization occurs during deformation, while static

after deformation. Also, recrystallization can occur continuously or discontinuously, depending on the evolution of microstructure. For high stacking fault energy materials, like aluminium, recovery occurs immediately and subgrains surrounded by low angle grain boundaries will form from the free dislocations' rearrangement [16].

Deformed metals exhibit recrystallization by nucleation and growth of new, undeformed grains [17]. New high angle grain boundaries will form and start moving into the matrix resulting to changes of the crystallographic orientation, thus, the texture of the material [8]. The literature reported that the main deformation texture components are: Copper {112}<111>, Brass {110} <112> and S {123}<634> and the main recrystallization textures are Cube {100}<001>, Goss {110}<001>, R {124}<211> and P {011} <122>, Table 2.4 [18,19]. In many cases the description of texture with ideal components is not possible but it can be described as a "tube" running through specific texture components. These orientation tubes are commonly called texture fibres. For FCC metals the most usual fibres are α and β. Fibre α runs from Goss to Brass and usually appears at lower deformations and for higher deformations, β fibre is predominant which runs from Copper to S and then to Brass, Fig. 2.5.

Table 2.4 Miller indices and Euler angles of the most important orientations of Al and Al-alloys.

Texture component	**Miller Indices {hkl}<uvw>**	**Euler angles** φ_1 Φ φ_2	
Brass	{110} <112>	35° 45° 0° /90°	Deformation texture components
S	{123} <634>	59° 37° 63°	
Copper	{112} <111>	90° 35° 45°	
Cube	{100} <001>	0° 0° 0°/90°	Recrystallization texture components
Goss	{110} <001>	0° 45° 0° /90°	
CG26.5	{021} <100>	0° 26.5° 0°	
R	{124} <211>	25° 64° 14°	
P	{011} <122>	65° 45° 0°/90°	

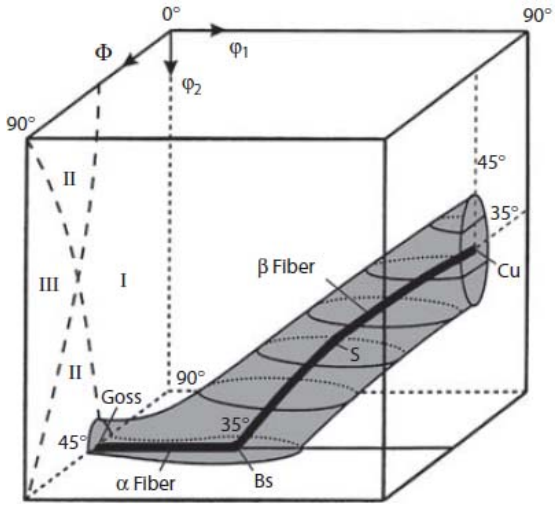

Fig. 2.5 Sketch of the position of α and β fibres in Euler space [20].

Table 2.5 Characteristic fibres in FCC metals and alloys.

Fibre	Fibre Axis	Euler Angles
α	<011>//ND	0°,45°,0°- 90°,45°,0°
γ	<111>//ND	60°,54.7°,45°- 60°,54.7°,45°
τ	<011>//TD	90°,0°,45°- 90°,90°,45°
β		90°,35°,45°- 35°,45°,90°

Materials that are highly textured will develop anisotropy. Extruded aluminium alloys usually develop <111> and <100> fibre textures [21]. Palmer et al. have shown that yield strength will increase while the amount of the <111> fibre increases and that was achieved by decreasing the extrusion aspect ratio [22]. Fortunier and Driver showed that texture has a dominant influence on the strength anisotropy [23, 24].

Also, the ratio of width to thickness strain depends on texture [25]. Finally, texture, through anisotropy, results in strength variations through thickness for thick sections [26,27]. In general, the precise mechanisms involved in order to produce specific

textures are not completely understood, from empirical validation some processes have been established as commercial practices [8].

2.4.5 Electron backscatter diffraction (EBSD) technique

Electron backscatter diffraction (EBSD) is a scanning electron microscope (SEM) based technique, used to obtain crystallographic information, regarding the microstructure, phases and texture of the examined material. The technique is based on the analysis of the Kikuchi patterns, which are obtained after an electron beam hits the surface of a tilted sample and the scattered electrons are collected at a phosphorous screen. The advantage of this technique compared to the traditional approaches is the direct connection between microstructure and orientation. Microtexture is the combination of microstructure and texture and correlates the microstructure with local texture analysis. Moreover, EBSD microtexture information allows us to understand the local distribution of texture than merely a macro texture with texture components as available through X-ray diffraction-based textures. Using EBSD we can get a better understanding of how the texture components are distributed through the microstructure [28,29]. Crystallographic texture affects a series of properties in a material, such as its strength, Young's modulus, Poisson's ratio, ductility and toughness. Manipulation of the texture can lead to tailored materials [8].

2.5 Strengthening mechanisms in aluminium alloys

2.5.1 Introduction

Deformation of perfect defect-free aluminium crystals can result in an increased number of dislocations. As dislocation density increases, the mean free path between dislocations decreases, leading to a higher tendency of interactions between dislocations. The interaction of dislocations can lead to entanglements, cells, subgrain walls or annihilation which finally leads to an increase in strength. Deformation increases the amount of dislocations and develop deformation zones in the matrix with large local misorientation gradients due to dislocation cell formations. In these zones even relatively low strains can produce new high angle boundaries [9].

2.5.2 Solid solution strengthening

The strength of a material can be increased with the addition of solute atoms other than the base metal. The additional atoms occupy substitutional or interstitial positions in the solvent crystal lattice, causing a stress field around them, which can obstruct the dislocation movement. The types of lattice distortion are presented in Fig. 2.5.

There are two factors affecting the solid solution strengthening: the concentration of the additional solute atoms and the size ratio between solvent and solute atoms. There are many types of interaction between the solute atoms and the dislocations, such as, elastic, modulus, long-range order, short-range order, electrical and stacking fault interaction. Elastic interaction happens from mutual interaction of elastic stress fields. A modulus interaction occurs when a solute atom alters the modulus of the crystal. Long-range order interaction occurs in alloys with super-lattices, where the long pattern of atoms gets disturbed from dislocation motion. Short-range order interaction occurs when solute atoms arrange themselves in a way of having more dissimilar neighbours than the equilibrium number. Electrical interaction happens when solute atoms interact with dislocations that have electrical dipoles. Stacking-fault interaction occurs when solute atoms segregate to the stacking faults, resulting to lower stacking fault energy. Elastic, modulus and long-range order interactions are relatively insensitive to temperature and continue to act until about 0.6 T_m [17].

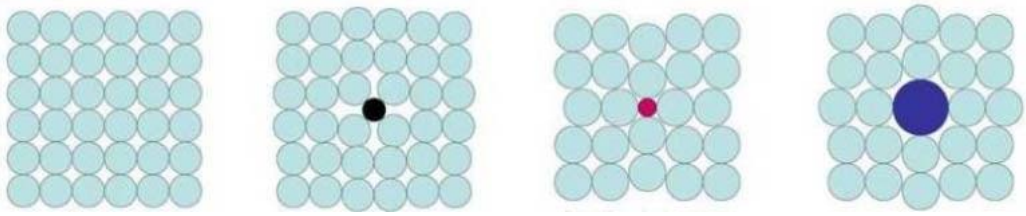

Fig 2.5 Lattice distortion by interstitial and substitutional atoms in a solid solution. a) Perfect crystal, b) large interstitial atom, c) small solute atom and d) large solute atom [30].

2.5.3 Work hardening

The phenomenon where a material's strength is enhanced due to plastic deformation is called work hardening or strain hardening. The energy that is applied to the material moves the existing dislocations and results in producing new ones. The new dislocations generate by Frank-Read mechanism, leading to higher dislocation density. The dislocations will interact and move along the slip planes until either being pinned or tangled. Higher deformation leads to more dislocation's entanglement. During work hardening, the strength and hardness of the material increase, but usually ductility reduces at the same time. The reason for this is that is easier for a crack to develop and grow at the dislocation entanglements, which are also called dislocation forests.

The strength of dislocation can be calculated [31]:

$$\tau = \tau_0 + Gab{\rho_\perp}^{1/2} \quad \textbf{(2.2)}$$

where,

τ_0 is the intrinsic strength of the material with low dislocation density

$\rho_\perp$ is the dislocation density

a is a geometrical factor

b is Burgers vector

G is the shear modulus.

In addition to mechanical properties, physical properties such as electrical and thermal conductivity also change [1].

Work hardening introduces thermodynamic instability since it is a condition of higher internal energy than the undeformed material. Annealing can revert the material to its strain-free state [3].

2.5.4 Grain boundary strengthening

In polycrystalline materials, crystallographic orientation can change sharply from one grain to the next one. The grain boundary strengthening mechanism is based on that, since a dislocation cannot easily move from a specific slip plane to another one of the next grain, especially if those two are very different. Moreover, grain boundaries commonly have atomic disorders, which increase the probability that dislocations will be forced to stop there. More effective are the high-angle grain boundaries since they contain a ledge of immobile dislocations. In addition to that, grain size is very important at this type of strengthening. A small grain size leads to dislocations more easily being trapped at grain boundaries.

The Hall-Petch relation shows the relationship between yield strength (σ_y) and grain size (d).

$$\sigma_y = \sigma_i + k_y d^{-1/2} \quad \textbf{(2.3)}$$

where,

σ_i is the internal stress.

k_y is the strengthening coefficient.

d is the average grain diameter.

It must be noted that the above relation is not valid for very small or very large grains as well as for deformed metals [32,33]. In deformed materials the effective grain size may be described more by the dislocation cell size and not the actual grain size [34].

2.5.5 Precipitation hardening

Second-phase particles can increase the strength of aluminium by obstructing the dislocation motion. That can happen by precipitation hardening.

Precipitation hardening, or otherwise called age hardening, is induced by solution treatment and quenching. A supersaturated solid solution is formed by the solution treatment and quenching before the formation of the precipitates during artificial ageing. The dislocation that moves into the matrix can either cut through the precipitates or bypass them. The force that a precipitate particle can withstand depends on its internal strength and diameter [32]. Fig 2.6 shows the relationship between strength and particle size. The hardening precipitates in Al-Mg-Si systems during heat treatments are enabled due to the addition of Mg and Si. In such systems, the minimum free energy occurs when the shape of the precipitate and its orientation to the matrix give the lowest total interfacial free energy. Interphase boundaries can be divided through their atomic structure into coherent, semi-coherent and incoherent.

A coherent interface occurs when two crystals match perfectly at the interface plane. For this to happen the two crystals have to be oriented relative to each other, so the interfacial plane has the same atomic configuration.

For sufficient large atomic misfits, the coherent interface is being replaced with a semi-coherent where the disorder is occasionally taken up by misfit dislocations. In this case, there are continuous planes combined with regions of discontinuity.

Finally, when the interface plane has very different atomic configuration at the two crystals the interface is incoherent [35].

For coherent particles, the critical diameter, d_c, to promote looping of dislocations without being sheared is:

$$d_c = C\frac{Gb^2}{\gamma_{APB}} \quad \textbf{(2.4)}$$

where,

G is the shear modulus.

b is the modulus of Burgers vector.

γ_{APB} is the energy of the antiphase domain boundaries.

And C is the geometrical factor.

For semi-coherent or incoherent particles this equation is modified by an interface and volume strain energy term [36].

For non-coherent particles:

$$d_c = \frac{4\pi b G_\alpha}{G_\beta} \tag{2.5}$$

where,

G_α is the shear modulus of the precipitate phase.

And G_β is the bulk modulus of the matrix [37].

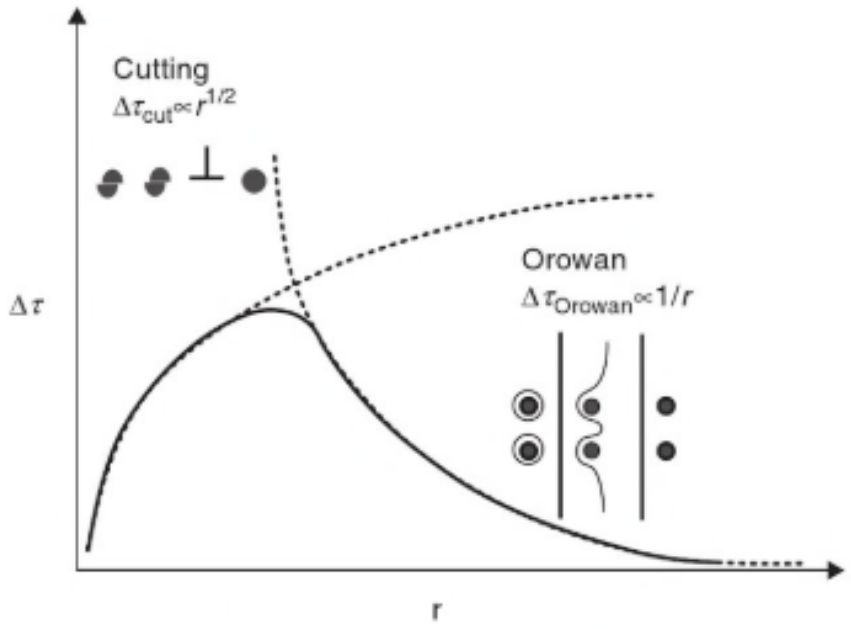

Fig 2.6 A schematic illustration of the strengthening increment observed as a function of precipitate size at a given volume fraction of precipitates, together with the strengthening mechanism operated at a given precipitate size [37].

2.5.6 Precipitation sequence in the binary Al-Cu system

In binary aluminium alloys, maximum solid solubility occurs at eutectic temperatures as shown in Fig. 2.7.

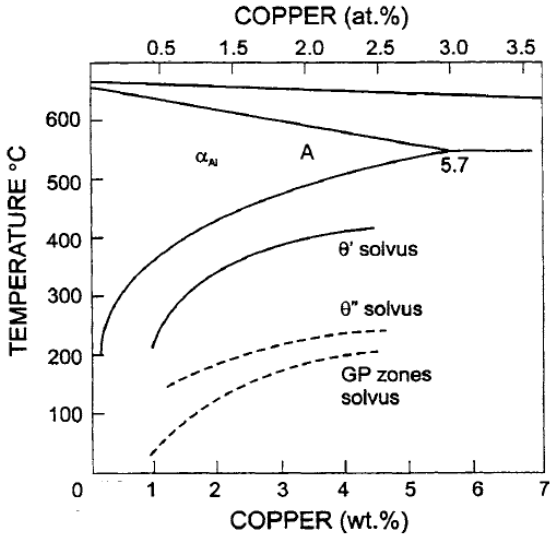

Fig 2.7 Aluminium-rich corner of the Al-Cu eutectic diagram. The positions of the solvus lines for GP zones and the other metastable precipitates are also shown [37].

When a composition of Al-4 wt% Cu (1.7 atomic %) is heated above 570°C for solution treatment, the copper is in a stable FCC α-phase solid solution, and it is retained almost unchanged upon quenching rapidly to room temperature. This results in the formation of a supersaturated state and if the alloy is now aged annealed at 170°C (artificial aging), the first precipitate to nucleate will be Cu-rich GP zones and not the equilibrium θ ($CuAl_2$). This is because of the barrier to nucleation of GP zones, which is less than that of θ phase [38].

Precipitations of the transitional (metastable) phases follow the formation of GP zones. The precipitation process can be written [38]:

SSSS → GP zones → θ''→ θ' → θ

The transitional phases θ´´ and θ´are less stable than the equilibrium θ phase and have higher free energies. The transitional phases form because they have a lower activation energy barrier for nucleation than the equilibrium one. The phases θ´´, θ´ and θ have an approximate composition $CuAl_2$ but different structures: θ´´ and θ´ have a tetragonal unit and plate-like morphology while θ has a complex body-centred tetragonal structure and a rod-like morphology [35]. Fig 2.8 presents the variation of strength on ageing time for an Al-Cu alloy. The GP zones are the initial formed precipitates during artificial ageing, transitional precipitates θ'' and θ' follow and finally equilibrium precipitates θ form.

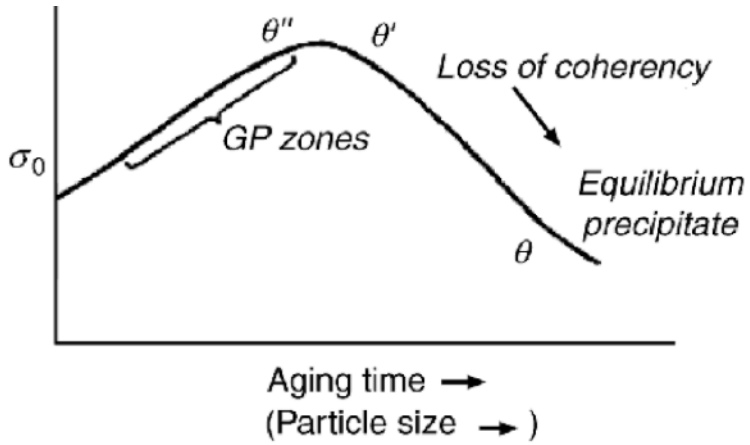

Fig 2.8 A schematic illustration of the strength variation as a function of ageing time (particle size) in an Al-Cu alloy [39].

2.5.7 Precipitation sequence in Al-Mg-Si system

In Al-Mg-Si alloys the precipitation sequence usually follows the pathway below, which can be altered due to temperature, Mg and Si percentages and additional elements [40].

SSSS → Atomic clusters → GP zones → β''→β', U1, U2, B'→β, Si

An overview of the known precipitation phases of the Al-Mg-SI systems, their shape and composition are presented in Table 2.5.

Table 2.5 Overview of known precipitation phases in the Al-Mg-Si system [40].

Phase	Shape	Composition
GP zones	Needle	$Mg_{2+x}Al_{7-x-x}Si_{2+y}$; $1<x+y<3$
β´´	Needle	Mg_5Si_6
β´	Needle	$Mg_{1.8}Si$
U1	Needle	$MgAl_2Si_2$
U2	Needle	MgAlSi
B´	Lath	$Mg_9Al_3Si_7$
β	Plate	Mg_2Si

For the Al-Mg-Si-Cu alloys the precipitation sequence changes to [40]

SSSS→ Atomic clusters→ GP zones →β'', L/S/C, QP, QC → β', Q'→ Q

For Si-rich alloys, GP zones and β'' have similar unit cells and structures. An overview of the known precipitation phases of the Al-Mg-Si-Cu systems, their shape and composition are presented in Table 2.6.

Table 2.6 Overview of known precipitation phases in the Al-Mg-Si-Cu system [40].

Phase	Shape	Composition
QP	Needle	Unknown
QC	Needle	Unknown
C	Plate	Unknown
L	Needle	Unknown
Q´	Needle	Probably $Al_3Cu_2Mg_9Si_7$
Q	Needle	Probably $Al_3Cu_2Mg_9Si_7$

2.6 6xxx Aluminium alloys

2.6.1 Introduction

6xxx aluminium alloys (Al-Mg-Si) can be traced back to the very early 20th century. They have many attractive characteristics, such as medium to high strength, especially after heat treatment, good formability, corrosion resistance and surface finish [41]. Their suitability for a range of applications has made them the most extrudable products in the market. Al-Mg-Si alloys are heat-treatable Al alloys as a result of the formation of magnesium silicide (Mg_2Si), the primary hardening phase. An increase of Mg_2Si in the alloys results in higher tensile properties but is detrimental to extrudability. Moreover, controlling the ratio between Mg and Si, a range of strength levels may be achieved in the 6xxx series alloys which will be exploited to provide a strength level required for a range of applications which is inherent to the system, Fig. 2.9 [42,43].

Dispersoids form during the homogenisation of billet at temperatures from 450°C to 600°C. They are intermetallic compounds that commonly contain Zr, Cr, Mn, Fe and Sc. Their sizes are comparable and even finer than precipitates. Dispersoids can control the grain structure during thermomechanical processing, such as extrusion. A fine

distribution of dispersoids can control the microstructure by delaying static recrystallization [13,44].

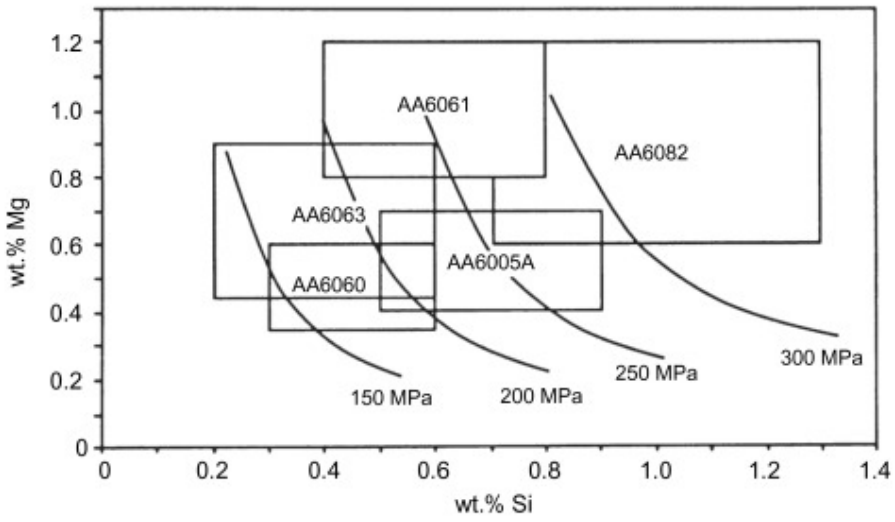

Fig 2.9 Compositional limits of common 6xxx alloys and their typical yield stress levels in the peak aged condition (T6) [43]

2.6.2 Al-Mg-Si-Cu system

The addition of copper in 6xxx series enhances the strength and ductility due to the influence that Cu has on the precipitation behaviour of the material during the heat treatment. Cu increases the precipitation kinetics of β'' during artificial aging and modifies the precipitates in the material [45,46]. The three-phase field of Al-Mg-Si systems converts into a tetrahedron space with the addition of Cu. The four-phase field of Al-Mg-Si-Cu alloys consists of the primary aluminium (Al) and the quaternary intermediate Q phase and two of the other three phases (θ, β and Si), depending on the alloy composition as shown in Fig. 2.10 [47].

The principal precipitation hardening reactions arise from the ternary Al-Cu-Mg system. The primary intermetallic phases of these systems are the $CuAl_2$ (θ phase), $CuMgAl_2$, Mg_2Si and Q phase ($Al_4CuMg_5Si_4$ or $Al_5Cu_2Mg_8Si_6$) [47,48].

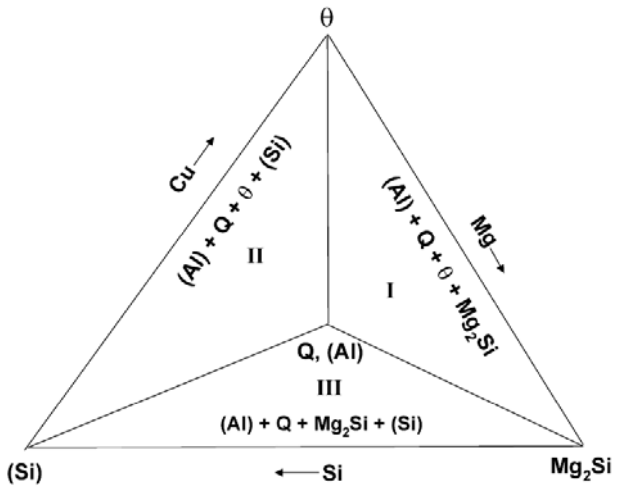

Fig 2.10 Al–Mg–Si–Cu alloys grouped by phase field occupancy on a pseudo-projection of the four-phase-field tetrahedrons. The vertical line represents alloys with Mg/Si=1 [47].

2.6.3 Effect of ageing and deformation on 6xxx

Fallah et al. [49] investigated the early-stage precipitation in Al-0.8Mg-0.8Si and Al-0.94Mg-0.47Si. Through high resolution electron microscopy, they discovered that the initial spherical FCC-structured clusters (C1) developed into elongated clusters, firstly on $\{111\}_{Al}$ (C2) and then on $\{100\}_{Al}$ planes and along $<100>_{Al}$ directions (C3). Three different types of precipitates were documented from Esmaeili et al. [50] for AA6111 during aging at 180°C, namely, GP zones, β'' and Q'. They reported that β'' phase was the one responsible for high hardening rate. Ding et al. [51] found that L, Q' and β'' were the main precipitate phases in an Al-Mg-Si-Cu system after peak-ageing at 180ºC for 30 minutes. Also, it was noticed that the level of Cu changes the alloy dependence on the Mg/Si ratio. Three types of precipitates were also reported for A6061, from Buha et al. [52]: GP zones, β'' and fine structured Mg-Si(-Cu) co-clusters were detected in the peak-aged microstructure. The effect of Cu addition in Al-Mg-Si alloys was investigated by Marioara et al. [40] as well. The overall hardness of the Cu-containing alloys was higher than the Cu-free ones. Moreover, the Cu addition made the alloys less sensitive to the Mg/Si ratio, in relation to hardness evolution. Finally, it was found that the β'' and pre-β'' phases only contribute to a maximum of 30% to the precipitates in the peak-aged material, which leaves the Cu accountable for the rest of them. Wang et al. [53] developed a thermomechanical process for 6061 Al sheets, consisting of pre-ageing, cold rolling and peak-ageing. Specifically, the pathway was pre-ageing at 180°C for 2h,

75% reduction with cold rolling and peak-ageing at 100°C for 48h. This procedure showed to greatly improve the mechanical properties. The mechanism responsible for this strength enhancement was found to be a combination of precipitation hardening, dislocation hardening, sub-structure hardening and high Taylor factor value.

The composition and density of the β'' phase change accordingly to Si content in 6xxx alloys [54]. Gupta et al. [55] showed that excess of Si improves the ageing response and strength by enhancing β'' precipitations, but not for over-aged alloys, which will have a decline in strength due to unstable precipitations with reduced Mg/Si ratio. Murayama and Hono [54] suggested that the GP zones formed during pre-ageing are responsible for the β'' precipitations in peak-aged material as the former act as nucleation sites for the latter.

Perovic et al. [56] showed the different precipitating phases that occur in two Al alloys, i.e. AA6016 and AA6111, after following the same heat treatment path. Both alloys were pre-aged at 180°C for 0.5 hour and then peak-aged at 180°C for 11 hours. In the microstructure of AA6016 only β'' was identified while in AA6111 β'' and Q phase were present.

A mechanism of vacancy diffusion on demand, with the addition of a microscopic amount of Sn, was proposed by Pogatscher et al. [57]. By this way, the problem of natural ageing of long-time storage Al-Mg-Si alloys can be controlled. Also, Jia et al. [58] showed that the combination of pre-straining and pre-ageing enhances the precipitation of β'' phase by originating C2 and dislocations while inhibiting natural ageing. The great effect that deformation has on the precipitation evolution of AA6060 was also shown by Teichmann et al. [59]. Their HRTEM study showed that pre-deformation causes a heterogeneous precipitation, only on dislocations. In another study [51] it was found that 2% of pre-deformation is the optimized percentage for drastic increase of material's hardness and simultaneously supressing natural ageing. The addition of Cu can further enhance these results. In addition, Bryant [60] showed the importance of pre-ageing treatment immediately after quenching. A finer distribution of precipitates, resulted by changes of metastable phases, enhanced the mechanical properties. Birol [61] investigated the importance of pre-ageing after a period of natural ageing. Short time heat treatments between 200°C and 250°C before a standard paint-bake treatment improved the hardness of AA6016. The heat treatments showed to enhance the formation of stable GP zones.

Trivedi et al. [62] investigated the microstructural evolution during deformation in a series of Al alloys. For all the alloys, deformation increased the density of substructural dislocations and fraction of low angle boundaries. AA6022 had the greatest increase of grain orientation spread and it was contributed to the coarse Mg_2Si particles that were observed. Also, an interesting observation was that for grains/subgrains with cube orientation the distribution of sub-structural dislocations was inhomogeneous.

Mirzakhani and Payandeh [63] investigated the influence of severe plastic deformation, such as equal channel angular pressing (ECAP), of AA6063 on natural and artificial ageing. Their conclusion was that the combination of the above, i.e. a thermomechanical process, can improve the overall material's mechanical properties. The effect of artificial ageing was also studied by Österreicher et al. [64]. It was found that mechanical properties can vary even with small differences of artificial ageing.

Moreover, Engler et al. [65] investigated the effect of deformation (stretching) and natural ageing on the properties of AA6016 and showed that their combination has a great effect on the material's mechanical properties.

Pedersen et al. [66] investigated the texture and grain structure of extruded AA6063 and 6082, as well as their formability. The two alloys were investigated in the as-extruded condition as well as after a thermomechanical process. A combination of cold rolling and annealing was used to deform and heat treat the alloys. The final four materials (as-extruded AA6063 and 6082 and deformed-heat treated AA6063 and 6082) had different texture. For the as-extruded materials, the AA6082 had a β-fiber texture while AA6063 had predominantly cube texture. After the thermomechanical process the texture was almost random for both alloys. Regarding formability, it was found that cube texture had the higher formability while the lowest formability values were associated with the β-fiber texture of the as-extruded AA6082. Between the two deformed and heat-treated alloys there was no significant difference in formability, even though AA6082 had higher strength. Another study showed that ductility decreases in the presence of coarse precipitates, as they enhance crack nucleation [67].

Chapter 3 Experimental techniques

3.1 Alloy composition

The chemical composition of the billets used in all the investigations is presented in Table 3.1.

Table 3.1 Chemical composition (wt.%) of the investigated and the most similar AA6xxx alloys used in automotive industry.

Alloy	Si	Fe	Cu	Mn	Mg	Cr	Zn	Ti
Investigated	Max. 0.8	Max. 0.3	Max. 0.8	Max. 0.6	Max. 0.7	Max. 0.1	Max. 0.1	Max. 0.1
6061	0.4-0.8	<0.7	0.15-0.4	<0.15	0.8-1.2	0.04-0.35	<0.25	<0.15
6082	0.7-1.3	<0.5	<0.1	0.4-1	0.6-1.2	<0.25	<0.2	<0.1

3.2 Direct Chill (DC) Casting

DC cast billets of a high strength Al-Mg-Si-Cu alloy, produced at Advanced Metal Casting Centre (AMCC), Brunel University London, were used. The composition was provided by Constellium. After casting, the 152 mm diameter and 2 m long logs were homogenized. The logs were further cut into smaller billets of 420 mm, which were used for the extrusions.

3.3 Extrusion

All the extrusions were performed at the AMCC, Brunel University London. The DC cast billets were direct extruded in a horizontal extrusion press of 35 MN maximum press capacity. The container was held at 420°C during the whole procedure. As a final step after extrusion, the material was immediately quenched with an agitated water wave combined with sprays. The extruded material was either investigated as extruded or was further heat treated and deformed. In the next chapters it is clearly stated the condition of the material presented.

3.3.1 Extruded profiles

The profiles used in this thesis as well as some of the extrusion parameters are presented in Fig 3.1-3.3 and Tables 3.2-3.3.

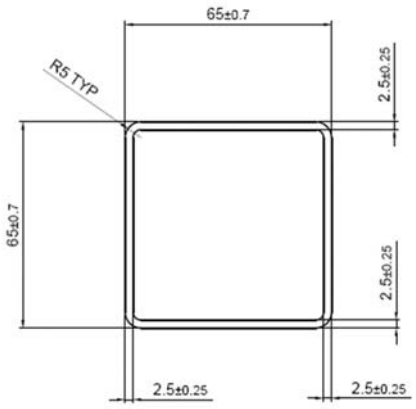

Fig 3.1 Hollow rectangle profile (dimensions in mm).

Table 3.2 Extrusion parameters for the two extrusion recipes of hollow rectangle.

Billet	Container T (ºC)	Exit T (ºC)	Extrusion Speed (m/min)
A	420	540	6
B	420	550	9

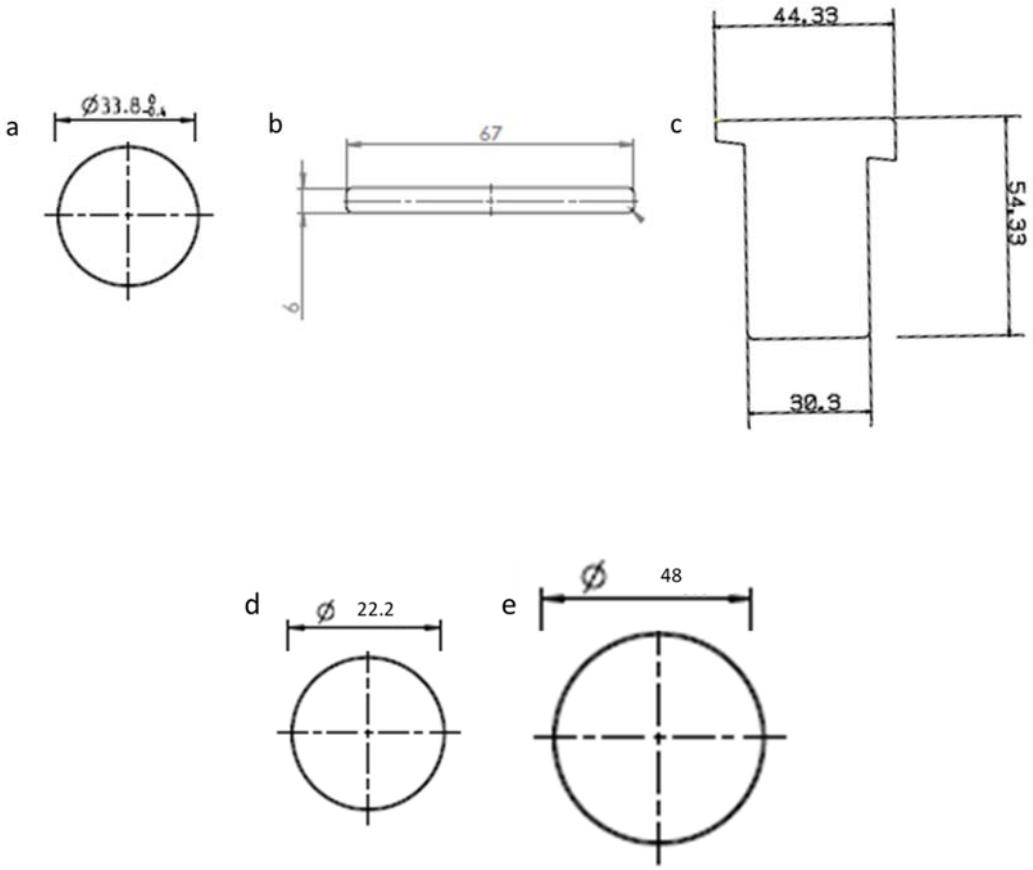

Fig 3.2 a) Medium round bar, b) flat bar, c) tow nut, d) small and d) large round bar profiles (dimensions in mm).

Table 3.3 Extrusion parameters and ER for the three round bars, flat bar and tow nut.

Profile	Extrusion Ratio (ER)	Extrusion exit speed (m/min)	Exit T (ºC)
Small round bar	55	9.3	548
Flat bar	50	9.6	540
Medium round bar	20	8.5	560
Big round bar	10	5.8	553
Tow nut	10	7	552

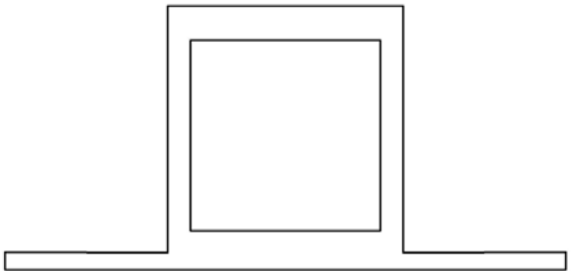

Fig 3.3 Complex profile for side impact beam application (dimensions are not disclosed in this thesis due to commercial confidentiality).

3.4 Thermomechanical Treatment

The subsequent thermomechanical treatment of the extruded samples involved a combination of heat treatments and induced deformation and is referred as aDA (pre-ageing, deformation, post-ageing). Specifically, the material was subjected to an initial heat treatment (pre-ageing), then it was stretched along the extrusion direction, and finally it was subjected to another heat treatment (post-ageing). The specific processing conditions of aDA thermomechanical treatment are commercially sensitive and therefore cannot be disclosed in this thesis.

For the heat treatments a Carbolite electric resistance furnace with fan convection for rapid heating and cooling was used. The accuracy of the furnace temperature was measured with a K-type thermocouple (± 2 ºC). After the heat treatments, the material was immediately quenched in room temperature water. For the stretching an Instron 5500 Universal Electromechanical Testing System, equipped with Bluehill software and a 50 kN load cell was used.

3.5 Material characterization

3.5.1 Optical microscopy (OM)

The extruded material was investigated with the use of a Zeiss Axioscope optical microscope (OM). Samples were taken from the extrusion-normal plane. The material was sectioned and cold mounted in polyester resin. The standard metallurgical grinding steps were followed and then polished to a 0.04 μm finish with the use of OPUS non-crystallising colloidal silica suspension (Metprep Ltd.). Because of the nature of the material and since the goal of the investigation was the depiction of the grains and PCG layer the polarized mode was preferred in some cases and the material was anodized. For the etching, Baker's reagent (5 mL HBF_4, 200 mL H_2O) was used, and the material was immerged in it for 1 min at 15V.

3.5.2 Electron Backscatter Diffraction (EBSD)

The microstructure and texture of the extruded material was studied with EBSD. Samples were taken from the extrusion-normal plane, Fig 3.4. The preparation for EBSD analysis included the standard metallurgical grinding steps, and then polished to a 0.04 μm finish using an OPUS non-crystallising colloidal silica suspension (Metprep Ltd.), following by electropolishing as a final step. For the electropolishing, a mixture of 30-70% nitric acid-methanol was used and the samples were immersed into it for 1 minute at 12V.

EBSD analysis was performed on a Crossbeam 350 FIB-SEM (Carl Zeiss AG) equipped with a Hikari Plus EBSD camera (EDAX Inc.). The samples were 70º tilted from horizontal and a 20 kV accelerating voltage was used. In most cases the scan step size

was set to 0.5 μm. The scanned EBSD data were analysed with TSL-OIM Analysis software (EDAX Inc.). An average of three maps per presented condition was performed, at different locations. For the calculation of the orientation distribution function (ODF) the harmonic series expansion method was used, with L_{max}=22 and a Gaussian half-width of 5°. A triclinic sample symmetry was assumed.

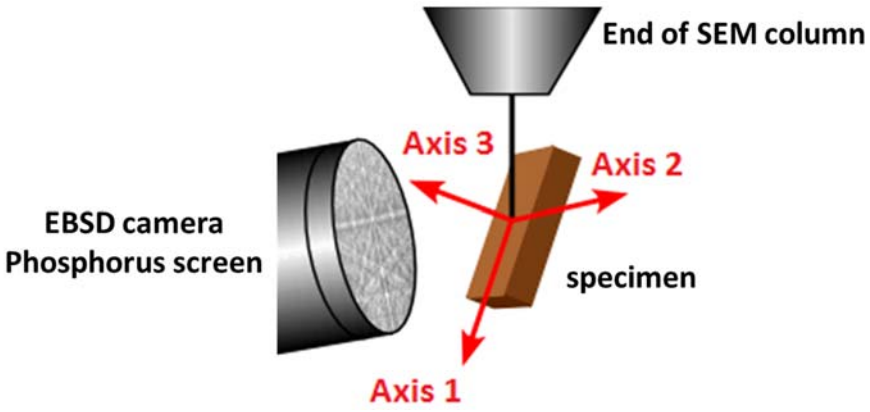

Fig 3.4 Schematic of the SEM-EBSD set up and the direction of the sample (Axis 1=ND, 2=ED and 3=TD).

3.5.3 X-Ray diffraction pattern (XRD)

In some cases, samples investigated by EBSD were further studied with X-ray diffraction for texture analysis. These studies were carried out at Constellium Technology Center, at Voreppe France.

For the thin profiles (e.g., hollow rectangle and flat bar) a sandwich structure was preferred during the sample preparation while for the bulk profiles (e.g., bars and bumper tow nut) a slice was sufficient, as shown in Fig. 3.5. The measurements were conducted in the normal-transverse plane. A Panalytical X'Pert Pro goniometer with Copper ceramic X-ray tube and flat graphite monochromator was used. The goniometer is equipped with a collimator with parallel slit at 0.27º and polycapillary lens, φ 14 mm, calibrated with crossed slits. A voltage of 45 KV and a current of 40 mA was used.

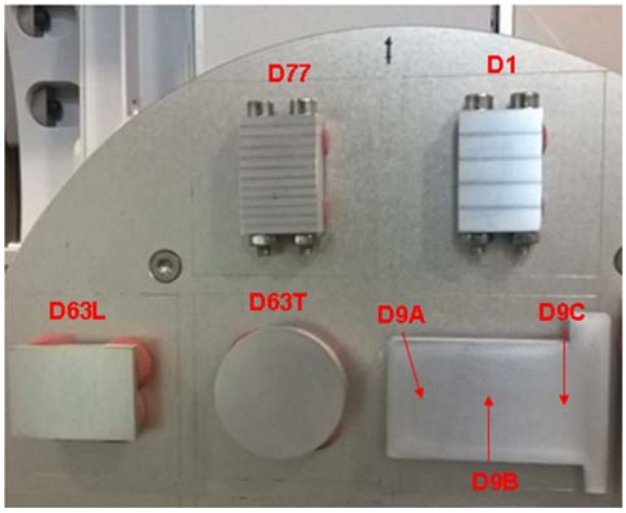

Fig. 3.5 A photograph showing the specimen for texture analysis using XRD.

3.6 Tensile test

Tensile tests were performed following ASTM E8 standard, using an Instron 5500 Universal Electromechanical Testing System, equipped with Bluehill software and a 50 kN load cell. All the tests were performed at room temperature at a dual strain rate of 0.015 min^{-1} up to 1% strain and 0.4 mm^{-1} up to failure. Standard dog-bone and subsized round samples were used depending on the geometry of each profile, as shown in Fig. 3.6. For the thin profiles, standard dog-bone samples were machined and their thickness was the same with that of each profile. For the bulk profiles, subsized round samples were machined with critical diameter of 6 ± 0.02 mm. All the samples were machined parallel to the extrusion direction. For each condition presented, six tensile samples were tested. The exact positions where the tensile samples were taken for hollow rectangle, flat bar, bumper tow nut and the three round bars are presented in Figs 3.7 and 3.8.

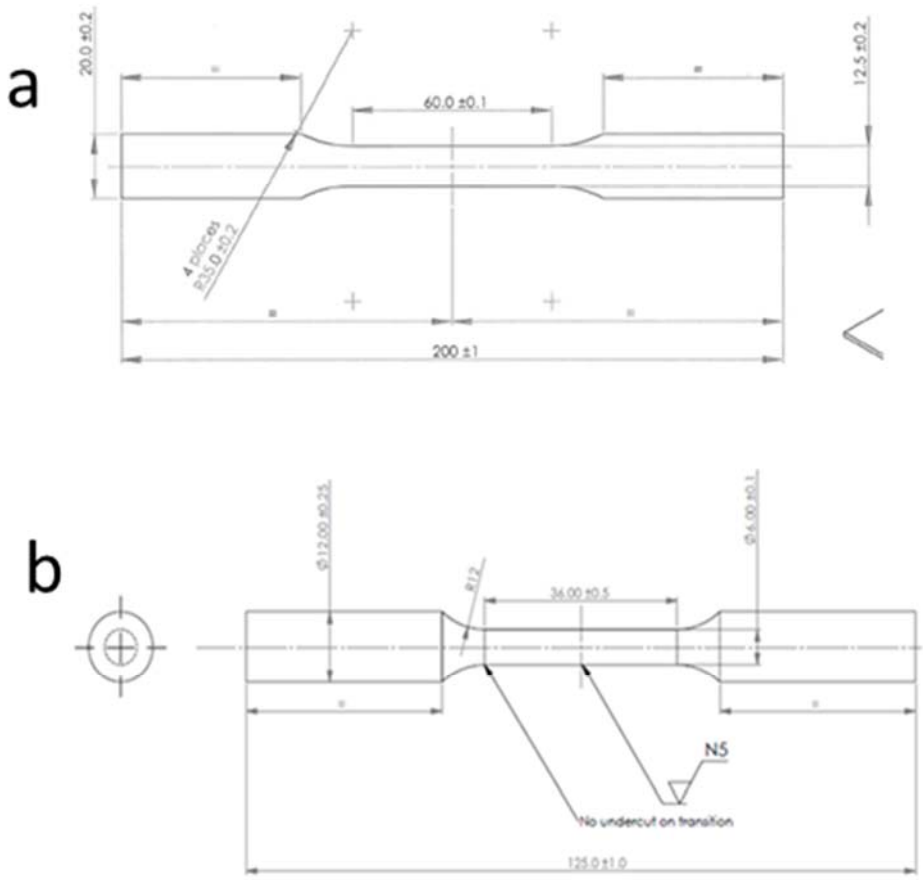

Fig.3.6 A schematic diagram of a) dog-bone and b) subsized round tensile test specimens.

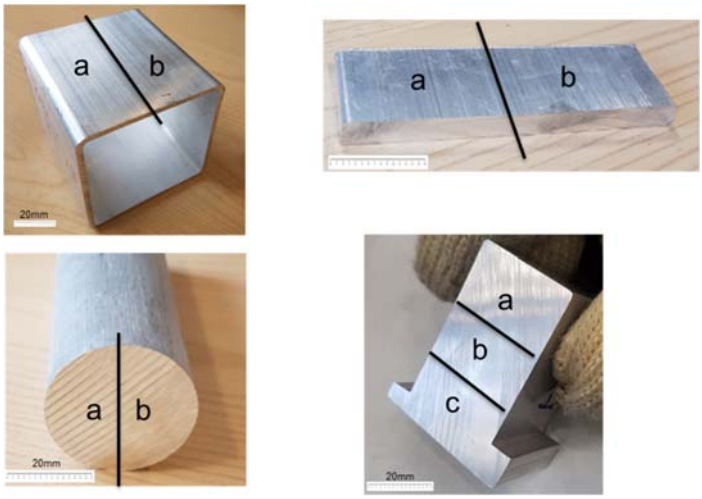

Fig. 3.7 Photographs showing various extrusion profiles with indication of the location where specimens were made for tensile testing.

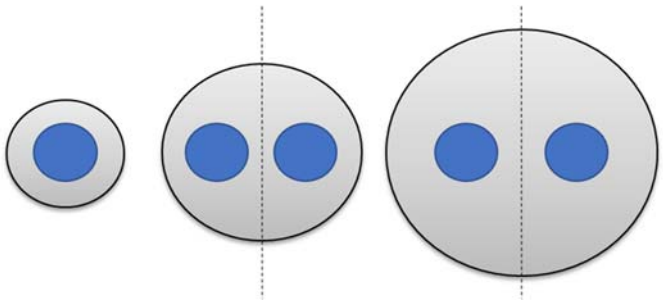

Fig 3.8 Schematic of the tensile samples position for each profile of round bar.

Chapter 4 Effect of the extrusion speed on resultant microstructure and properties

4.1 Introduction

Extrusion is a complex procedure that involves different parameters. This includes billet homogenization, preheating time and temperature, quenching and others. It is well known that final properties reflect the parameters of the extrusion process. Extrusion speed, extrusion ratio and extrusion temperature are the factors that can be controlled during the process. In practice, the extrusion ratio usually is determined by the industrial need, so the only values that can be controlled are speed and temperature.

Extrusion speed and temperature are linked through pressure. Speed affects the metal flow, the final surface quality and the mechanical properties. In reality, the extrusion speed is determined based on the extruded alloy and the practical experience from the extrusion press [68]. For better productivity, a good control of the extrusion parameters is necessary [13]. Moreover, optimized extrusion parameters can lead to increased productivity and better final products. Therefore, the understanding of their effect on microstructure, texture and mechanical properties of the final extruded product is essential.

This chapter is concerned with the study of the effect of extrusion speed of a fixed hollow profile on the resultant microstructure, texture and mechanical properties using a combination of EBSD and tensile testing methods.

Two different extrusion speeds were used for this extrusion speed investigation; billet A was extruded with 6 m/min and B with 9 m/min. The extrusion parameters are presented in Table 4.1. Even though the aim was to keep all the rest of the parameters constant, the change of the extrusion speed results in a change of the exit temperature. A hollow rectangle profile with external dimensions 65 x 65 mm and 2.5 mm thickness was used for this extrusion trial.

4.2 Microstructure

For this investigation the EBSD scans were performed on the normal-extrusion plane (ND-ED). Fig 4.1 shows the inverse pole figures (IPF) of the material extruded at low speed (A) and high speed (B). In both cases, grains are elongated along the extrusion direction with a small amount of recrystallized grains. Moreover, subgrains inside the thicker grains can be detect in both cases. Morphologically, the profiles appear to be very similar, but an intense difference of the colour can be observed. This colour variation indicates a difference of the crystallographic texture found in samples processed under different extrusion speed. The grain size increased with increasing extrusion speed. The average grain size was found to be 4.2 μm for sample A and 6.1 μm for B. Furthermore, both high and low angle grain boundaries were similar for both samples, Table 4.1.

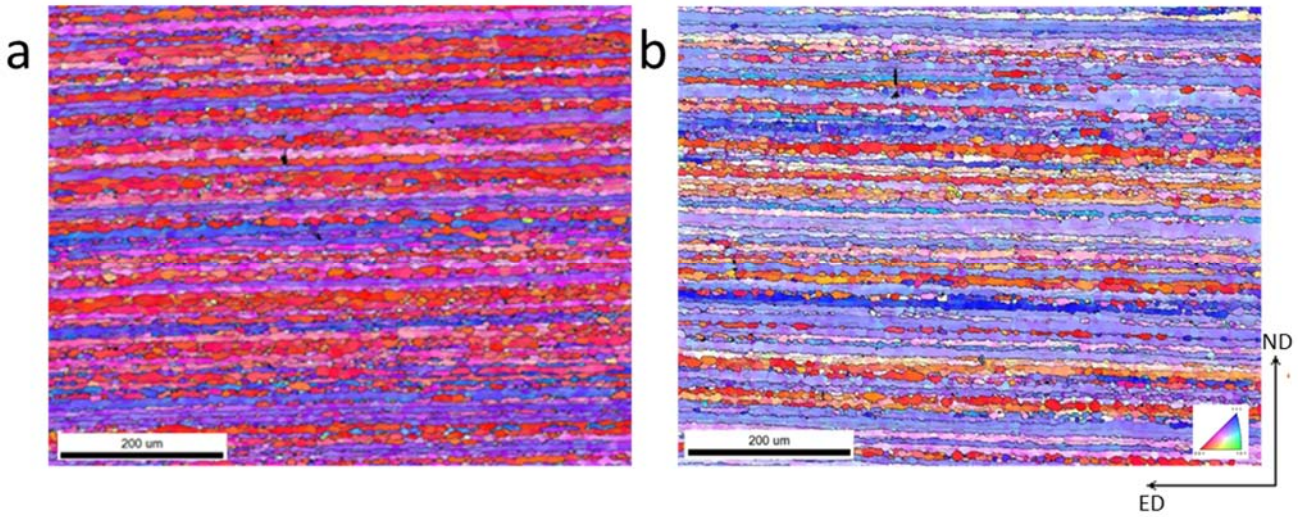

Fig 4.1 IPF maps of samples extruded at a) low and b) high speed.

Table 4.1 Average grain size (and standard deviation), high (15º-65º) and low (5º-15º) angle grain boundaries of the two samples.

Sample	Extrusion speed (m/min)	Av. Grain size (μm)	HAGB (Fraction)	LAGB (Fraction)
A	6	4.23 (0.010)	0.57	0.24
B	9	6.13 (0.012)	0.51	0.25

4.3 Effect of extrusion speed on the texture of extruded samples

Fig 4.2 shows the Orientation Distribution Function (ODF) of the two samples. As it can be observed in both samples, the texture is mainly Brass-S and Cube and looks similar to rolling texture. The intensity (19.05) of sample extruded at 9 m/min is stronger than the intensity (13.78) of sample extruded at 6m/min.

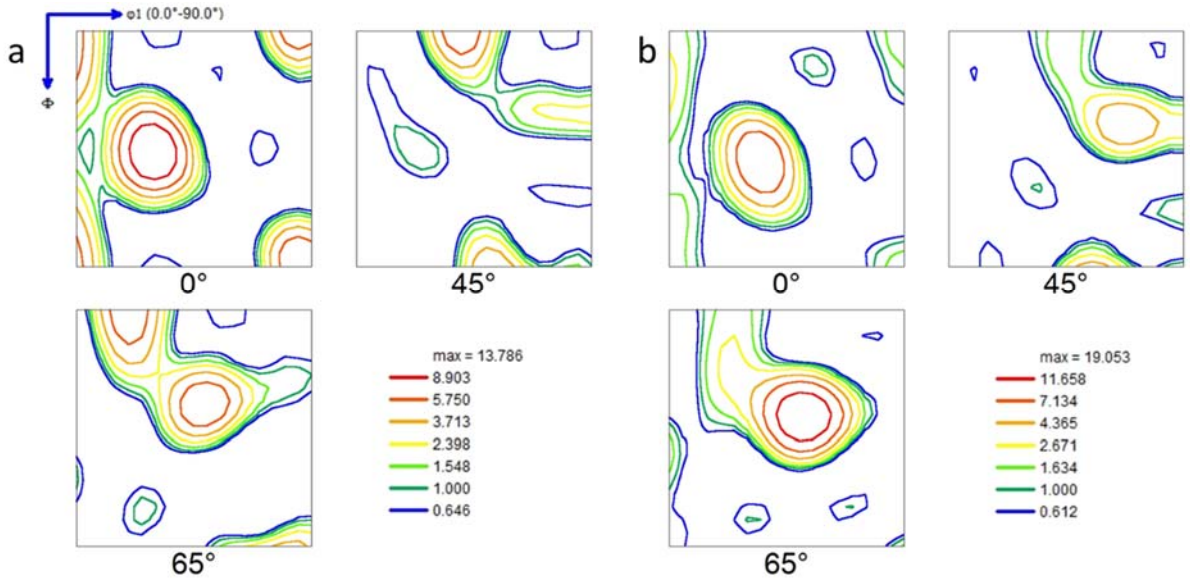

Fig 4.2 ODF sections (φ2 = 0°, 45° and 65°) of samples extruded at: a) low and b) high extrusion speed.

In order to have a better understanding, the volume fractions of the main texture components appearing in the samples were calculated by integrating the ODF within 15º of the ideal component, as shown in Table 4.2. The volume of Brass was found to be comparable for these two extruded samples. However, sample extruded at 9m/min, exhibits increased amount of S component (43.1%) as compared to sample A, extruded at 6m/min. Moreover, the increased extrusion speed decreased the total Cube fibre (Cube-Goss-CG26.5) volume from 24.9% to 12%. Finally, a similar small amount of Copper component is observed for both samples.

Table 4.2 Volume fraction of the main texture components of A) low and B) high extrusion speed sample.

Sample	Brass {110}<112>	Copper {112}<111>	S {123}<634>	Cube {001}<100>	Goss {011}<100>	CG26.5 {021}<100>	Total Cube fibre (Cube-Goss-CG26.5)
A	22.3	6	30.1	13.1	1	10.8	24.9
B	24.5	5.3	43.1	3.6	2.5	5.9	12

4.4 Effect of extrusion speed on the mechanical properties of extruded samples

Table 4.3 shows the properties of the two extruded samples. Comparing the strength difference between extrusion speeds we can notice that the extrusion speed increase had an effect on yield strength (~ 12 MPa). In detail, sample A, extruded with the low speed (6 m/min) reached 334.8 ± 1.62 MPa, while sample B, extruded with the high extrusion speed (9 m/min), reached 346.7 ± 5.9 MPa. Furthermore, the change of the exit temperature while changing the extrusion speed should also be taken under consideration. Finally, the n-value (strain hardening exponent) did not change significantly between the two extrusion speeds, 0.085 and 0.088 for low and high speed respectively.

Table 4.3 Tensile properties of the two samples extruded at different speeds in T6 condition.

Sample	Extrusion speed (m/min)	YS (MPa)	UTS (MPa)	EL (%)	n-value
A	6	334.83 ± 1.62	374.03 ± 3.13	9.23 ± 0.81	0.085
B	9	346.76 ± 5.91	387.93 ± 6.38	9.83 ± 1.06	0.088

4.5 Investigation of different sides

Significant variations of strength differences between the different sides of the profile were noticed, which even though axisymmetric was showing these irregularities. In theory, the material flow through the extrusion should be symmetrical, based on the profile's symmetry. Moreover, if all the processes through the extrusion were accurate, we would not expect to see these strength differences from side to side.

An investigation of the sides of the high extrusion speed was proposed, trying to explain these strength differences based on the crystallographic texture. From the four sides of the profile, the top and the side were chosen for this investigation. Table 4.4 gives a list of tensile properties of top and right-hand side of extrusion fabricated at high speed.

These two sides were the ones showing repeatedly lower and higher yield strength, 335.8 ± 4.27 MPa 348.6 ± 5.25 MPa respectively.

Table 4.4 Tensile properties of the top and side samples extruded at 9 m/min, in T6 condition.

Sample	Extrusion speed (m/min)	YS (MPa)	UTS (MPa)	EL (%)	n-value
Top	9	335.8 ± 4.27	384.03 ± 1.34	10.2 ± 0.98	0.09
Side	9	348.6 ± 5.25	389.5 ± 2.47	9.31 ± 1.12	0.087

4.5.1 Microstructure

The microstructure of both sides is similar, with thin grains elongated through the extrusion direction and some recrystallization, Fig 4.3. Closer investigation shows that the average grain size at the top is 6.1 μm while for the side 3.8 μm; there are no significant differences at the amounts of high and low grain boundaries, Table 4.5.

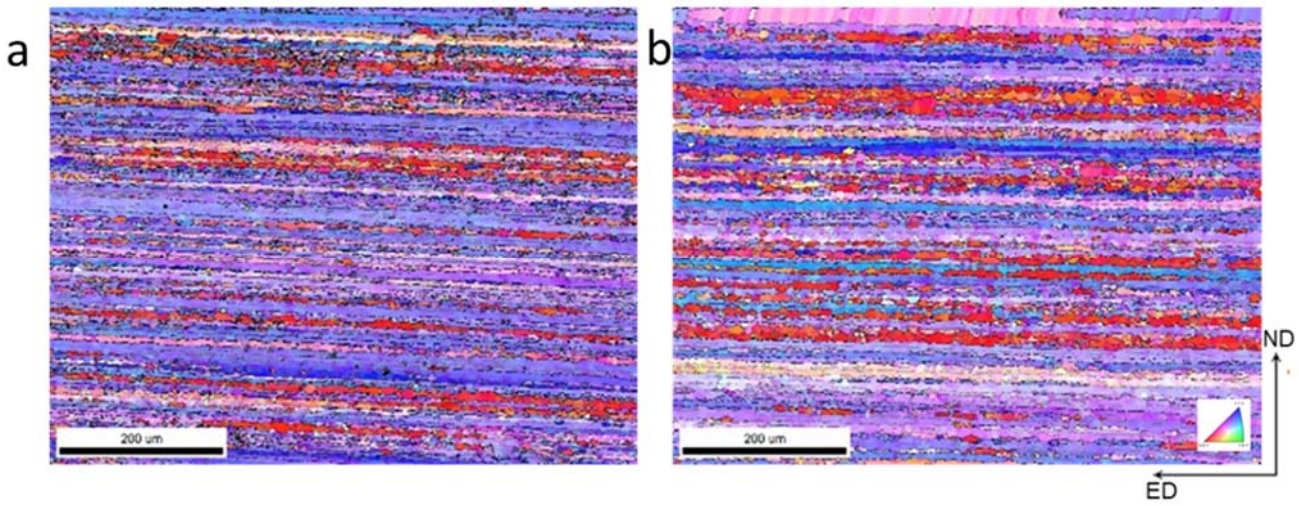

Fig 4.3 IPF maps a) of the right-hand side and b) the top of the hollow rectangle profile extruded in the high speed.

Table 4.5 Average grain size (and standard deviation), high (15º-65º) and low (5º-15º) angle grain boundaries of the side and the top of the extruded profile.

Sample	Av.Grain Size (μm)	HAGB (fraction)	LAGB (fraction)
Side	3.81 (0.017)	0.47	0.21
Top	6.12 (0.012)	0.42	0.21

4.5.2 Texture

The ODFs at 0º, 45º and 65º of the side and the top of the profile are presented in Fig 4.4. The areas of the scans were close to the center of the cross section, in the same plane as all the other investigations. From the ODFs we can notice that the texture is the same in both sides, with higher intensity for the side sample, at 22.18. Brass and S texture components appear with higher intensity, but also Cube and CG26.5 are present. Looking closely at the volume fractions, Table 4.6, differences between the main components can be noticed. In detail, the S component is higher for the side sample rather than the top, with volume fractions 42.9% and 34% respectively, while Brass amount is almost similar between them (27.9% and 30.1%). Moreover, the Cube fibre fraction (Cube-Goss-CG26.5) is higher for the top sample by 47.4%, reaching from 9.7% for the side to 14.3% for top.

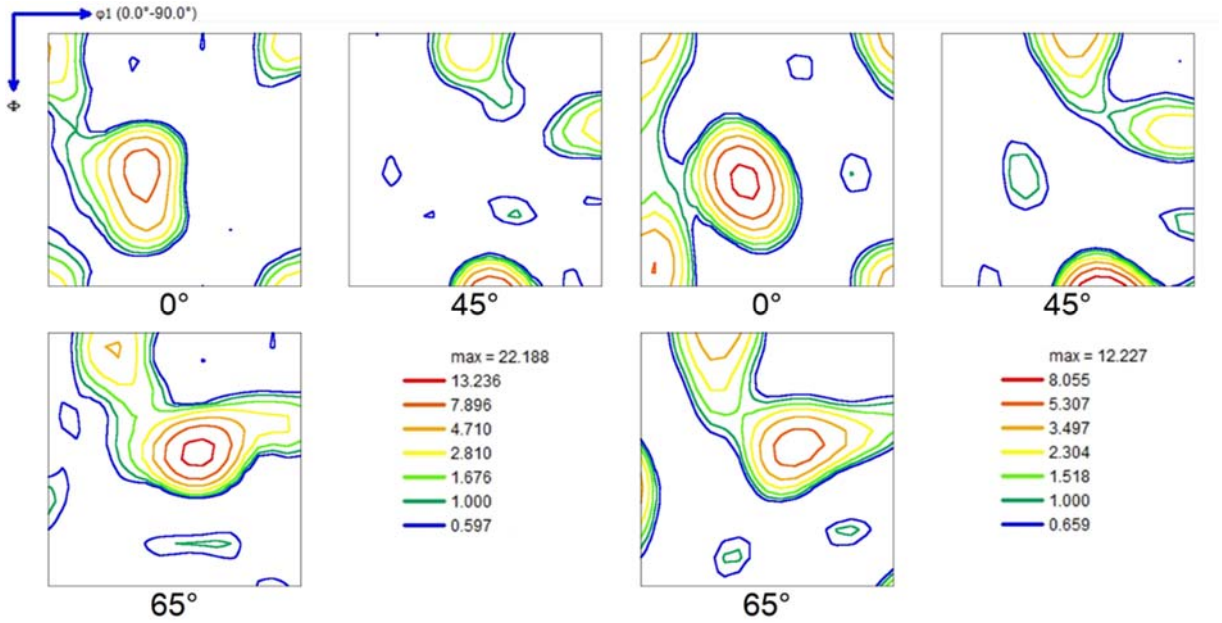

Fig 4.4 ODF sections (φ2 = 0°, 45° and 65°) of the side and the top of the extruded profile.

Table 4.6 Volume fraction of the main texture components of the side and the top of the extruded profile.

Sample	Brass {110}<112>	Copper {112}<111>	S {123}<634>	Cube {001}<100>	Goss {011}<100>	CG26.5 {021}<100>	Total Cube fibre (Cube-Goss-CG26.5)
Side	27.9	5.3	42.9	5.7	1.1	2.9	9.7
Top	30.1	8.4	34	8.2	1.2	4.9	14.3

4.6 Discussion

The determination of the right extrusion parameters can crucially affect the final microstructure and properties.

The increase of extrusion speed from 6 to 9 m/min resulted in an increase of the exit temperature by 10ºC. Higher extrusion speeds result in generating more heat, by plastic deformation, friction between the billet and the container and shearing at the dead metal zone. Extruding at higher temperatures reduces the flow stress and therefore deformation is easier [69]. That can also be translated in larger section reductions and higher productivity.

The Zener-Hollomon parameter is a temperature-compensated strain-rate that often is defined as:

$$Z = \dot{\varepsilon}\, exp\left(\frac{Q}{RT}\right) \tag{4.1}$$

where,

έ (s^{-1}) is the mean equivalent strain rate.

R is the universal gas constant (8.314 J/ K mol).

And Q (kJ mol^{-1}) the activation energy for deformation.

Z increases with the increase of έ or the decrease of T. Microstructure changes that are deformation induced can be interpret by this parameter.

The flow stress during the steady state of the extrusion is then:

$$\bar{\sigma} = \frac{1}{\alpha}\, Ln\left\{\left(\frac{Z}{A}\right)^{1/n} + \sqrt{\left(\frac{Z}{A}\right)^{2/n} + 1}\right\} \tag{4.2}$$

where A, a and n are constants within the extrudable temperature range.

The increase of extrusion speed, and furthermore the exit temperature, had as an effect the increase of the average grain size from 4.23 μm to 6.13 μm. Similar increase can be found in the literature for extruded Al-Mg-Si-Cu rods [70]. Park et al. reported that high Z resulted in finer microstructure and weaker texture. Moreover, in the same study was shown that textural strengthening can be achieved by increasing ram speed [71]. In the literature there are connections made between extrusion speed and mechanical properties. Karabay et al. reported that increase of extrusion exit speed, of different diameter rods, resulted to increase of UTS [72]. Moreover, Aytac et al. showed that increase of extrusion speed from 3 mm/s to 6 mm/s led to hardness increase but further increase to 10 mm/s had an opposite effect [73]. Rahim et al. showed that for a constant extrusion temperature, speed affects the inhomogeneity of the final product [74]. Thus, higher ram speed leads to higher inhomogeneity for the extrudate. As reported from Zhang et al. extrusion speed and temperature have a great impact on microstructure through the cross section of the extrudate [75]. During extrusion of AA6N01, the initial coarse equiaxed grains transformed into fine equiaxed grains as a result of dynamic recovery and dynamic recrystallization. Moreover, extrusion speed affected the surface layer, making it thicker with increase of speed, and high extrusion speed and temperature resulted into a coarse surface layer. Wang et al. showed that for an Al-Mg-Si-Cu alloy, grain size had a slight effect on strength, but precipitation hardening was the main strengthening mechanism [76]. Furthermore, Zhang et al. investigated the use of numerical simulations. It was shown that the increase of stem speed led to an increase of the extrusion strain and temperature that indicated better weldability [77].
Texture for both extrusion speeds was similar, Brass-S and Cube fibre (Cube-Goss-CG26.5). This texture resembles the rolling texture, usually forming at large rolling deformation stages of cold rolling [19,77,78]. The increase of extrusion speed affected S component which increased by 43.1%. At the same time Cube fibre (Cube-Goss-CG26.5) decreased by 48%. Brass seemed not to be affected by the extrusion exit speed. Moreover, the yield strength increased by 12 MPa.

From investigation of right-hand side and top of the profile fabricated at high extrusion speed (B), the yield strength difference between side and top was found to be ~13 MPa. Top side, with the thicker grains, showed the lower mechanical performance. The comparison of texture components volume fractions of the top and side indicated the effect of each component on mechanical properties. S component was 26.1% higher for the side, while Cube fibre was 47.4% higher for the top. Cube {001}<100> component was the main component of the Cube family. S and Cube orientations have a 40º <111> orientation relationship and in many cases, S had been considered

responsible for the formation of Cube texture. Moreover, S and Cube, belonging in different <uvw> direction families have different effect on mechanical properties. The Taylor factor, which is applicable for multiple slip in at least five independent (111)<110> slip systems has been studied in the literature. The S component has been found to have higher Taylor factor than Cube component for alluminium subjected to uniaxial tension [79,80].

4.7 Conclusions

- The increase of the extrusion exit speed, from 6 m/min to 9 m/min, and furthermore the increase of exit temperature, increased the average grain size of the extrudate by 44.8% and resulted to a 12 MPa increase.
- The overall texture of the extruded hollow rectangle was Brass-S-Cube for both extruded speeds. The increase of extrusion exit speed resulted to a 43.1% increase of S and a 51.8% decrease of Cube fibre, while Brass remained consistent.
- A 13 MPa yield strength difference between the sides of the profile was noticed. From the texture analysis, a 26.1% increase of S component, and a 32.1% decrease of Cube fibre, of the side of the profile was reported.
- The strength difference both between the different extrusion speeds and between sides can be explained by texture. The increase of S component and simultaneously decrease of Cube fibre resulted to the increase of yield strength.

Chapter 5 Effect of extrusion profile

5.1 Introduction

The extruded products can take different profile shapes, such as solid or hollow rectangles, bars and flat bars, depending on the applications. For their production various extrusion parameters are involved, such as extrusion ratio, extrusion speed and temperature. The extrusion processing conditions have a significant influence on the resultant microstructure (grain size and texture) and the mechanical properties. This chapter is concerned with the study of the microstructure, texture and mechanical properties of extrusion as a function of extrusion profile, extrusion ratio, extrusion speed and extrusion exit temperature using a combination of EBSD, XRD and tensile testing methods.

Four different die shapes were used for this investigation. A hollow rectangle, a solid bar, a flat bar, and a bulk bumper tow nut. The profiles except their geometry had also different extrusion ratio, Fig 5.1. The extrusion ratio (ER) is defined as the initial cross section area (A_1) over the final cross section area (A_2), as given by equation 5.1.

$$ER = \frac{A_1}{A_2} \tag{5.1}$$

Moreover, the introduced effective plastic strain (ε_{eff}) is defined as follows in equation 5.2:

$$\varepsilon_{eff} = \ln(ER) = \ln\left\{\frac{A1}{A2}\right\} \tag{5.2}$$

The extrusion ratio indicates the amount of plastic deformation introduced to the extrusion [81]. A high extrusion ratio results in high mechanical work since excessive pressure is necessary to force the metal through the die.

In order to keep these four extrusion trials as similar as possible, they were all extruded with the aim to reach a comparable extrusion exit temperature by using different extrusion speeds, as listed in Table 5.1.

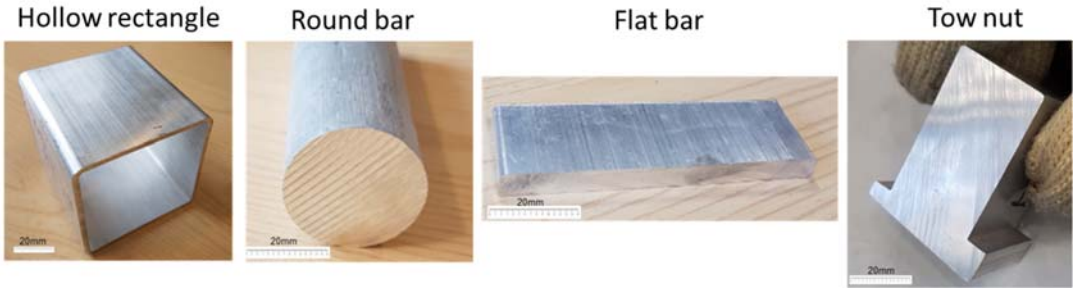

Profile	Hollow rectangle	Flat bar	Round bar	Tow nut
ER	30	50	20	10

Fig 5.1 Images and extrusion ratios (ER) of the four extruded profiles.

Table 5.1 Extrusion parameters of the 4 profiles.

Profile	Extrusion exit speed (m/min)	Exit T (ºC)
Flat bar	9.6	540
Hollow rectangle	6.2	551
Round bar	8.5	560
Tow nut	7	552

All EBSD scans have been produced on the ND-ED plane and the results are presented in respect of the normal plane (ED-TD) for comparison reasons, as shown in Fig 5.2. By this way, the “pancake” effect of the grains is observed, which was expected for the extruded material.

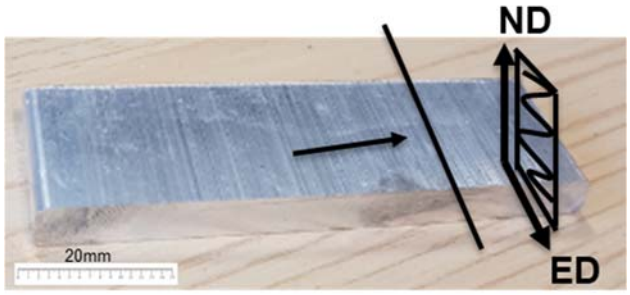

Fig 5.2 Schematic representation of the plane used for EBSD scans of all the four profiles.

5.2 Microstructure of the various extrusion profiles

The IPF maps of the four profiles in the as-extruded condition are presented in Fig 5.3. The areas being presented here were taken at the middle of the half cross-section, except the tow nut that it was taken at the centre of the cross-section. These scans were obtained from the ND-ED plane and the data were plotted according to the normal plane (ED-TD). As it is clear, the four profiles can be grouped at those with high extrusion ratio (ER) and microstructurally their grains are thinner (flat bar and hollow rectangle) and those with small ER and thicker grains (round bar and tow nut). In detail, the average grain size as well as the high and low angle grain boundaries can been found in Table 5.2. Moreover, colour gradient can be observed inside the grains from all four IPF maps. This colour change indicates a misorientation inside the grains due to remaining strain from defects piled up during extrusion.

The amount of HAGB and LAGB between flat bar and hollow rectangle is comparable, with the hollow rectangle having 15% and 22.5% higher HAGB and LAGB than the flat bar. Between round bar and tow nut the amount of LAGB is the same but the amount of HAGB for the tow nut is 82% higher than the round bar's.

Table 5.2 Average grain size (and standard deviation), high (15º-65º) and low (5º-15º) angle grain boundaries of the four profiles.

Sample	Av.Grain Size (μm)	HAGB (fraction)	LAGB (fraction)
Flat bar	5.45 (0.015)	0.44	0.20
Hollow rectangle	6.13 (0.125)	0.51	0.25
Round bar	17.17 (0.009)	0.23	0.16
Tow nut	14.97 (0.026)	0.42	0.16

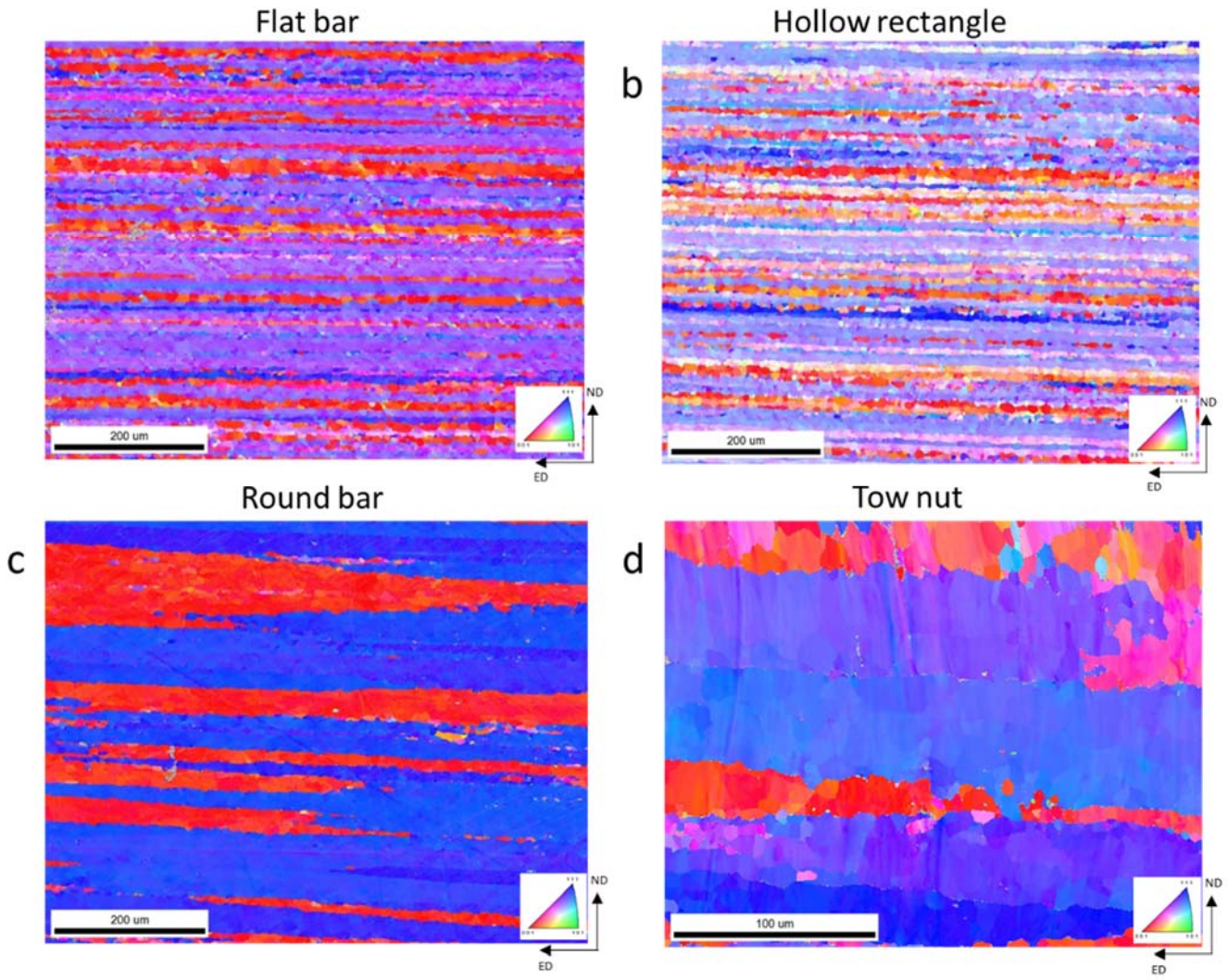

Fig 5.3 IPF maps of the extruded profiles in the as-extruded condition: a) flat bar, b) hollow rectangle, c) round bar and d) tow nut.

5.3 Development of grain structure through thickness of the profile studied by multiple EBSD scans

Apart from the smaller areas presented previously, the investigation of the grain structure development through thickness of extrusion profile was found particularly interesting. Figs 5.4 a-c, show IPF maps of hollow rectangle taken from the inner to the outer side, flat bar taken from the top to the bottom and round bar taken from the centre to the edge, respectively. The tow nut was split in three areas, as shown in Fig 5.5 a and b, and multiscans were performed on samples taken from the top edge to the centre of area a, the middle of area b and c and the very edge of c, as shown in Fig 5.5 d. Subsequently, from the 54 mm length of the profile, approximately the 33 mm were scanned.

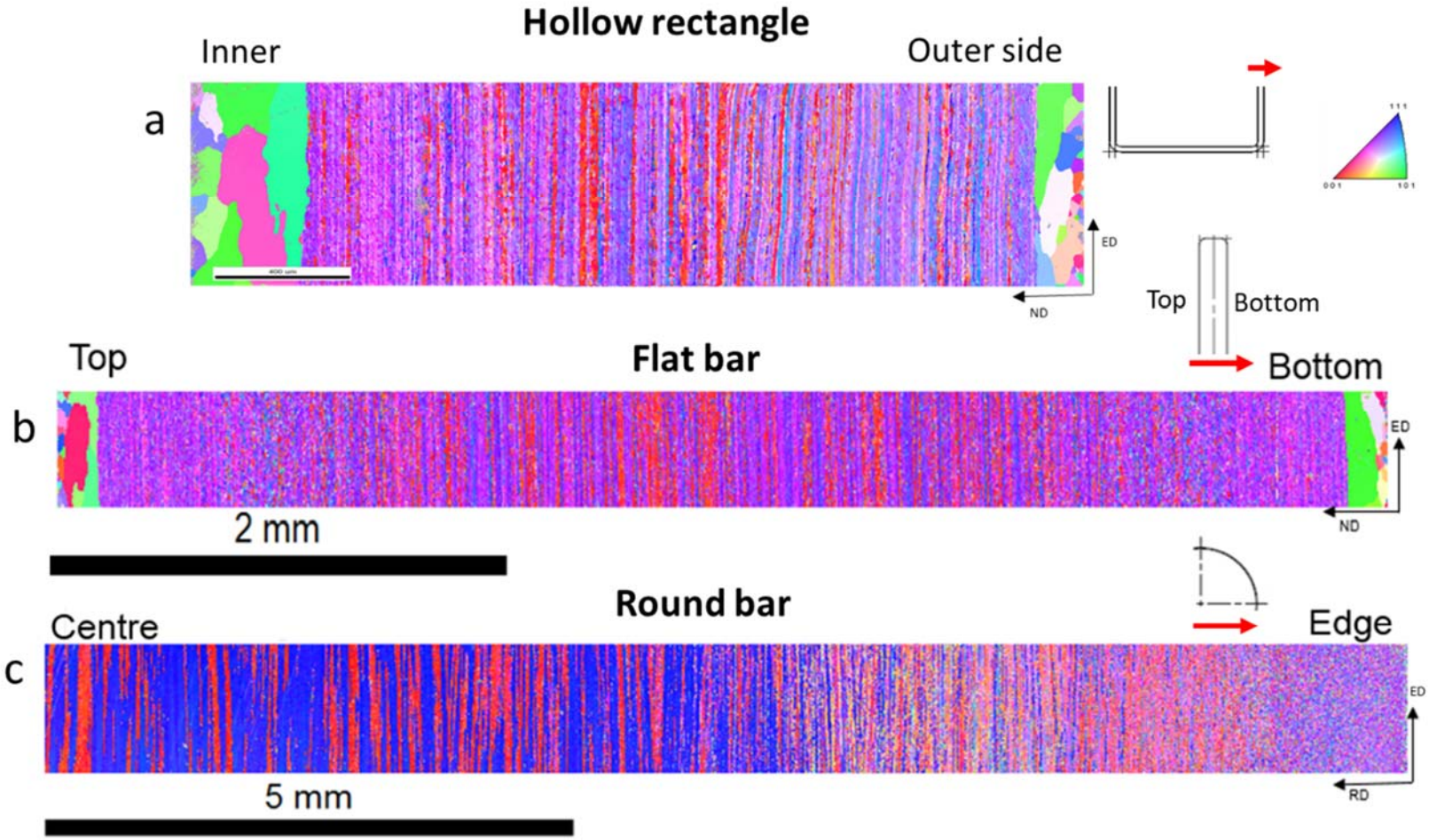

Fig 5.4 IPF maps of the whole cross section of a) hollow rectangle and b) flat bar and c) half cross section of the bar.

The hollow rectangle and the flat bar showed a similar, strong morphological symmetry at the centre of the cross section. It is particularly interesting to note that the peripheral coarse grain (PCG) layer at the inner side of the hollow rectangle was 2.45 times thicker than that of the outer side, with an average PCG layer thickness of 91 μm for the outer and an average PCG layer thickness of 224 μm for inner side. This can be attributed to the lower quenching rate at inner side of the hollow rectangle. Moreover, similarities of the microstructure can be observed also for the round bar and the tow nut. The grains of round bar and tow nut once more were elongated along the extrusion direction but were coarser than the flat bar and hollow rectangle ones. Additionally, for round bar and tow nut an important change of the grain size from edge to centre can be noticed, with the increasing grain size from the edge to the centre.

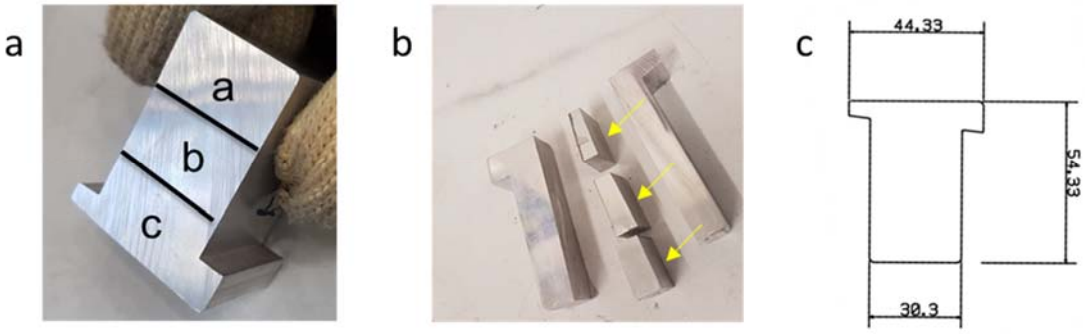

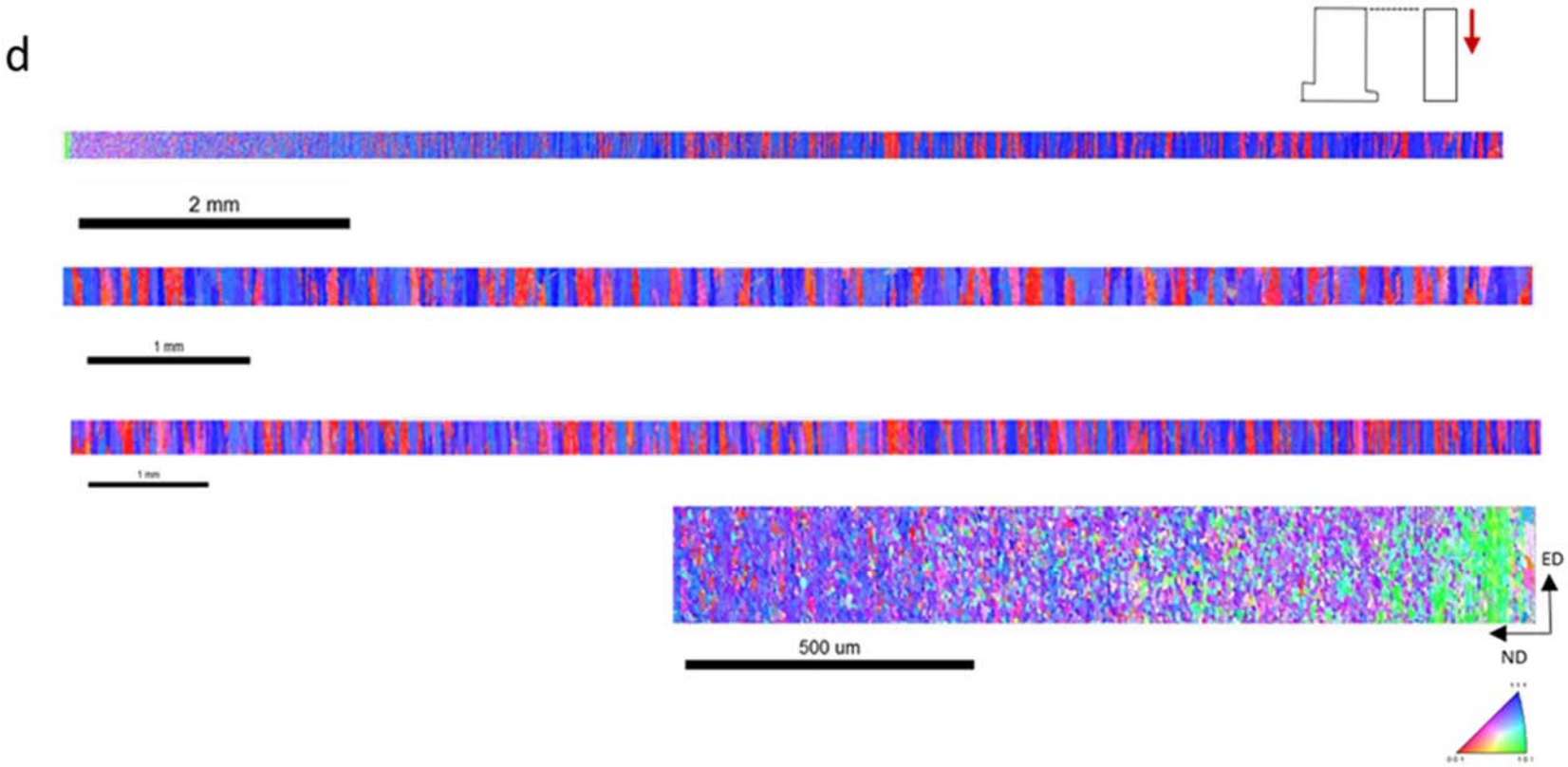

Fig 5.5 Tow nut profile: a) separated in three areas, b) indicating the plane of the through thickness EBSD scans, c) dimensions and d) IPF maps of area a, b, c and edge of c

To be able to investigate the through thickness grain size distribution, the half cross sections of these four profiles were divided into three equal areas, starting from the edge and moving to the centre; the PCG layer observed at the hollow rectangle and flat bar was avoided at this point. In all cases, the grains were found to be finer at the edge of the cross section and became coarser towards the centre of the extrusion profile. But the through thickness grain size distribution was different between profiles with small and large ER, as shown in Table 5.3. For profile with ER between 30-50, the grain size increment between the edge and centre of the extrusion profile seemed to be inversely proportional to ER. For example, the flat bar profile with the highest ER of 50, had a 19% increase of the grain size between the edge and the centre, while hollow rectangle profile with ER of 30, had a 37.5% increase in grain size from the edge to the centre. For the profiles with ER between 10-20, the grain size increment between the edge and centre of the profile appeared to be proportional to the ER. For example, the tow nut profile with ER of 10, had a grain size increment of 71.2% as compared to the three times grain size increment in the round bar profile with ER of 20.

Table 5.3 Average grain size (μm) and standard deviation in parenthesis from edge to centre.

Area	A (edge)	B (intermediate)	C (centre)	Grain size increment (%) (edge to centre)
Hollow rectangle	3.47 (0.022)	3.95 (0.020)	4.77 (0.020)	37.5
Flat bar	4.41 (0.096)	4.63 (0.008)	5.25 (0.008)	19
Round bar	4.89 (0.005)	7.94 (0.004)	14.40 (0.003)	194
Tow nut	7.58 (0.004)	10.80 (0.012)	12.98 (0.006)	71.2

5.4 Texture of various extrusion profiles

The four extrudates can, once more, be classified into two groups: those with higher ER (hollow rectangle and flat bar) and those with lower ER (round bar and tow nut) profiles, this time based on their textures. As it can be observed from the ODF maps, Fig 5.6, for the middle of the half cross sections (same areas as previously presented the microstructure), the texture of the higher ER profiles resembled rolling texture with a combination of Brass, S and Cube components while for the lower ER profiles, the texture was extruded with Cu, Brass and Cube.

As a result of the size of the tow nut, Fig 5.4 c, a scan at the centre of each of the three areas was performed, for the better understanding of the texture through the cross section. Texture was similar for areas a and c, with rotated Brass being the predominant component, while for area b, Cu and P are present, as shown in Figs 5.6 (d-f).

These results were further compared with XRD texture analysis, and the results are being presented below.

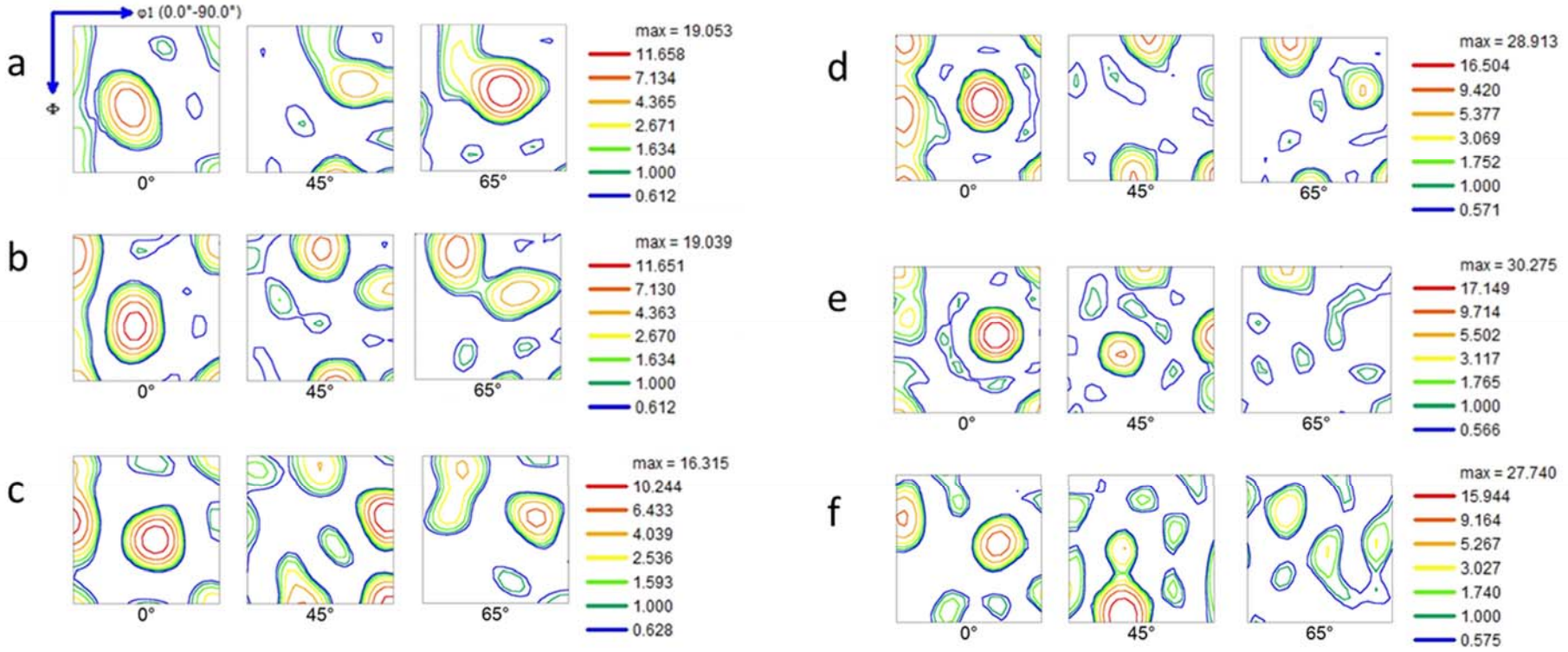

Fig 5.6 ODF sections (φ2 = 0°, 45° and 65°) of a) Hollow rectangle, b) Flat bar, c) Round bar, d) Tow nut taken from area a in Fig 5.5, e) Tow nut taken from area b in Fig 5.5 and f) Tow nut taken from area c in Fig 5.5.

For the hollow rectangle and the flat bar, the predominant texture component was found to be S, with volume fractions 43.1% and 41.5% respectively, as shown in Table 5.4. Brass was the second major texture component, with 24.5% for hollow rectangle and 20.8% for flat bar. Cube fibre (Cube-Goss-CG26.5) texture was found to be 22.6% for flat bar and 12% for the hollow rectangle. Both profiles contained a small amount of Copper texture with 5.3% for hollow rectangle and 8.7% for flat bar.

Round bar showed an extruded texture, with Copper being the stronger component, with 31.7% volume fraction, and Brass following with 23.3%. It must be noticed that Brass was rotated by 20º and on the ODF map appears at 55º rather that 35º. The volume fraction of Cube fibre (Cube-Goss-CG26.5) was 29.7%.

Tow nut's areas a and c had 37.1% and 14.6% Brass, rotated at 55º, respectively. However, Copper was present with 12.7% in area a and only 3.6% for area c. Moreover, for area c, P texture component was present with 22.9%. Texture at the middle of tow nut, area b, was different. The main texture components were Copper, with 35.1% volume fraction, and P component, with 27.3%, as shown in Table 5.4.

Table 5.4 Volume fraction of the main texture components of the four extruded profiles.

Profile	Brass {110}<112>	Copper {112}<111>	S {123}<634>	Cube {001}<100>	Goss {011}<100>	CG26.5 {021}<100>	P {011}<122>	Total Cube fibre (Cube-Goss-CG26.5)
Flat bar	20.8	8.7	41.5	11.6	0.7	10.3	-	22.6
Hollow rectangle	24.5	5.3	43.1	3.6	2.5	5.9	-	12
Round bar	R(20°)23.3	31.7	5.9	5.8	13.7	10.2	0.7	29.7
Tow nut a	R(20°)37.1	12.7	2.1	12.2	11.9	11.5	1.6	35.6
Tow nut b	R(20°)0.4	35.1	0.3	5.7	2.2	6.5	27.3	14.4
Tow nut c	R(20°)14.6	3.6	0.3	0.8	2.3	10	22.9	13.1

5.5 X-ray Diffraction analysis

As it can be observed from the XRD ODF maps, Fig 5.7, the hollow rectangle and the flat bar demonstrated rolling texture, with Brass-S and some Cube texture components. The round bar showed a strong extruded texture, with Copper-Brass and Cube fibre. The Brass component was found to be strongly rotated, by 20º around ND, thus from the 35º that normally appears here was at 55º.

The tow nut was divided into three areas, A, B and C, as it is presented in Fig 5.8. For areas A and C, a similar, strong, extruded texture, with Copper-Brass and presence of Cube fibre was reported. Again, Brass was rotated at 55º. For the middle of the tow nut, area B, the texture resembles rolling S-Copper-Brass, also with presence of Cube fibre. In this case, Brass was present at 45º, rotated by 10º from the ideal, a presentation of Brass common for extruded material. Finally, a small amount of P component was present in areas A and C, with their volume fractions being 7.9% and 11.8% respectively.

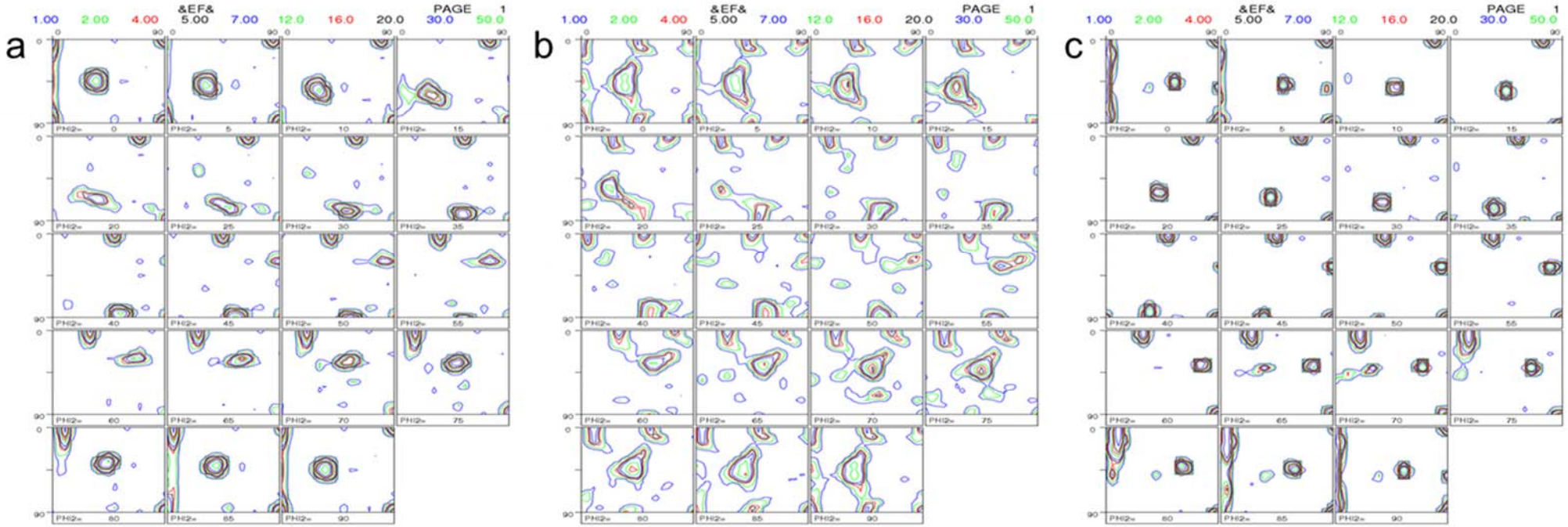

Fig 5.7 ODF maps obtained from XRD of a) flat bar, b) hollow rectangle and c) round bar.

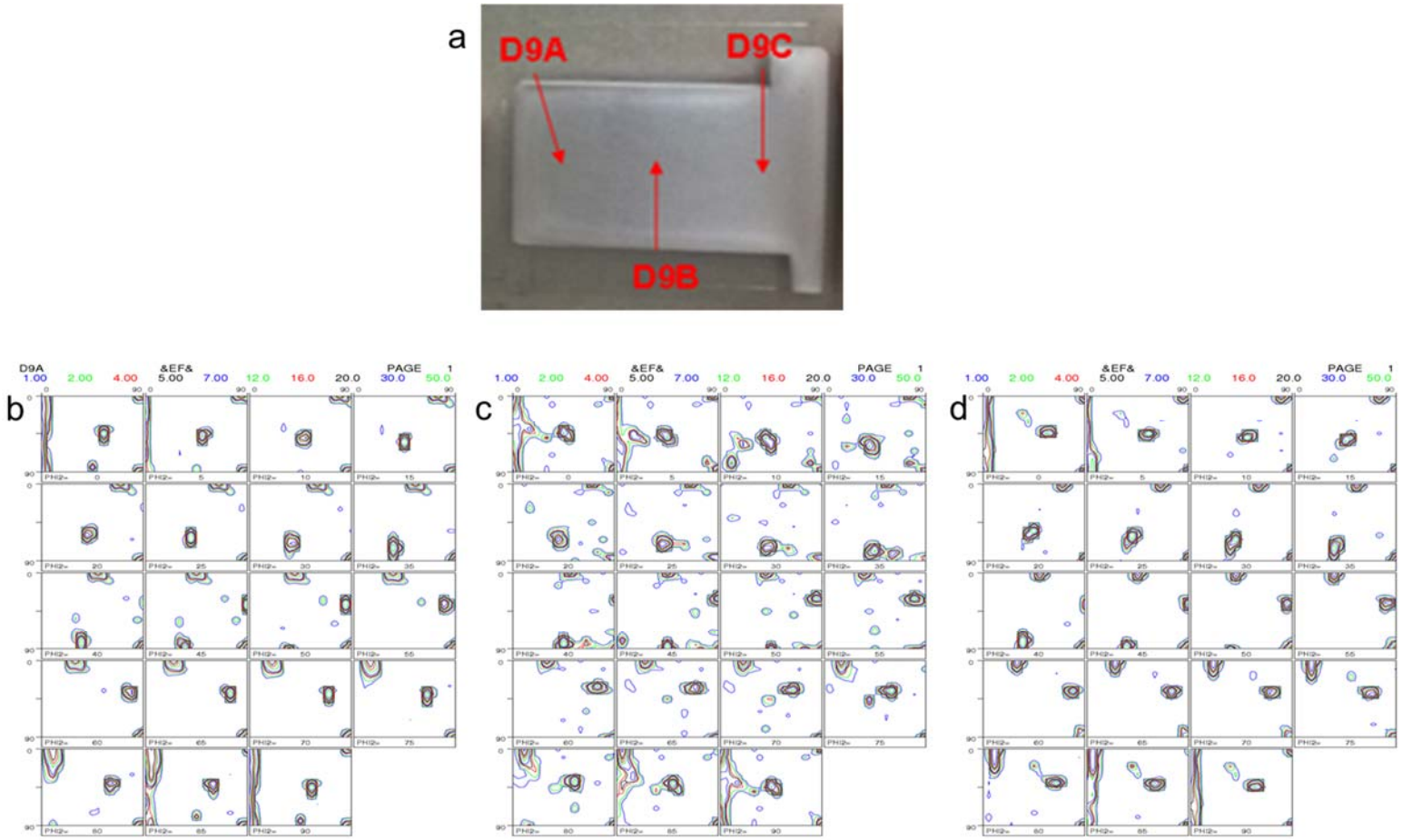

Fig 5.8 Tow nut's: a) cross-section for XRD texture analysis and the areas (A, B and C) that was devided, and the corresponding ODF maps obtained from XRD of b) area A, c) area B and d) area C.

In general, there was a good agreement between localized EBSD and macroscopic XRD texture results. The texture presented for hollow rectangle, flat bar and round bar was comparable. Some differentiations were noticed for the tow nut, especially for the middle of the cross-section. Specifically, Brass and S were absent with EBSD, while were present with XRD. At the same time, the presence of P component reported with EBSD was confirmed by XRD.

5.6 Texture development through thickness of the profiles studied by multiple EBSD scans

The texture deviation through thickness of each profile is presented here. The analysis has been done at the same areas as the previous through thickness microstructural analysis.

Fig 5.9 presents the deviation of the main texture components found in the profiles in respect to the cross-section distance. Hollow rectangle had the same Brass-S-Cube texture through the whole cross-section with some noticeable changes of texture components. Brass component increased at the edge of the cross-section, reaching 36.5% volume fraction, while it was 28.6% at the centre. S component had similar volume fractions for edge and intermediate areas, ~38.5%, but showed a small decrease at the centre, reaching 31.4% volume fraction. Moreover, Cube fibre (Cube-Goss-CG26.5) fluctuated from 10.4% for the centre, to 13.1% for intermediate area and 9.2% for the edge. Finally, a small amount of Copper was present at edge and intermediate areas (5.5%) but decreased significantly (1.9%) reaching the edge.

For the flat bar, the Brass's volume fraction increased from centre to the edge. Specifically, it was 32.1% for the centre, 37.8% for intermediate area and 51.9% for the edge. This is a 61.6% increase of Brass component. S component was at similar levels for all the three areas, ~30%. Cube component increased importantly from the edge to the centre, almost quadrupled the volume fraction. From 3.7% for the edge, reached 12.9% for intermediate area and 14.6% for the centre.

Round bar displayed a very interesting deviation of texture through cross-section. The overall texture was Copper-Brass-Cube fibre. For centre and intermediate areas, Brass was strongly rotated at 55º, a 20º rotation from its usual presence, with volume fractions 17.1% and 12.5% respectively. For the edge of the cross-section, Brass returned at 35º and its volume fraction was 15.3%. Copper decreased significantly from centre to edge. The volume fractions were 35.3% for the centre, 26.9% for intermediate area and 7.5% for the edge. The amount of Copper at the edge is 4.7 times less than the centre. Moreover, Cube fibre had a decrease from centre to edge. The volume fractions were 29.4% for centre, 18.1% for intermediate area and 13.8% for edge. Finally, a small amount of P component was present at the centre (4.2%), decreased to 1.9% at the intermediate area and 1.4% at the edge.

Deviation through tow nut's cross-section was also present. Similar to round bar, Brass component was rotated at the centre and the intermediate area, with the volume fractions being 7.5% and 20.9% respectively. Copper component, similarly to rotated Brass, was stronger for the intermediate area than the centre, with their volume fractions being 34.7% and 25.7%. At the edge, Copper decreased significantly to 9.5%. Cube fibre had similar volume fraction at the centre and the intermediate area, ~25%, while decreased at 3.1% at the edge, 8 times less. P component had a 15.8% volume fraction at the centre, decreased to 3.5% at the intermediate area and finally almost disappeared at the edge (0.3%).

a

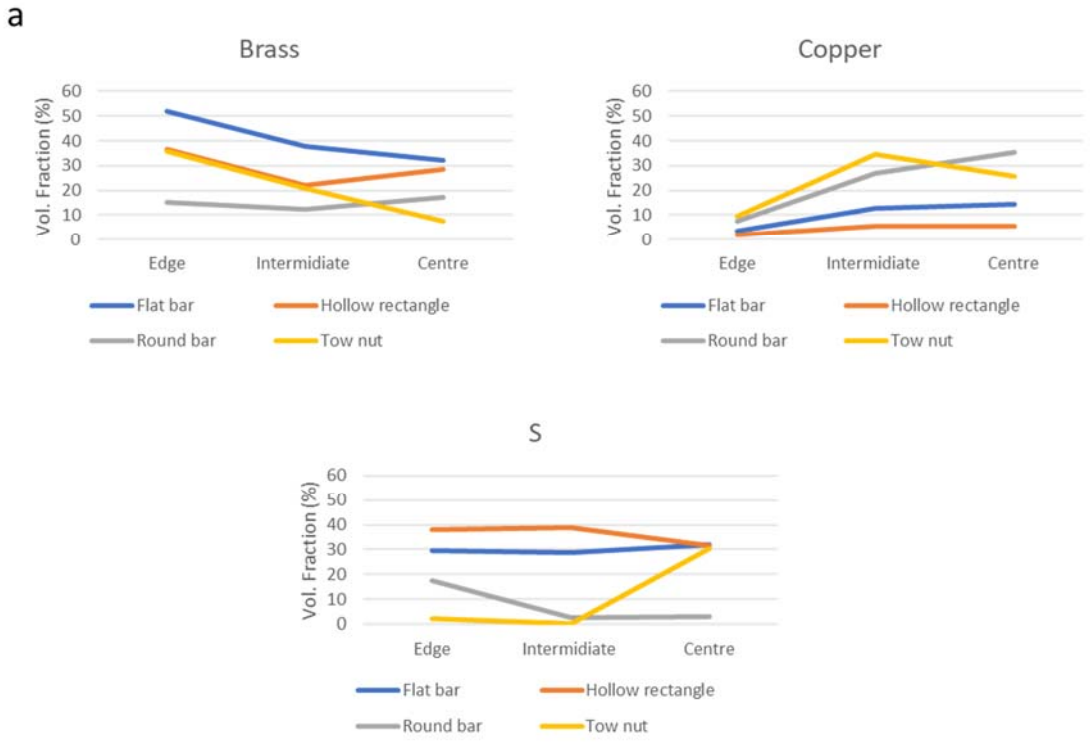

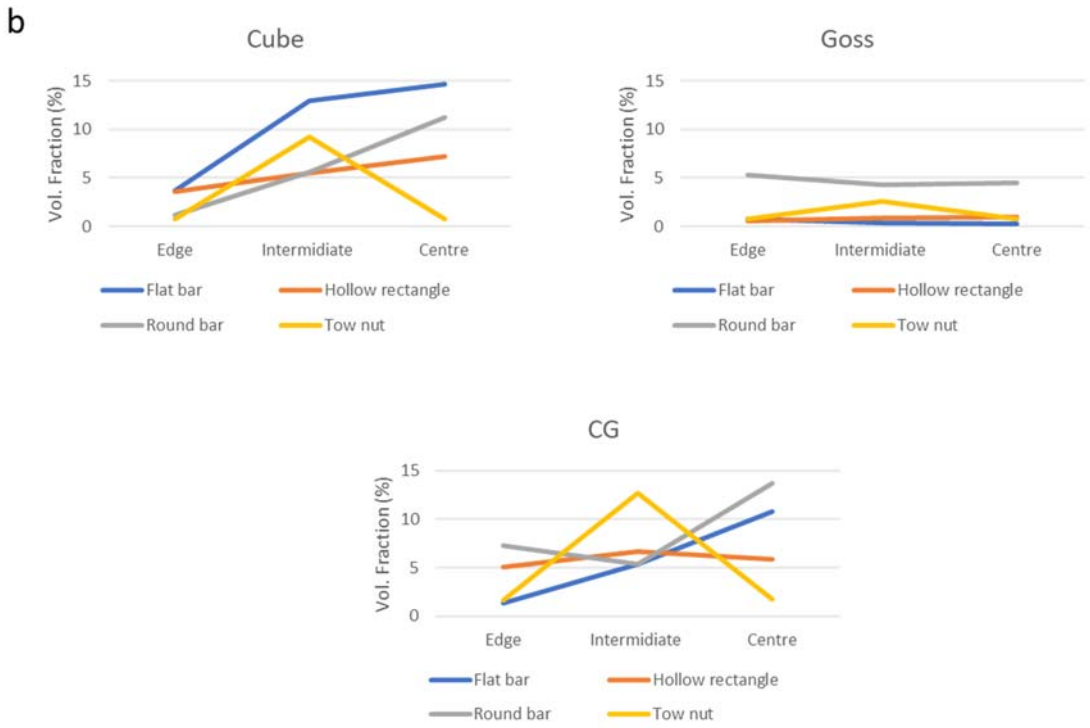

Fig 5.9 Volume fractions of a) deformation (Brass, Copper, S) and b) recrystallization (Cube, Goss, CG26.5) components for the four profiles in relation to the area of the cross-section.

5.7 Study of Kernel average misorientation (KAM) of various profiles

EBSD analysis has a variety of tools for the investigation of elastic and plastic strains. With the use of these tools, we can monitor the differences of orientation between neighbouring points.

A common approach to investigate the stored strain energy is through Kernel average misorientation (KAM). Using a kernel misorientation approach the local misorientation of a point can be characterized, with respect to its nearest neighbours [82]. A maximum misorientation (tolerance) is necessary and in this case was set at 5º. Usually, grains that have been highly deformed have higher KAM due to higher dislocation density [83].

It should not be overlooked that KAM is affected by scan step and for maps with different step size a compare of KAM is not feasible. For this investigation, the scan step size was set at 0.5 μm for all the samples.

As it is presented in Fig 5.10 the distribution for the hollow rectangle was relatively sharp with small mean value of 0.62º. Round bar followed with 0.79º and almost the same distribution was obtained for the flat bar, with 0.81º mean value. Lastly, tow nut's KAM was widely distributed, with an average at 1.51 degrees. Moreover, the number fraction more than 1º, $f_{[\theta>1]}$ was 14%, 8%, 13% and 49% for flat bar, hollow rectangle, round bar and tow nut respectively.

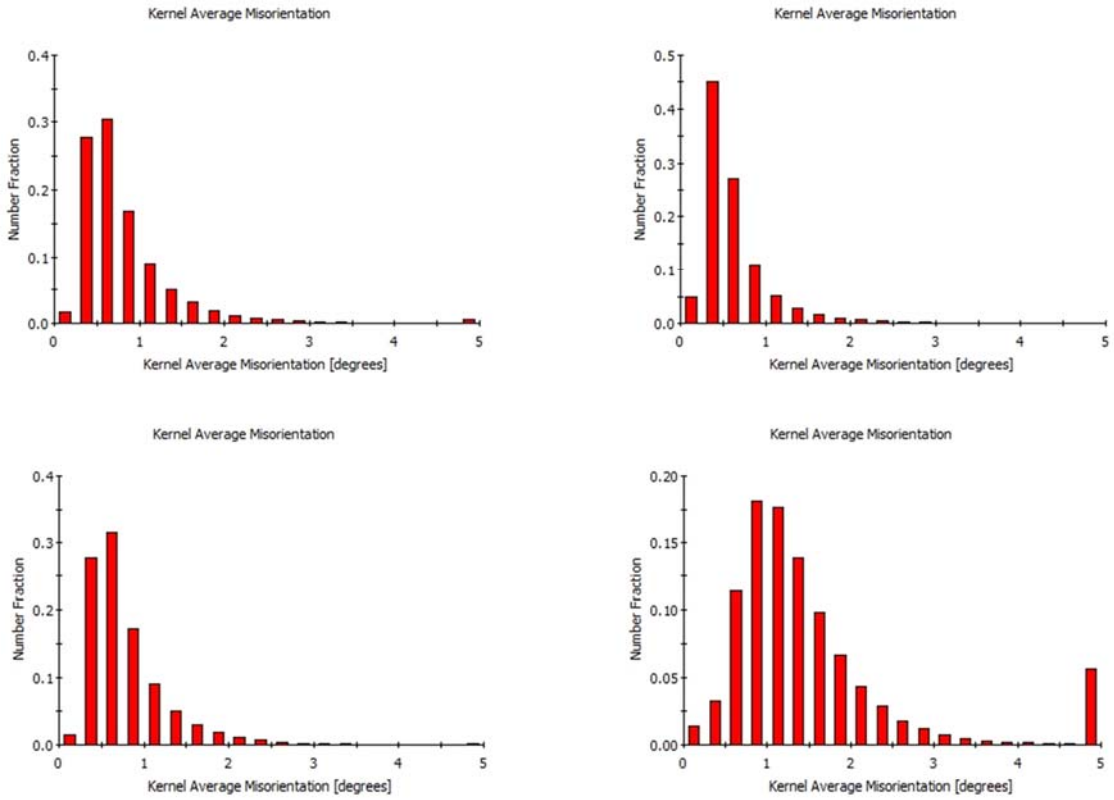

Fig 5.10 Histograms of kernel average misorientation (KAM) for the a) flat bar, b) hollow rectangle, c) round bar and d) tow nut profiles.

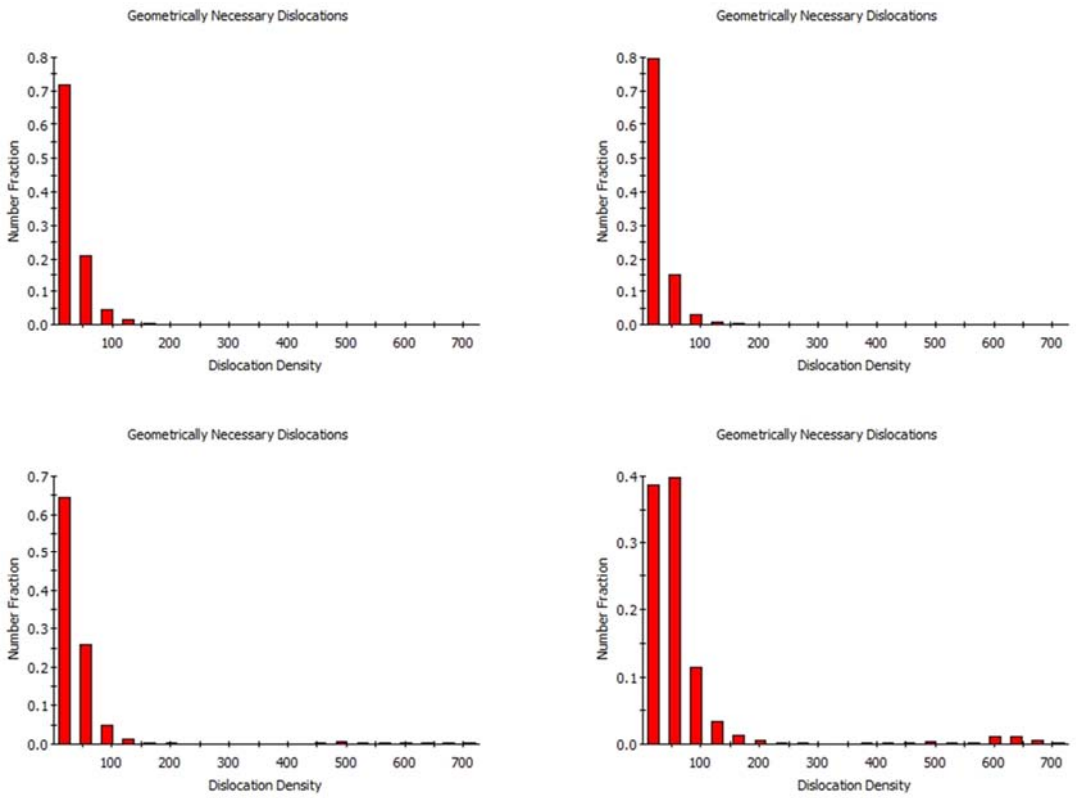

Fig 5.11 Histograms of geometrically necessary dislocation (GND) for the a) flat bar, b) hollow rectangle, c) round bar and d) tow nut profiles.

The histograms of geometrically necessary dislocation (GND) of the four profiles are presented in Fig 5.11. The density of GND was calculated from the local misorientations and it is given in terms of $1x10^{12}m^{-2}$. The calculation method is according to D.P. Field et al. [84]. Again, a maximum misorientation (tolerance) should be determined and in this case is 5 degrees..

The mean GND density for the flat bar was found to be $36.31x10^{12}m^{-2}$, the hollow rectangle $32.37\ x10^{12}m^{-2}$, the round bar $48.83\ x10^{12}m^{-2}$ and $75.08\ x10^{12}m^{-2}$ for the tow nut, Table 5.5.

Table 5.5 Mean GND density and extrusion ratio of the four profiles.

Profile	ER	Mean GND density (m^{-2})
Flat bar	50	36.31×10^{12}
Hollow rectangle	30	32.37×10^{12}
Round bar	20	48.83×10^{12}
Tow nut	10	75.08×10^{12}

5.8 Mechanical properties

Uniaxial tension specimens were extracted from the extruded profiles along the extrusion direction for mechanical testing. As is can been observed in Table 5.6, the mechanical properties have a similar grouping of the profiles to microstructure and texture. The two lower ER profiles showed the higher yield strength, with the round bar reaching 408.1 ± 3.4 MPa and the tow nut 400.1 ± 8.4 MPa. From the two higher ER profiles, the flat bar reached 362.6 ± 0.6 MPa and the hollow rectangle 342.7 ± 6.8 MPa. The ultimate tensile strength followed the same trend. Uniform elongation was higher for hollow rectangle and flat bar (12.45 and 10.37), while it was lower for bar and tow nut (8.61 and 8.37).

Table 5.6 Tensile properties of the four extruded profiles in T6 condition.

Sample	YS (MPa)	UTS (MPa)	EL (%)	n-value
Flat bar	362.6 ± 0.58	413.4 ± 0.49	10.37 ± 0.42	0.14
Hollow rectangle	342.6 ± 0.58	389.4 ± 5.26	12.45 ± 0.49	0.086
Round bar	408.1 ± 3.43	448.5 ± 2.24	8.61 ± 0.93	0.062
Tow nut	400.1 ± 8.4	446.2 ± 4.1	8.37 ± 0.08	0.089

Moreover, the mechanical properties of tow nut were further investigated, for the centre of each area, a, b and c. The results revealed a decrease of yield strength for area b, reaching 386.4 ± 4.1 MPa, while area a and c reached 406.2 ± 5.64 MPa and 404.4 ± 5.3 MPa respectively. Ultimate tensile strength followed the same trend. Uniform elongation followed the same trend as yield strength, with the higher elongation for area a (8.15), followed by c (7.75) and finally b (7.4), something that is not usual for this type of alloys, Table 5.7.

Table 5.7 Tensile properties of the three areas of tow nut in T6 condition.

Sample	YS (MPa)	UTS (MPa)	EL (%)	n-value
a	406.5 ± 5.64	448.4 ± 2.17	8.15 ± 0.05	0.078
b	386.4 ± 4.1	429 ± 3.52	7.4 ± 1.3	0.077
c	404.4 ± 5.3	446.4 ± 2.6	7.75 ± 0.15	0.079

5.9 Discussion

5.9.1 Effect of extrusion profile geometry on grain size

Optimized extrusion conditions were used to produce the four profiles. This was based on a combination of maximum productivity and final properties. As a result, there were differences of the exit temperature. The bar had the higher extrusion exit temperature, 560 ºC, tow nut and hollow rectangle follow with 552 ºC and 551 ºC and finally flat bar had 540 ºC.

The average grain size close to the center of the cross-sections was higher for the bar, with the tow nut, hollow rectangle and flat bar following. This comes in agreement with the higher extrusion exit temperature. The same effect of extrusion exit temperature on grain size was reported in Chapter 4. A proposed explanation to the way exit temperature affects the grain size is that the grains transition from non-dynamic recrystallized to dynamic recrystallized as the extrusion temperature increases [85]. Comparing the average grain size of the profile with the smallest ER (tow nut with ER 10) and the profile with the biggest ER (flat bar with ER 50) an increase of 2.7 times was found. A small extrusion ratio would indicate smaller billet surface in contact with the container and the die, resulting to less shear stress and work hardening [86]. As a result, tow nut and bar had very different microstructure than flat bar and hollow rectangle, with thick grains elongated through the extrusion direction.

The microstructure was very similar for the hollow rectangle and flat bar. The grains were flattened and elongated through the extrusion directions. Many grains with serrated grain boundaries can been noticed as well as smaller grains that have been pinched-off from bigger, initial ones. This phenomenon is attributed to geometric dynamic recrystallization (GDRX), and it comes in agreement with the literature [87,88]. Bar and tow nut had a different microstructure. The grains were again elongated through the extrusion direction, but they were much thicker than the other two profiles.

The differences of the strain distribution during extrusion process reflects on the microstructural and textural deviation through the extrudate cross-section [81]. These deviations resemble the rolling procedure [82]. For all the profiles, the grains were thicker at the centre of the cross-section. This is evidential of the two mechanisms taking place during extrusion. Closer to the edge shear stress is higher, leading to recrystallization of the grains, while at the centre recovery is the main mechanisms.

5.9.2 Effect of extrusion profile on the texture components

The effect of geometry on texture has been investigated. Typical texture for extruded aluminium rectangles is a Brass-S-Copper texture, similar to rolling texture. For the hollow rectangle and flat bar of this study, Copper is relatively weak compared to S and Brass. Moreover, by increasing the ER, from 30 for hollow rectangle to 50 for flat bar, the amount of S and Brass decreased while Copper increased.
The extruded bar of this study showed a strong preferred orientation, noticeable from the IPF map. The texture was characterized by strong <111>//ED and <100>//ED fibers. This duplex fibre texture comes into agreement with the literature for extruded and drawn Al alloys [70,91,92].

Kaneko et al. showed that the strong <111>//ED texture of extruded Al-Mg-Si-Cu rods significantly decreased by increasing the ER, while at the same time <100>//ED increased [70]. In our study a comparison like this cannot be achieved. For example, bar, with ER=20 had a 60.9% volume fraction of Brass, Copper and S, while flat bar, with ER=50, had 71%. This is understandable, since the effect of geometry, hence different strain paths, should not be overlooked.

The centre of the tow nut, area b, showed a significant increase of Copper component. At the same time area b had the lowest yield strength, with 386.4 ± 4.1 MPa, ~19 MPa less than areas a and c, that showed similar yield strength. Barlat and Richmond investigated the effect of Brass, S and Copper textures on the yield surfaces of FCC metal sheets [93]. Copper was found to create the most deformed yield surface. Moreover, it has been reported that increased Copper component enhances the strength anisotropy [94].
Furthermore, for tow nut, P component was reported, which was stronger at the centre (15.8% volume fraction) and gradually decreased and eliminated at the edge. P component {011}<122> is not a common texture component in 6xxx aluminium alloys. Jung et al. investigated the nucleation mechanisms of P component and concluded that during strain compression, stable P and near P orientations formed, that acted as nuclei that recrystallized into P component [95]. Moreover, Huang et al. showed that concurrent precipitation subdued nucleation at grain boundaries and allowed the growth of P component [96]. Hu et al. showed that P, Goss and Cube oriented grains have more {111} slipping planes participating in cycle plastic deformation, resulting to reduced stress concentration [97].

The use of XRD texture analysis was decided as a comparative tool. Many times, differences of the texture components volume fractions between EBSD and XRD method have been noticed. These differences arise from the characteristics of each technique. X-rays have a deeper penetration capability (~ 20-30 μm), while EBSD is more surface sensitive since it has a penetration capability ~ 20-30 nm. Moreover, based on the machines layouts, X-rays can scan bulk materials, resulting to measuring more grains than EBSD is capable. For industrial extruded profiles, EBSD would be more of a qualitative technique, while XRD quantitative.
For the flat bar, hollow rectangle and round bar, texture was reported similar with both techniques. For tow nut, the overall texture was similar with both methods, but some differences were noticed. In particular, for area c, XRD texture analysis reported a strong Copper (27.8%) and some P (11.8%) component. EBSD analysis found a very small amount of Copper (3.6%) and strong P (22.9%). Moreover, with EBSD for area b, Brass was not present, and P had a significant volume fraction (27.3%), while with XRD, P was not present and Brass was strong (20.1%).

Khadyko et al. investigated the grains and texture gradients through thickness of an extruded AA6063 flat profile [98]. It was found that the grain size and texture displayed variations through the thickness which is typical for such profiles. In more detail, at the centre of the cross section the grains were smaller, with Cube texture, the following layer had larger grains with random orientation and the outer layer had smaller grains with Goss as the predominant texture. Finally, it was shown that the texture gradient had a smaller effect on the mechanical properties than the global texture and the work hardening. The same trend for Cube was also noticed in the case of the flat bar of our investigation. Moreover, Cube and Brass seemed to develop vice versa through the cross-section.

Anisotropy has been related to the development of specific texture components. Specifically, Brass, S and Copper are the main texture components that their development seems to affect mechanical properties. Wu et al. investigated the effect of minor Zr/V additions in an Al-Si-Mg extruded alloy on texture and mechanical properties [99]. He concluded that the development of Brass texture component is helpful for yield strength.

5.9.3 Effect of extrusion profile on mechanical properties

The yield strength was reported higher for the bar and the tow nut, then the flat bar followed and the hollow rectangle had the lowest yield strength. The ultimate tensile strength followed the same trend. The mean GND density was very similar between hollow rectangle (32.37 $x10^{12}m^{-2}$) and flat bar (36.31$x10^{12}m^{-2}$). As the ER decreased to bar's 20, the mean GND density increased to 48.83 $x10^{12}m^{-2}$ and a further big increase was noticed for the tow nut, reaching 75.08 $x10^{12}m^{-2}$. These results confirm that the decrease of ER results to severe pile-up of dislocations that enhances strength.

5.10 Conclusions

- Morphologically the four profiles showed some differences. The effect of extrusion exit temperature was once again noticed. For the profiles with low ER the exit temperature was higher resulting to higher average grain size. Moreover, since the contact surface between the billet and the container is less for smaller ER, less shear stress and work hardening will occur. The two profiles with high ER (flat bar and hollow rectangle) had overall thinner grains, with some of them having serrated boundaries and other being pinched-off. This indicates high geometric dynamic recrystallization.
- During the through thickness investigation of the four profiles the grain size was reported thicker for the centre and gradually became thinner closer to the edge. This is evidential of the existence of two different mechanisms, higher recovery at the centre and higher shearing closer to the edge of the profiles.
- The extrusion geometry was found to be instrumental on the developed texture. The four extruded profiles showed different texture and they were further grouped into high and low ER, based on their texture. The profiles displayed the typical texture for their geometry, with hollow rectangle been treated as flat bar. The two profiles with high ER (flat bar and hollow rectangle) had Brass-S-Cube fibre texture, bar had Copper-Brass-Cube fibre and tow nut had similar texture with bar but with some differences at specific areas. The comparison between EBSD and XRD texture analysis showed that the results were in general in good agreement.

- Both EBSD and XRD texture analysis agreed that for the middle of tow nut Copper was the predominant texture component. Moreover, a significant volume fraction of P component was found through EBSD analysis. P belongs to recrystallization components and it is easy to deform due to the {111} slipping planes.

Chapter 6 The effect of extrusion ratio

6.1 Introduction

Most studies in the past only looked at the effect of ER regardless geometry. But extrusion geometry plays a tremendous role on the final microstructure, grain orientation and mechanical properties. There is a gap in the understanding of individual extrusion effect on final product and their interaction.

In order to decouple the effects of the extrusion geometry and the extrusion ratio, the addition of two new extruded profiles was suggested. Both solid bars; one with smaller and one with bigger diameter than the previously extruded solid bar (Chapter 5). The addition of the new profiles lead to two new investigations, Fig 6.1. The first one is the investigation of same extruded geometry, with different dimensions (investigation between the three solid bars). The second investigation is between extruded profiles with similar extrusion ratios but different geometries (comparison of flat bar-small solid bar and tow nut-big solid bar). The extrusion details of the five profiles, as well as their ER is presented in Table 6.1.

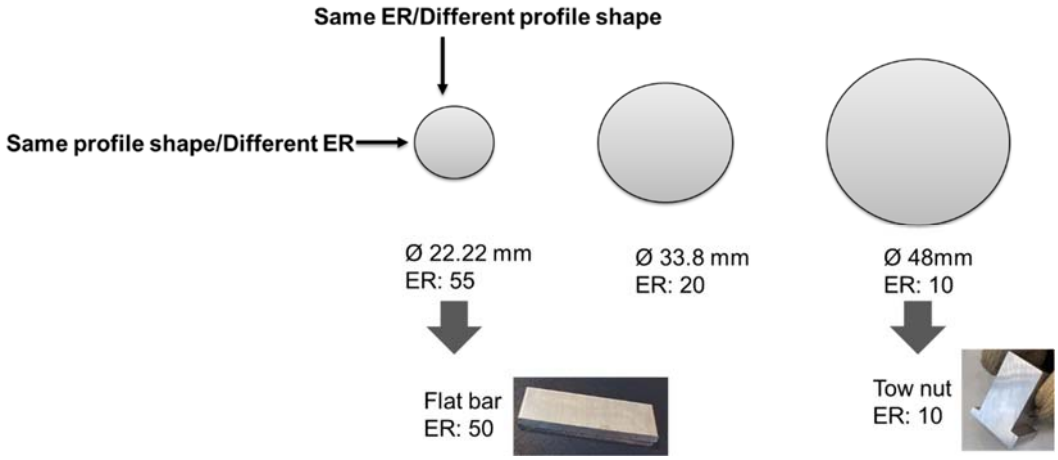

Fig 6.1 Schematic of the two new investigations with the profiles and their ER.

Table 6.1 Extrusion parameters and ER for the three round bars, flat bar and tow nut.

Profile	Extrusion Ratio (ER)	Extrusion exit speed (m/min)	Exit T (ºC)
Small round bar	55	9.3	548
Flat bar	50	9.6	540
Medium round bar	20	8.5	560
Big round bar	10	5.8	553
Tow nut	10	7	552

6.2 Microstructure

The IPF maps of the three bars, obtained at the ED-ND plane, at the centre of the half cross-section are presented in Fig 6.2. As expected, the grains of all the three solid bars were elongated through the extrusion direction; moving from the smaller to the bigger bar the thickness of the grains is getting significantly bigger. The average grain size, the high and low angle grain boundaries of the three bars are presented in Table 6.2. The average grain size for the small bar was 10.6 μm, then increased by 61.3% for medium bar, reaching 17.1 μm and decreased by 8.1% for large round bar, reaching 15.7 μm. Moreover, at the IPF map of the large round bar, a cluster of recrystallized grains can be observed.

The total amount of grain boundaries decreased from 0.49 for small round bar to 0.39 for medium round bar and then increased to 0.60 for large round bar. The HAGB of the medium bar is lower than the other two profiles by ~32%. The LAGB were similar for small and medium bar, but had a major increase, 68.5%, from medium to large round bar. The ratio of LAGB to HAGB amount increased from 0.44 for small round bar to 0.76 for large round bar.

The clustered area of large round bar with the equiaxed grains was found to contain mostly LAGB. In general, from Fig 6.3, most of the LAGB are located at grains within the <100> direction.

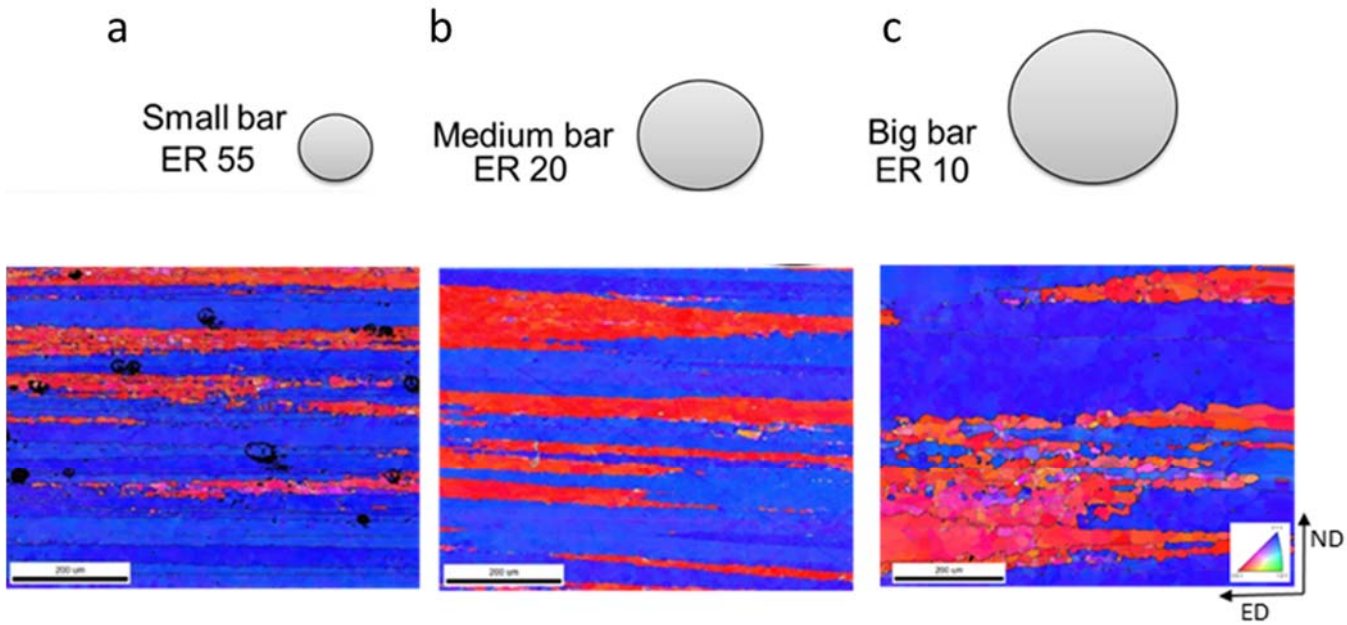

Fig 6.2 IPF maps of a) small, b) medium and c) large round bar and their extrusion ratios.

Table 6.2 Average grain size (and standard deviation), high (15º-65º) and low (5º-15º) low angle grain boundaries, total amount of grain boundaries and the ratio of low to high angle grain boundaries for small, medium, and large round bar.

Sample	Av. Grain size (μm)	HAGB (fraction)	LAGB (fraction)	Total GB (fraction)	LAGB/HAGB
Small bar	10.6 (0.013)	0.34	0.15	0.49	0.44
Medium Bar	17.1 (0.009)	0.23	0.16	0.39	0.69
Large bar	15.7 (0.011)	0.34	0.26	0.60	0.76

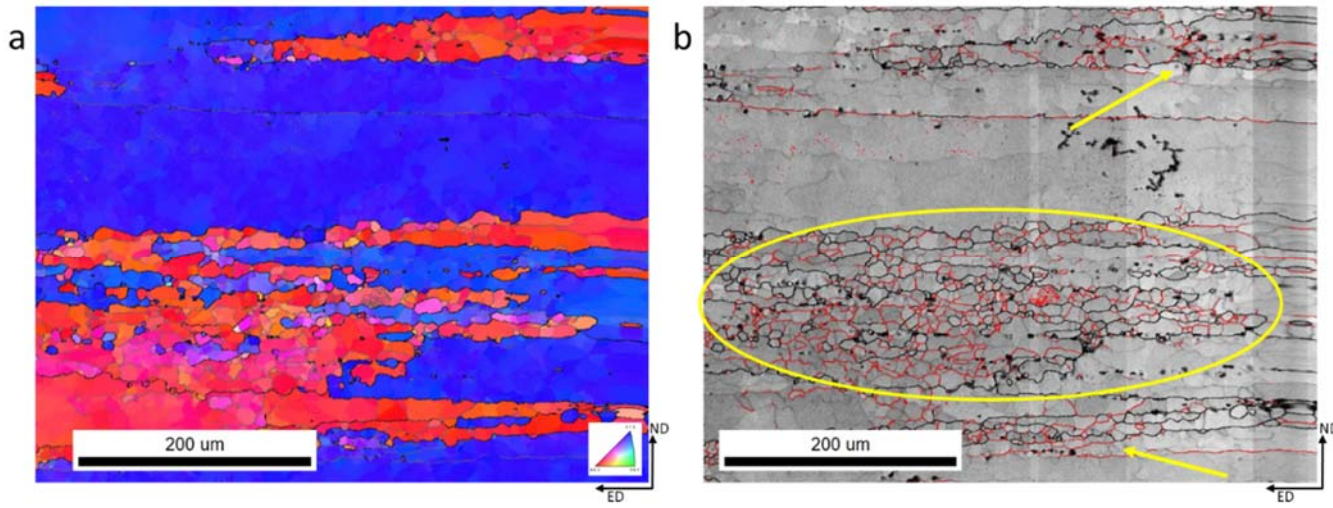

Fig 6.3 Image quality (IQ) map (b) of large bar in comparison with its IPF map (a). HAGB are presented with black and LAGB with red lines. Areas with increased presence of LAGB are noticed with yellow circle and arrows.

6.3 Texture

As it can be observed from the IPF maps the bars are strongly oriented. In all the cases there is strong texture with <111> and <100> fibers. The texture is extruded with Cu-Brass-Cube main components in all the three cases, with small differences at the intensities. Specifically, intensity increased from the small to large round bar; it was reported 14.8 for small bar, 16.3 for medium and 21.1 for large bar. The ODF maps (0º, 45º, 65º) of the three bars is presented in Fig 6.4.

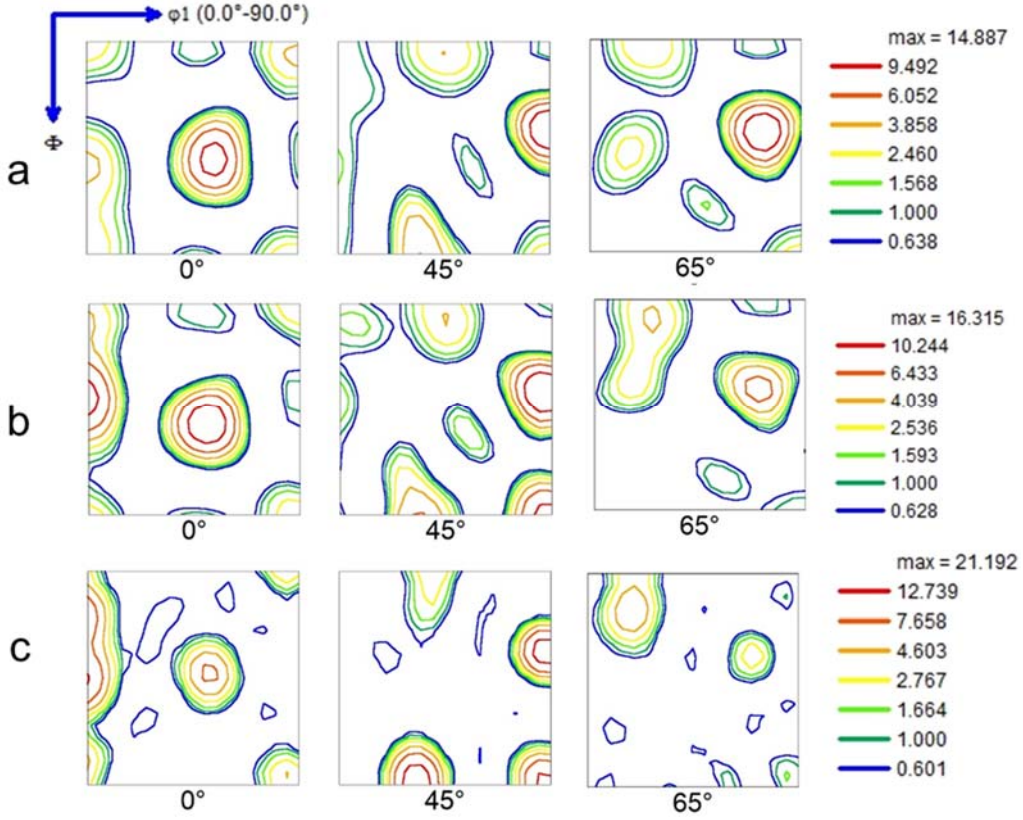

Fig 6.4 ODF sections (φ2 = 0°, 45° and 65°) of a) small, b) medium and c) large round bar of the previous presented microstructures.

Furthermore, the volume fractions of each texture component were calculated and are presented in Table 6.3. Copper is the predominant texture component for all the three cases, but it is especially high for the small bar, reaching 47 volume fraction. As the ER decreases Copper decreases as well. Specifically, from small to medium bar there is a 32.5% decrease and a further 21.1% from medium to big. The amount of Brass (rotated at 55º) is similar for the three bars, ~23. Finally, the Cube fibre is getting higher moving

from the small to the large round bar, with the volume fractions being 18.8 for the small, 29.7 for medium and 35.7 for large round bar. The increase of the volume of Cube fibre from small to large round bar is 89.8%. Moreover, the total volume fraction of the <111> and <100> fibres for each bar is presented in Fig 6.5.

Table 6.3 Volume fraction of the main texture components of small, medium and large round bar.

Sample	Brass {110}<112>	Copper {112}<111>	S {123}<634>	Cube {001}<100>	Goss {011}<100>	CG26.5 {021}<100>	Total Cube fibre (Cube-Goss-CG26.5)
Small bar	(R20º)23	47	0.6	7	5.7	6.1	18.8
Medium bar	(R20º)23.3	31.7	5.9	5.8	13.7	10.2	29.7
Large bar	(R20º)22	25	1.1	7	13	15.7	35.7

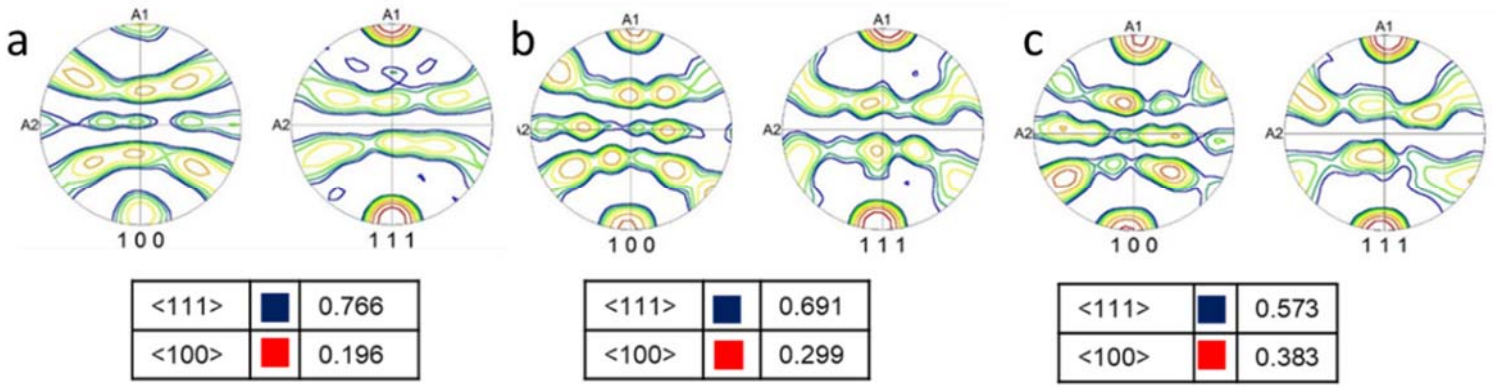

Fig 6.5 Pole figures (PF) and volume fractions of each fiber for a) small, b) medium and c) large round bar.

6.4 Mechanical properties

The yield strength is very similar for the three bars, with the medium bar reaching the highest strength, 408.1 ± 3.4 MPa. Small bar reported 403.7 ± 2.5 MPa and large bar 401.2 ± 2 MPa, as shown in Table 6.4. The ultimate tensile strength and uniform elongation are also very comparable for the three bars.

Table 6.4 Tensile properties of the three extruded round bars in T6 condition.

Sample	YS (MPa)	UTS (MPa)	EL (%)	n-value
Small bar	403.7 ± 2.5	443 ± 1.89	8.82 ± 0.52	0.071
Medium bar	408.1 ± 3.4	448.5 ± 2.24	8.61 ± 0.93	0.062
Large bar	401.2 ± 2	447.6 ± 2.28	9.01 ± 0.93	0.064

6.5 Effect of extrusion geometry on grain structure

After the study of the ER on the same extruded shape of different sizes the next investigation was the comparison of different extruded profiles with similar ER. For this, the flat bar and the tow nut from Chapter 5 were compared with the small and the large round bar respectively.

6.5.1 Microstructure

Both the small bar, with 55 ER, and the flat bar, with 50 ER, had long, elongated grains through the extrusion direction. For the flat bar many grain boundaries were serrated and new small grains were created by pinch-off. For the small bar only few, distinct areas of recrystallized or pinched-off grains could be observed. The extrusion ratio of

both the large round bar and the tow nut was 10. Microstructurally, their IPF maps looked similar with thick, elongated grains through the extrusion direction, with exception some clusters of equiaxed grains in both profiles, Fig 6.6.

The average grain size of the small bar was almost the double of the flat bar's; 10.6 μm and 5.5 μm respectively. Moreover, the high and low angle grain boundaries of the flat bar were ~ 30% higher that the small bar's. The average grain size was similar for the large round bar and the tow nut, with large bar's being 5% increased, 15.7 μm, than tow nut's, 14.9 μm. The fraction of the HAGB was higher by 23.5% for the tow nut, while the LAGB of the large bar were 62.5% increased from the ones of tow nut, Table 6.5.

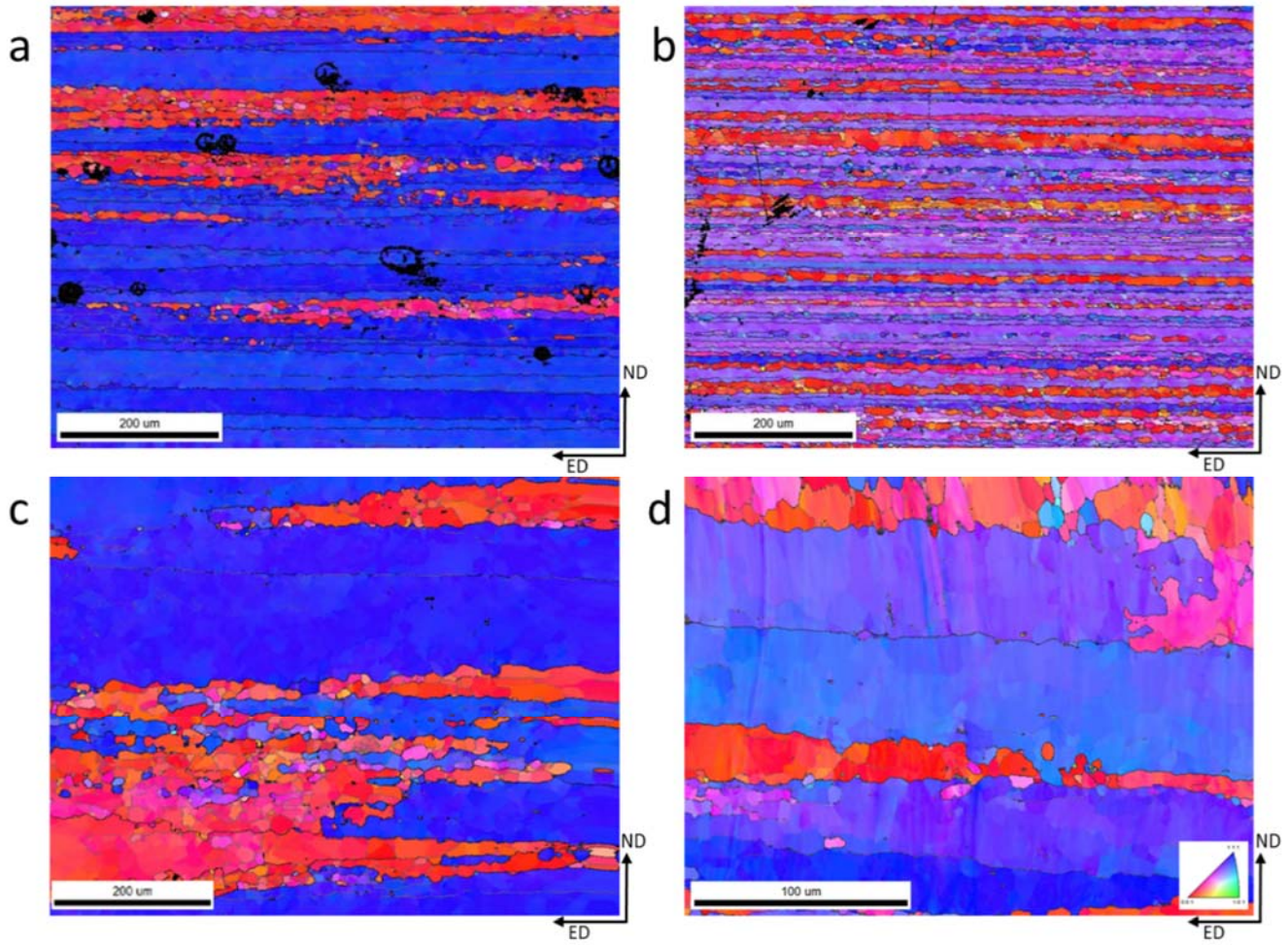

Fig 6.6 IPF maps of a) small round bar, b) flat bar, c) large round bar and d) tow nut.

Table 6.5 Average grain size (and standard deviation), high (15º-65º) and low (5º-15º) angle grain boundaries, total amount of grain boundaries and the ratio of low to high angle grain boundaries for small round bar, flat bar, large round bar and tow nut.

Sample	Av. Grain size (μm)	HAGB (fraction)	LAGB (fraction)	Total GB (fraction)	LAGB/HAGB
Small bar	10.6 (0.013)	0.34	0.15	0.49	0.44
Flat bar	5.5 (0.015)	0.44	0.20	0.64	0.45
Large bar	15.7 (0.007)	0.34	0.26	0.60	0.76
Tow nut	14.9 (0.025)	0.42	0.16	0.58	0.38

6.5.2 Texture

Comparing the texture of small round bar with the flat bar we can notice important differences, as shown in Fig 6.7 (a-b). In detail, as presented earlier, small bar had an extruded texture with Cu-Brass-Cube components, while flat bar had rolling texture with Brass-S-Cube. On the other hand, large round bar and tow nut had similar extruded texture with Cu-Brass and some Cube components, although tow nut showed a change of texture at the middle of its cross-section. The texture components of each profile can be found on their ODF, Fig 6.7(c-d) and their volume fraction in Table 6.6.

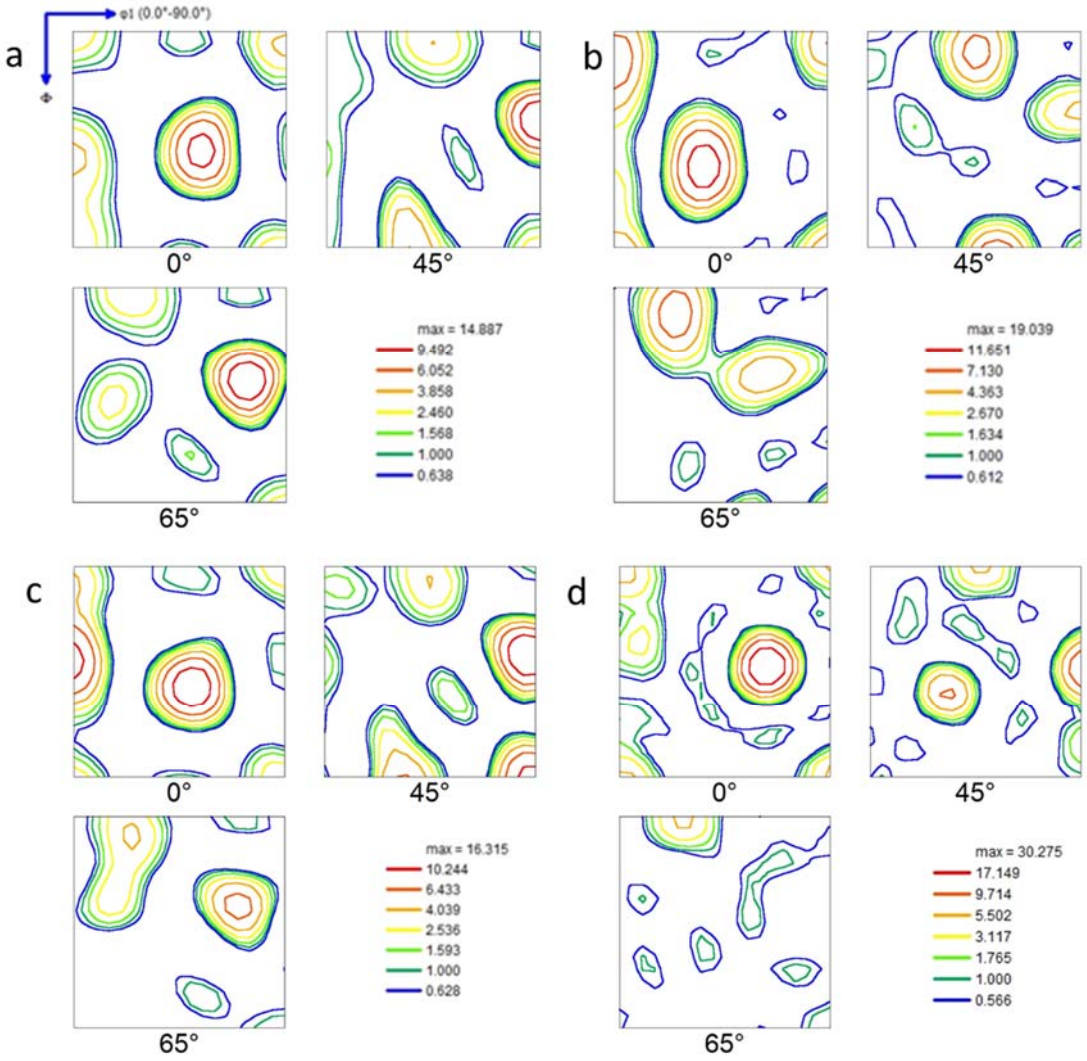

Fig 6.7 ODF sections (φ2 = 0°, 45° and 65°) of a) small round bar, b) flat bar, c) large round bar and d) tow nut.

Table 6.6 Volume fraction of the main texture components of small round, flat, large round bar and tow nut.

Sample	Brass {110}<112>	Copper {112}<111>	S {123}<634>	Cube {001}<100>	Goss {011}<100>	CG26.5 {021}<100>	Total Cube fibre (Cube-Goss-CG26.5)
Small bar	23	47	0.6	7	5.7	6.1	18.8
Flat bar	20.8	8.7	41.5	11.6	0.7	10.3	22.6
Large bar	22	25	1.1	7	13	15.7	35.7
Tow nut	R(20º)37.1	12.7	2.1	12.2	11.9	11.5	1.6

6.5.3 Effect of geometry on mechanical properties of extruded samples

For a given ER of 10, the yield strength remained similar between large round bar (401.2 MPa) and tow nut (400.1 MPa), as shown in Table 6.7. However, for ER between 50 and 55, the yield strength of extruded sample increased from 362.6 MPa for flat bar to 403.7 MPa for small round bar. The ultimate tensile strength followed the same trend, with those of large round bar and tow nut being similar (447.6 and 446.2 MPa), while for small bar and flat bar a important difference was reported, 443 and 413.4 MPa respectively.

Table 6.7 Tensile properties and extrusion ratios of the extruded profiles in T6 condition.

Sample	ER	YS (MPa)	UTS (MPa)	EL (%)	n-value
Small bar	55	403.7 ± 2.5	443 ± 1.89	8.82 ± 0.52	0.071
Flat bar	50	362.6 ± 0.58	413.4 ± 0.49	10.37 ± 0.42	0.14
Large bar	10	401.2 ± 2	447.6 ± 2.28	9.01 ± 0.93	0.064
Tow nut	10	400.1 ± 8.4	446.2 ± 4.1	8.37 ± 0.08	0.089

6.6 Discussion

6.6.1 The effect of extrusion ration on the same geometry

From the ER investigation, between the three bars with ER= 55, 20 and 10 a change of microstructure was noticed. The average grain size was higher for the medium bar, 17.1 μm, which also reported the highest extrusion exit temperature, 560ºC. Temperature is one of the main factors affecting the shape and size of grains. Since the quenching was optimized for every profile, the higher exit temperature resulted to coarser grains. Moreover, for the large round bar, clusters of recrystallized grains, containing LAGB was observed, resulting to a decrease of the average grain size.

The effect of ER on extruded rods has been investigated. Increase of ER has been reported to decrease average grain size at the centre of extruded rods which comes in agreement with the results of this investigation [70].

All the three bars exhibited strong <111> and <100> fibre texture. For axisymmetrically extruded aluminium alloys this is a typical texture [99]. The texture intensity decreased as the ER increased. The main texture components observed were Copper, Brass and Cube fibre (Cube-Goss-CG26.5). The predominant component was Copper for the three bars, with the volume fraction increasing significantly as the ER increased. Specifically, an 88% increase from big to small bar was reported. Brass component was not affected by the ER, keeping a similar average volume fraction ~23. Moreover, the total Cube fibre volume fraction decreased with the increase of ER. Overall, increasing ER resulted to increase of <111> and decrease of <100>. The transformation of the <111> texture to <100>// ED has been reported in the literature due to recrystallization [100].

There has been a big conversation in the literature regarding the source of Cube texture in deformed high stacking fault energy metals (Al and Cu). Scientists are debating the relationship between the major rolling texture components, Copper and S, and recrystallization Cube texture. S component has a ~40º <111> orientation relationship with Cube component and following the orientation growth theory it should be the component accountable for Cube presence. Nonetheless, from the experimental data Copper seems to be the texture component responsible for Cube [100-104]. From the

trend appeared in this investigation we can conclude that Copper is responsible for Cube and support the literature.

The strength results support the previous observations, that there is an optimum combination of texture components and grain characteristics. The yield strength of the three bars was very close to each other, but the best results were observed for the medium bar with 408 ± 3.4 MPa. The medium bar had a good combination of high amount of strong <111> fiber and low amount of weak <100> fiber, while the average grain size was 17.1 μm. The small round bar, with 403.7 ± 2.5 MPa, had a slightly better combination of <111> and <100> fibers but the average grain size was 10.6 μm. Finally, the large round bar that had the lowest strength, 401 ± 8.4 MPa, showed a high amount of <100> fiber, mainly attributed to the recrystallization area and probably the big grain size contributed to the lower strength. It has been reported that increase of ER resulted to increase of ultimate tensile strength and hardness [72]. In this present study an increase of ER from 10 to 20 resulted to a 7 MPa increase of yield strength, but the further ER increase to 55 followed by a 4.5 MPa decrease.

Moreover, it has been reported that among different extrusion parameters (extrusion ratio, billet and container temperature and ram speed) extrusion ratio has the biggest effect on surface cracks initiations. Specifically, increase of ER resulted to less surface cracks [89].

6.6.2 The effect of geometry on similar ER

Although small bar and flat bar had similar ER, 55 and 50 respectively, significant differences were observed at their morphology and texture. The small bar's average grain size was double the flat bar's, with some clusters of recrystallized grains. On the other hand, flat bar had 40% more LAGB, with many thin, elongated, serrated grains and others, equiaxed, that had been pinched-off. This indicates that geometric dynamic recrystallization was higher for the flat bar.

Moreover, the texture was different for the two profiles. A rolling texture of Brass-S-Cube components were found in flat bar and extrusion texture of Cu-Brass-Cube components were found in small round bar. The amount of Brass component remained similar for both small round bar (23%) and flat bar (20.8%), while S component increased from the small round bar (0.6%) to flat bar (41.6%) at the expense of Copper component, which decreased from 47% for small round bar to 8.7% for the flat bar. The

total amount of cube fibre (Cube-Goss-CG26.5) increased from 18.8% for small round bar to 22.6% for flat bar, due to the high amount of pinched off grains.

For ER of 10, a common extrusion texture of Cu-Brass and some Cube components was found in both large round bar and tow nut profiles. The tow nut had a higher amount of Brass and Copper than those found in big round bar but both had very little amount of S component. However, the total amount of cube fibre (Cube-Goss-CG26.5) decreased from 35.7% for big round bar to 14.4% for tow nut. This comes in agreement with the higher amount of LAGB for the large round bar and the presence of recrystallized areas.

For a given ER of 10, the yield strength remained similar between large round bar (401.2 MPa) and tow nut (400.1MPa), indicating that Cu-Brass-Cube texture results to high mechanical properties materials. Moreover, the differences of the amount of the texture components did not seems to affect strength. However, for ER between 50 and 55, the yield strength of extruded sample increased from 362.6 MPa for flat bar to 403.7 MPa for small round bar. This comes in agreement with the microstructural and textural differences between the two profiles.

The effect of different extruded shapes was investigated by Qamar et al. They studied a round, C-shape, cross, rectangle, square, triangle, I-shape, T-shape, and L-shape profiles and concluded that metal flow inhomogeneity and extrusion pressure increase with higher shape complexity. In addition, the importance of ER and geometrical symmetry was pointed. It was suggested that complexity should include ER. Moreover, dead metal zone was found to be affected by ER and symmetry [105].

6.7 Conclusions

- The average grain size as a function of ER for a given round profile, increased from high ER of 55 to similar size for both medium ER of 20 and low ER of 10 due to different strains and temperature effects.
- All the three round bars exhibited strong <111> and <100> fibre texture.
- For the three round bars, Copper was the predominant texture component, with its amount increasing significantly as the ER increased. At the same time, the amount of <111> increased at the expense of Cube <100> fibre texture with increasing ER.
- For all round bar, the brass component seemed independent of ER, Copper component decreased with increasing ER and total cube fibre increased with increasing ER. Cube fibre will be higher at higher ER due to microstructural changes and recrystallization resulting from higher strains.
- Similar ER can result to completely different microstructure and texture. Between small round bar and flat bar, the average grain size decreased significantly. Moreover, a rolling texture of Brass-S-Cube was found in flat bar and extrusion texture of Cu-Brass-Cube was found in small round bar. The different texture explains the 41MPa difference.
- Large round bar and tow nut, with ER of 10, exhibited similar microstructure and texture, that were reflected to similar strength.

Chapter 7 Case study of a complex extruded profile

7.1 Introduction

So far, the investigations have been focused on simple geometries, such as hollow rectangle, flat bar, round bar and tow nut. However, in automotive industry more complex profiles need to be extruded. These complex geometries aim to provide lightweight and strong parts of the final vehicles.

There are different approaches to define the extrusion complexity in the literature. Most commonly the shapes are grouped according to the geometry similarity from simple to more complex shapes. The easiest way of grouping extrusion profiles is by dividing them into solids, semi-hollows and hollows, with increasing level of complexity from solids to hollows [106]. Another way of separating the profiles is based on a quantitative approach, since the extrusion pressure increases with increasing complexity of the profile [105]. Finally, a third way is based on the effect the profiles have on tool failure [107]. The geometrical symmetry of the extrusion profile is an important factor for complexity. Bars, rectangles and I-shapes have a biaxial symmetry, while T or C-shapes have only one axis of symmetry and many other industrial profiles have none.

After the initial investigations of the different extrusion geometries (eg. the different size of the same geometry and the extrusion ratio), a complex profile was suggested for investigation. This profile is a commercial car side beam and it is a combination of a hollow rectangle with fins (flat bars) at the bottom side. The reason of investigating the specific profile was, except the fact that it is a combination of two profiles that have already been included in the previous studies, the inconsistency of mechanical properties at different sides that had been reported in the past. Specifically, a difference of ~25 MPa of strength had been reported between the stronger core (hollow rectangle) and the weaker fins. It was suggested that the use of texture analysis could help to explain the observed difference in strength at different sides of this complex profile.

7.2 Extruded microstructure of complex geometrical profile

Fig 7.1 (a-d) show typical IPF maps, at the centre of the cross section, taken from four sides of the complex profile (top, bottom, right-hand side (RF) and left-hand side (LF) fin). From the colour coding and the grain morphology it can be observed that the four sides can be grouped at top-bottom and right-left fin.

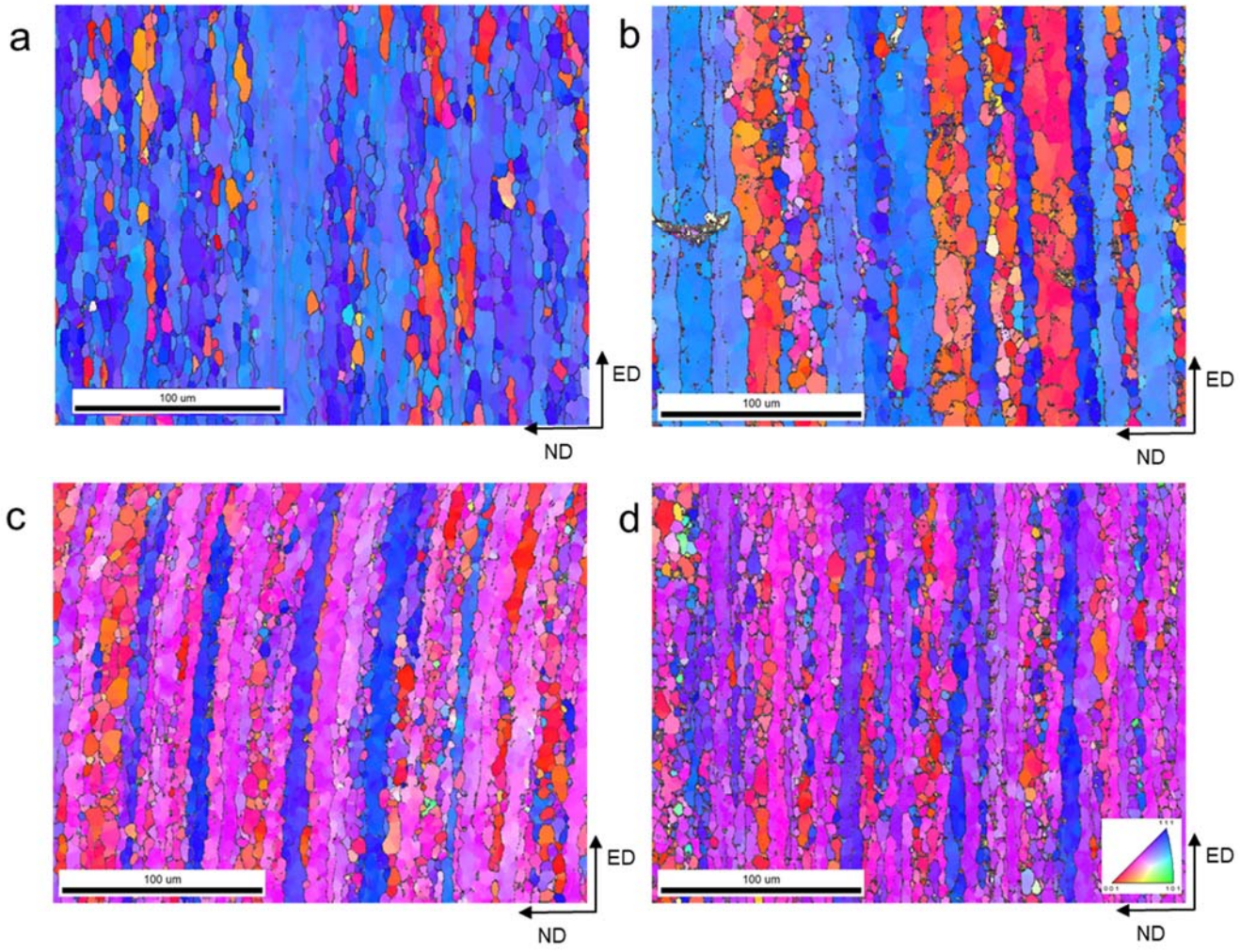

Fig 7.1 Typical IPF maps of the a) top, b) bottom, c) right hand side and d) left hand side fins.

Table 7.1 Average grain size (and standard deviation), high (15º-65º) and low (5º-15º) grain boundaries, total amount of grain boundaries and the ratio of low to high angle grain boundaries of the top, bottom, bottom, right-hand side and left-hand side fin.

Side	Av.Grain size (μm) (dev)	HAGB (fraction)	LAGB (fraction)	Total GB (fraction)	LAGB/HAGB
Top	4.04 (0.053)	0.36	0.16	0.52	0.44
Bottom	3.97 (0.041)	0.69	0.06	0.75	0.08
Right fin	3.63 (0.023)	0.66	0.12	0.78	0.18
Left fin	3.83 (0.022)	0.61	0.14	0.75	0.22

The average grain size measured from various sides of the complex profile was found to be similar, with the lowest of 3.63 μm at the right-hand side fin and the highest of 4.04 μm at the top side, as shown in Table 7.1. However, the total amount of grain boundaries (HAGB + LAGB) was found to be lowest (0.52) for top side, while those for the other three areas were found to be similar in the range between 0.75 and 0.78, as shown in Table 7.1. The ratio of LAGB/HGAB was found to be 0.44 for the top side, 0.08 for the bottom side, 0.18 for the left-hand side and 0.22 for the right-hand side fin.

7.3 Development of grain structure through thickness of the complex geometrical profile studied by multiple EBSD scans

Fig 7.2 (a-d) show through thickness IPF maps of various sides of the complex profile taken by multiple EBSD scans. The right-hand side and left-hand side fins contained a thick PCG layer, ranging from 400 to 450 μm, at both ends, as shown in Fig 7.2 (a-b), respectively. These results come in agreement with similar flat profiles, such as the hollow rectangle and the flat bar previously presented (Chapter 5). However, the top and bottom sides contained a very thin PCG layer, ranging from 15 to 25 μm, at both sides, as shown in Fig 7.2 (c-d), respectively.

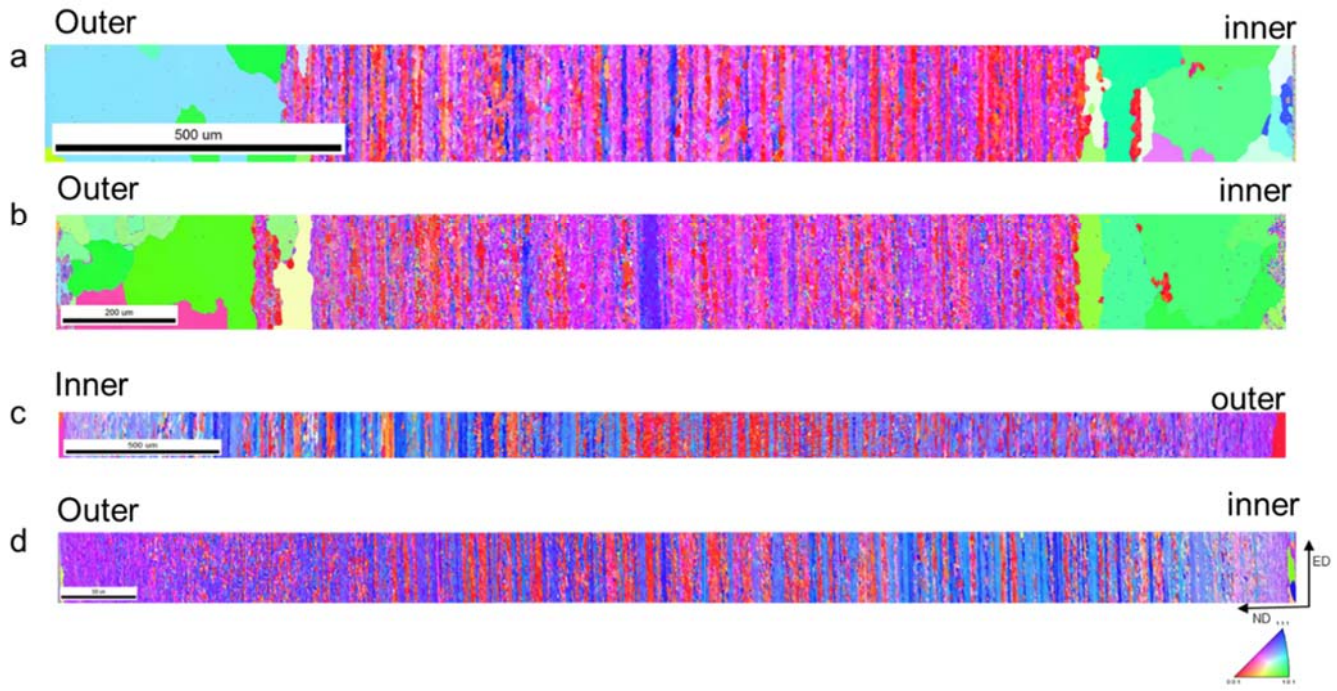

Fig 7.2 IPF maps of the whole cross section for a) right-hand side, b) left-hand side fin, c) top and d) bottom side.

Table 7.2 Average grain size and standard deviation in parenthesis (μm) from edge to centre.

Side	Edge	Intermediate	Centre	Grain size increment (%) (edge to centre)
Top	5.54 (0.013)	6.64 (0.007)	6.08 (0.008)	9.7
Bottom	4.33 (0.001)	6.12 (0.013)	5.41 (0.011)	24.9
Right fin	4.03 (0.019)	4.31 (0.013)	4.75 (0.015)	17.8
Left fin	3.043 (0.025)	3.14 (0.029)	3.92 (0.042)	28.8

Due to symmetry half of each four areas was investigated. The half cross-sections were split into three equal areas. For the left-hand side and right-hand side fins, the PCG layer was avoided. Table 7.2 gives a list of average grain size of the various sides of this complex profile from edge, to intermediate, to centre along a given axis. The measured average grain size increased from the edge (5.54 μm for top side and 4.33 μm for the bottom side) to the intermediate position (6.64 μm for the top side and 6.12 μm for the bottom side) and then decreased towards to the centre (6.08 μm for the top side and 5.41 μm for the bottom side). However, for the right-hand side and left-hand side fins, the measured average grain size increased from the edge (4.03 μm, 3.04 μm) to the centre (4.75 μm, 3.92 μm), respectively.

7.4 Texture of complex geometrical profile

The EBSD texture analysis was performed at the centre of each side taken from the same areas as IPF maps in Fig 7.2. The texture of the four sides, in the form of ODF maps was investigated and is presented in Fig 7.3.

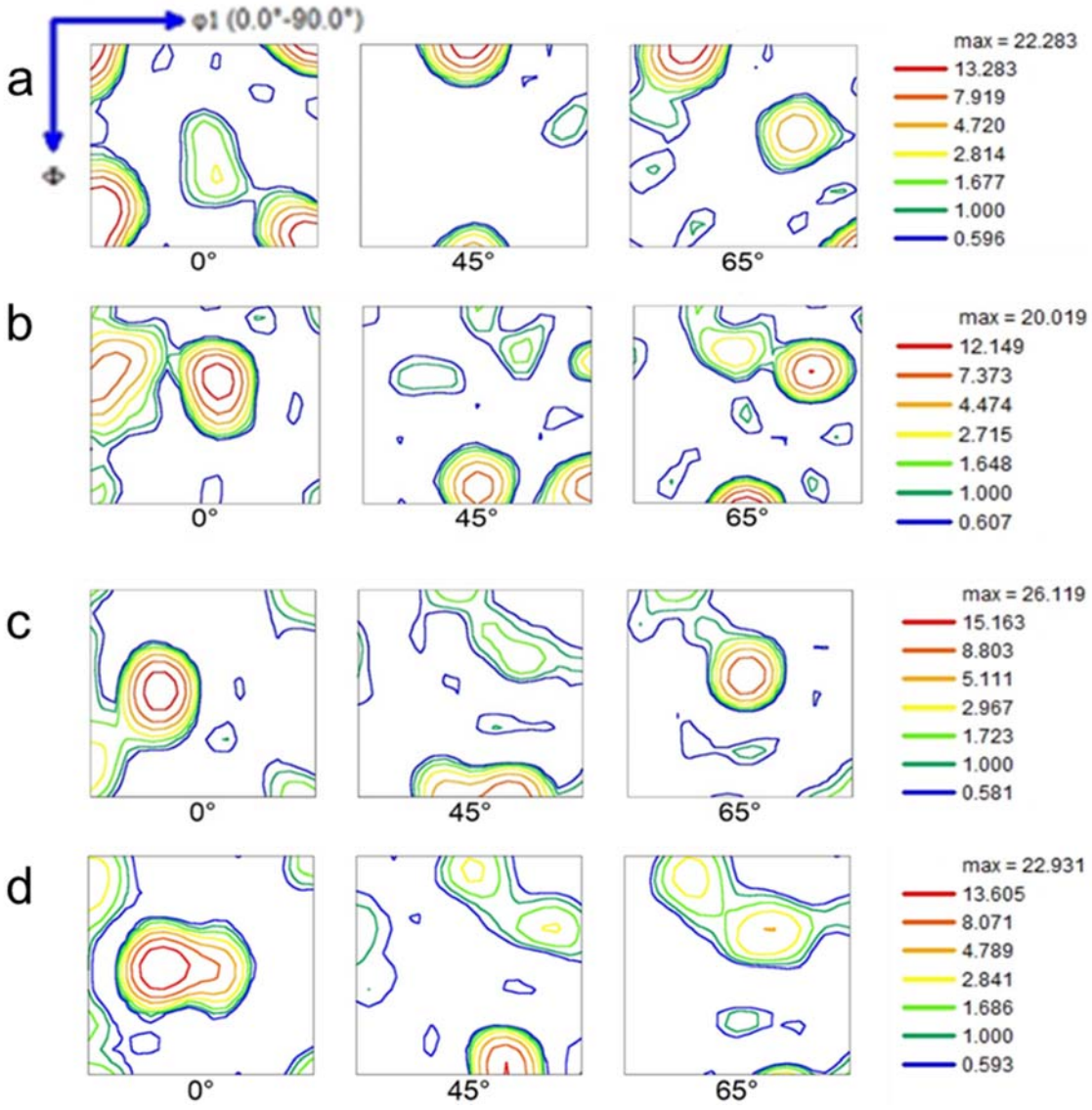

Fig 7.3 ODF sections (φ2 = 0°, 45° and 65°) of a) top, b) bottom side, c) right-hand side and d) left-hand side fin.

Fig 7.3 (a-d) shows typical ODF sections of top, bottom, right-hand side and left-hand side fin of the complex extrusion profile, while Table 7.3 gives the volume fractions of texture components determined by the texture analysis. It was found that both top and bottom exhibited a mixture of texture comprising of deformation (Cu-Brass-S) and recrystallisation (Cubic-CG26.5-Goss). The Brass component was rotated by 10º in both cases. The total amount of Cube fibre (Cube-CG26.5-Goss) was high in top (50.5%) and bottom (32.6%) sides, as compared to right-hand side fin (8.8%) and left-hand side fin (7.8%). In all the cases, the extruded material was found to be highly textured. The right-hand side and left-hand side fins exhibited a strong Brass-S texture. Both Bass and S components for right-hand side (43.9%,19.4%) and left-hand side (41.9%, 30.3%) were found to be higher than the other two sides, while Copper component was found to be higher for both top (8.8%) and bottom (6.9%) sides than the other two sides.

An amount of Q {013}<231> texture component was found in both top (3.3%) and bottom (9.5%) sides, whereas, CT texture component was found in top (3.7%), right-hand side (2.2%) and left-hand side (1.2%) fins.

Table 7.3 Volume fraction of the main texture components of the four sides through the EBSD analysis.

Sample	Brass {110}<112>	Copper {112}<111>	S {123}<634>	Cube {001}<100>	Goss {011}<100>	CG26.5 {021}<100>	Q {013}<231>	CT18DN {001}<3-10>	Total Cube fibre (Cube-Goss-CG26.5)
Top	R(10°)12.7	8.8	9.9	27.9	1.1	21.5	3.3	3.7	50.5
Bottom	R(10°)25.1	6.9	10	1.4	11.7	11.4	9.5	0.8	24.5
Right fin	43.9	5.1	19.4	3.1	1.4	4.3	0.9	2.2	8.8
Left fin	41.9	3.5	30.3	3	0.4	4.4	0.4	1.2	7.8

In Tables 7.4 and 7.5 the evolution of each texture component across the cross-sections is presented. It is interesting to notice that Brass component had a significant drop for all the four sides from edge to intermediate area. Specifically, a ~34.5% decrease was noticed for the fins, while for top and bottom Brass was eliminated at the intermediate and centre areas. At the same time, Copper and S component increased. For top and bottom Copper increased from the edge to the centre by 2.3 and 3.6 times respectively. As it can be seen, the evolution of texture components of the right-hand side and left-hand side fins showed great similarity. For the fins, S component increased in a similar way for both, from edge to intermediate area, by 25.5% for left and 29.5% for right hand side fin. From recrystallization components the development of Cube for the top side had the most important change. From a very small amount for the edge and intermediate areas (~4) it reached 44.9 volume fraction for the centre.

Table 7.4 Amount of the main deformation texture components (Brass, Copper, S) of the four sides found at the edge, intermediate and centre areas.

Sample	Texture component	Edge	Intermediate	Centre
Top	Brass {110}<112>	20.4	1.1	1
	Copper {112}<111>	5.1	20.2	10.9
	S {123}<634>	5.6	20.5	26.7
Bottom	Brass {110}<112>	13.2	0.6	2
	Copper {112}<111>	11.3	26.2	18.7
	S {123}<634>	26.3	13.3	11.3
Right fin	Brass {110}<112>	26	17.5	32.6
	Copper {112}<111>	6.5	8.4	6.2
	S {123}<634>	20	25.9	16.5
Left fin	Brass {110}<112>	25.7	17.1	34
	Copper {112}<111>	2.2	4.5	3.6
	S {123}<634>	25.4	31.9	23.9

Table 7.5 Amount of the main recrystallization texture components (Cube, Goss, CG265) of the four sides found at the edge, intermediate and centre areas.

Sample	Texture component	Edge	Intermediate	Centre
Top	Cube {001}<100>	3.2	3.1	44.9
	Goss {011}<100>	0.3	5.1	0.3
	CG26.5 {021}<100>	1.9	11.2	9.9
Bottom	Cube {001}<100>	2.9	4.9	6.1
	Goss {011}<100>	1.3	3.6	3
	CG26.5 {021}<100>	3.1	7.2	14.5
Right fin	Cube {001}<100>	7.1	6.6	3.9
	Goss {011}<100>	1.7	1.1	1.4
	CG26.5 {021}<100>	14.7	5.7	4.9
Left fin	Cube {001}<100>	5.6	9	2.4
	Goss {011}<100>	4.2	0.6	0.2
	CG26.5 {021}<100>	12.8	15.1	4.5

The evolution of the total amount of deformation (Brass, S, Copper) and recrystallization (Cube, Goss, GC) components for each side is presented in Fig 7.4. For the top and bottom sides, the deformation components decreased while the recrystallisation components increased from the edge to the centre positions. For the right-hand side and left-hand side fins, the deformation components remained stable with a small increase at the centre, while recrystallization ones decreased moving from the edge to the centre.

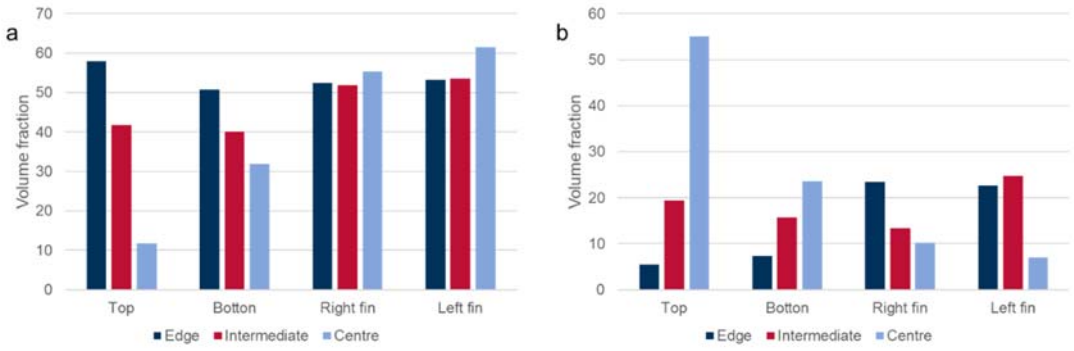

Fig 7.4 Total volume percent of a) deformation and b) recrystallization components.

7.5 X-ray Diffraction texture analysis

Further X-ray diffraction texture analysis was conducted to the four parts. In general, deformation texture was found to be predominant, with S, Brass and Copper being the main texture components, Fig 7.5. In deeper analysis, the top and bottom sides showed higher volume of Copper component, while right-hand side and left-hand side fins had higher amount of Brass. Moreover, presence of recrystallization texture (Cube-CG26.5-Goss) was found in top and bottom and weak presence of shear texture (J-H) in right and left-hand side fins.

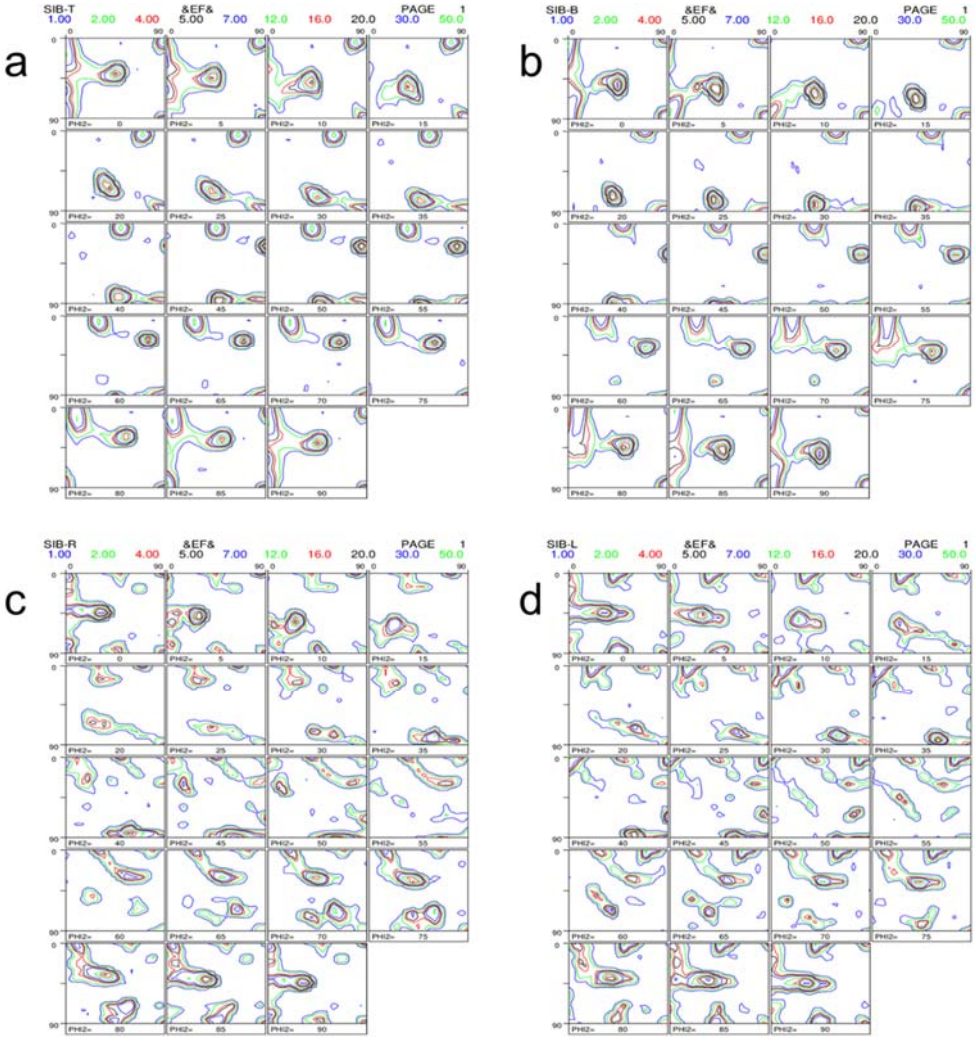

Fig 7.5 ODF maps obtained from XRD of a) top and b) bottom side, c) right and d) left hand side fin.

7.6 Mechanical properties of complex profile taken at various sides

The mechanical properties of the four sides of the complex profile taken from the intermediate position were measured on samples after a T6 heat treatment and are presented in Table 7.6. Both top (367 MPa) and bottom (384 MPa) sides exhibited higher yield strength than those of right-hand side (343 MPa) and left-hand side (340 MPa) fins.

Table 7.6 Yield strength of top, bottom, right and left fin, at T6 condition (12h, 170ºC).

Sample	YS (MPa)	UTS (MPa)	EL (%)	n-value
Top	367 ± 1.055	415.2 ± 0.47	10.47 ± 0.42	0.071
Bottom	383.8 ± 0.025	428.1 ± 2.53	9.85 ± 0.75	0.063
Right fin	343 ± 0.39	387. 2 ± 1.41	12.38 ± 0.96	0.12
Left fin	340.4 ± 1.6	388.1 ± 0.86	12.52 ± 0.53	0.14

7.7 Discussion

Morphologically, top and bottom were similar, as well as right and left-hand side fins. The average grain size was higher for the top and bottom, with 4.041 μm and 3.97 μm respectively. Right and left fins average grain size was 3.62 μm and 3.83 μm. Kayser et al. reported that for extuded EN AW-6060, increase of deformation resulted to decrease of average grain size as a result of dynamic recrystallization [108].

PCG layers observed at both edges of the fins, with their thickness being 400-450 μm. Their existence is attributed to the combination of high temperature, strain and strain rate, leading to concentration of dislocations. Similar PCG layers were observed for the hollow rectangle and flat bar of chapter 5. PCG is commonly found in the literature for extruded 6xxx Al alloys and this phenomenon should not be confused with static recrystallization [87,108,109]. For the top and the bottom sides PCG was much thinner (15-25 μm) indicating less plastic deformation at the surface of the extrudate.

The evolution of the average grain size followed different trends for top-bottom and the fins. For the top and the bottom, a band of thicker grains between the edge and the centre was reported. That was especially pronounced for the bottom, where the increase was 41.3% from edge to intermediate area. For the fins, the grains became thicker moving from the edge to the centre. The grains size evolution through the cross-section of the two fins followed the same trend as hollow rectangle and flat bar of chapter 5.

Texture analysis reviled the differences of texture between top-bottom and the fins. Overall, the texture was deformation Brass-S-Copper. For top and bottom an important volume fraction of Cube was also present. Moreover, the volume fraction of Copper component was significantly low for the fins through the whole cross-section, less than 8% at any area.

From the trough thickness analysis, it was noticed that for the top and bottom the overall compression components volume fraction decreased from edge to the centre and Cube fibre increased at the same time. Moreover, for the fins, the overall compression components volume fraction remained at similar levels through the thickness and the Cube fibre, with an exemption of the intermediate area of right fin, decreased from edge to the centre.

7.8 Conclusions

- The average grain size of top and bottom was slightly higher that the fins but bands of recrystallized grains were also present. Moreover, top side had high amount of LAGB.
- Top and bottom sides consisted of a mixture of deformation (Brass-S-Copper) and recrystallisation texture (Cube-Goss-GC), while the right- and left-hand side fins consisted of only deformation texture (Brass-S-Copper).
- The overall texture obtained from the XRD analysis was comparable to the EBSD texture. Moreover, the higher Cu and presence of recrystallization at the top and bottom as well as the high Brass at the fins were reported in both cases. The only deference noticed was a weak presence of shear texture (J-H) in the fins for XRD and a weak presence of recrystallization components Q and CH in top and bottom for EBSD. The localization and their small volume make these differences negligible.
- The yield strength results further pointed the grouping of the sides to top-bottom and right-left fin. The highest strength was reported for the bottom, with a refined β-fibre texture and presence of Cube fibre. Top, which followed at strength, had similar texture, but the Cube fibre had the double volume fraction from bottom. The fins, that showed ~40 MPa less yield strength that the bottom had predominant Brass and less Cu component.

Chapter 8 Effect of thermomechanical treatment

8.1 Introduction

This PhD project is also concerned with the investigation of the thermomechanical processing effect on resultant microstructure and properties of aluminium extrusion. This is a complex process involving different heat treatments and deformations. A range of microstructural features is affected, leading to changes in the final mechanical properties. These microstructural features include (sub)grain size and shape, crystallographic texture, recrystallization, and precipitates. However, the lack of understanding of the effect of shape/extrusion ratio and type of texture of the extrudate on the response of 6xxx alloy to the thermomechanical processing has constricted the achievement of potential performances of this material.

Two extrusion profiles of flat bar and medium round bar (reported in Chapter 5) were chosen for this investigation. They were chosen because these profiles showed difference in extrusion ratio, geometrical shape and crystallographic texture as reported previously in Chapter 5. In addition, these two profiles showed an important difference of yield strength at T6 condition, with the round bar having almost 50 MPa higher strength than the flat one, as report in Chapter 5.

Even though each extrudate might need a customized aDA recipe (pre-ageing, deformation, post-ageing) to achieve the best combination of properties, it was decided to use the same recipe for both profiles in this investigation. By this way, the variable of thermomechanical process will be constant. The chosen standard aDA process conditions consisted of: (a) an initial aging at low temperature, (b) followed by stretching and (c) a final post aging at high temperature. A schematic diagram of the full processing procedure of this alloy is presented in Fig 8.1.

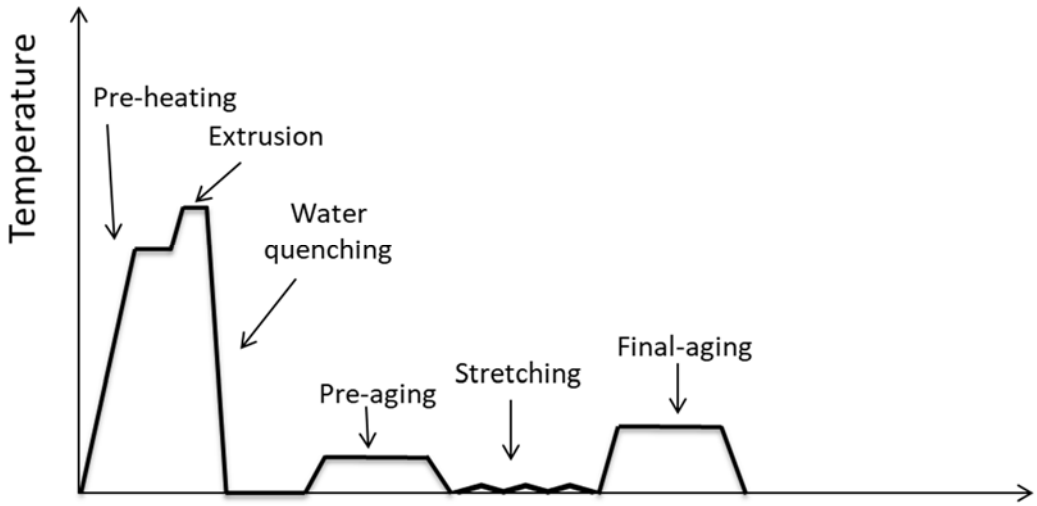

Fig 8.1 Schematic of the full processing of the alloy used for the thermomechanical treatment.

8.2 Microstructure of extrusion subjected to various stages of aDA thermomechanical treatment.

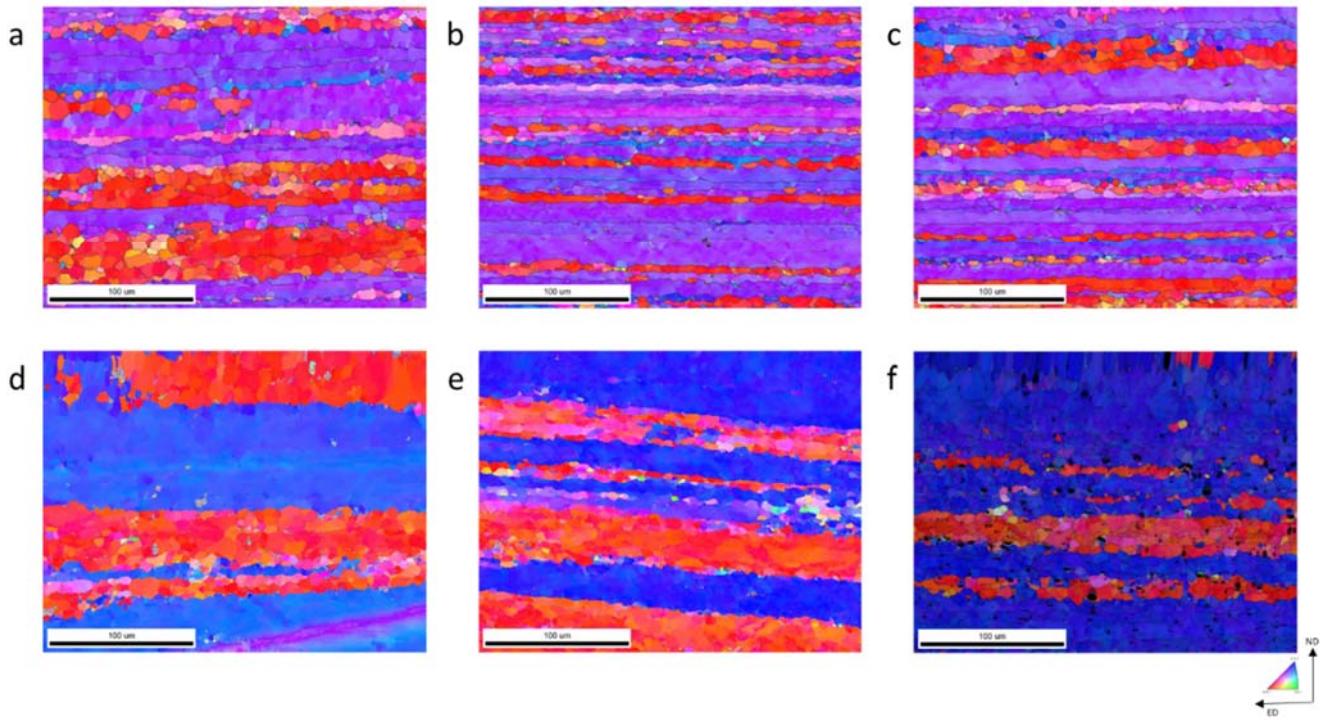

Fig 8.2 IPF maps of the: flat bar after a) pre-ageing, b) stretching and c) post-ageing, and medium round bar after d) pre-ageing, e) stretching and f) post-ageing.

Table 8.1 Average grain size (and standard deviation), high (15º-65º), low (5º-15º) angle grain boundaries, total amount of GB and LAGB/HAGB after each step of aDA for a) medium round bar and b) flat bar.

a

Medium round bar	Av. Grain size (μm)	HAGB (Fraction)	LAGB (Fraction)	Total GB (Fraction)	LAGB/HAGB
Pre-aged	9.59 (0.027)	0.41	0.21	0.62	0.51
Stretched	6.28 (0.025)	0.39	0.29	0.68	0.74
Post-aged	8.11 (0.029)	0.45	0.21	0.66	0.46

b

Flat bar	Av. Grain size (μm)	HAGB (Fraction)	LAGB (Fraction)	Total GB (Fraction)	LAGB/HAGB
Pre-aged	5.91 (0.020)	0.50	0.26	0.76	0.52
Stretched	4.78 (0.019)	0.51	0.27	0.78	0.53
Post-aged	5.03 (0.018)	0.57	0.21	0.78	0.37

Figs 8.2(a-f) show typical IPF maps of the flat bar and medium round bar. The grains look similar at every step of the aDA for both profiles. Table 8.1 gives a list of the average grain size with the amount of HAGB and LAGB of these two extrusion profiles subjected to different stage of the aDA process. For the flat bar, the average grain size decreased from 5.91 μm after pre-aging to 4.78 μm after stretching and then increased slightly to 5.03 μm after post-aging. The total amount of grain boundary (HAGB+LABG) was found to be similar for each step. However, the amount of HAGB and the ratio of the amount of LAGB to HAGB after pre-aging and stretching remained similar. The post-aging resulted in high amount (0.57) of HAGB with lower ratio of LAGB to HAGB (0.37).

For medium round bar, the average grain size decreased from 9.59 μm after pre-aging to 6.28 μm and then increased to 8.11 μm after pre-aging. Similarly, there was no significant difference in the total amount of grain boundary (HAGB+LAGB) between the various steps of aDA process. The amount of HAGB was found to be similar after pre-aging (0.41) and stretching (0.39) but increased slightly after post-aging (0.45), whereas the amount of LAGB was similar after pre-aging and post-aging (0.21) but, increased slightly after stretching (0.29). However, the ratio of amount of LAGB to HAGB increased from 0.51 after pre-aging to 0.74 after stretching and then decreased to 0.46 after post-aging. Moreover, a colour gradient in the grains was observed for both profiles, indicating there was remaining strain in the grains from the deformation, leading to ingrain misorientation.

8.3 Texture of extrusion subjected to various stages of aDA process

Figs 8.3 (a-f) show ODF sections of flat bar and medium round bar subjected to pre-aging, stretching and post-aging stages of aDA process. Table 8.2 gives a list of the amount of texture components extracted from ODF sections.

For the flat bar, the texture for each stage of aDA was Brass-S-Cube, with higher intensity after stretching (25.15), and after post-aging (22.05) steps. The Brass component increased from 17% after pre-aging to similar amount after stretching (32%) and post-aging (32%). The Copper component increased from 2.7% after pre-aging to 6.8% after stretching to 9.5% after post-aging. The S component after pre-aging (30%) and stretching (33%) remained similar but decreased after post-aging (21%). However, the total amount of Cube texture (Cube-Goss-CG26.5) decreased from 29.8% after pre-aging to 16.3% after stretching and then increased to 22% after post-aging, with Cube as the dominant component.

For the medium round bar, a very strong extruded texture was found at each stage of the aDA process with intensities at 38 after pre-aging, 30.5 after stretching and 43.3 times random after post-aging. In particular, the texture was Brass-Copper with a presence of Cube fibre, mostly Goss and CG26.5 components. The Brass component was highly rotated (at 55º) in each stage of aDA process as noticed in ODF sections (Fig.8.3). The amount of Brass (11%) component was the lowest after stretching, while the amount of Copper (7%) component was the lowest after pre-aging as compared to others. After pre-aging and post-aging, the Brass component was 29.9% and 25%, while the Copper component after stretching and post-aging was 29.6% and 32%, respectively. It is interesting to notice that the medium round bar contained a small amount of recrystallization P component after stretching and post-aging stages, with an amount of 3.1% and 7.5% respectively.

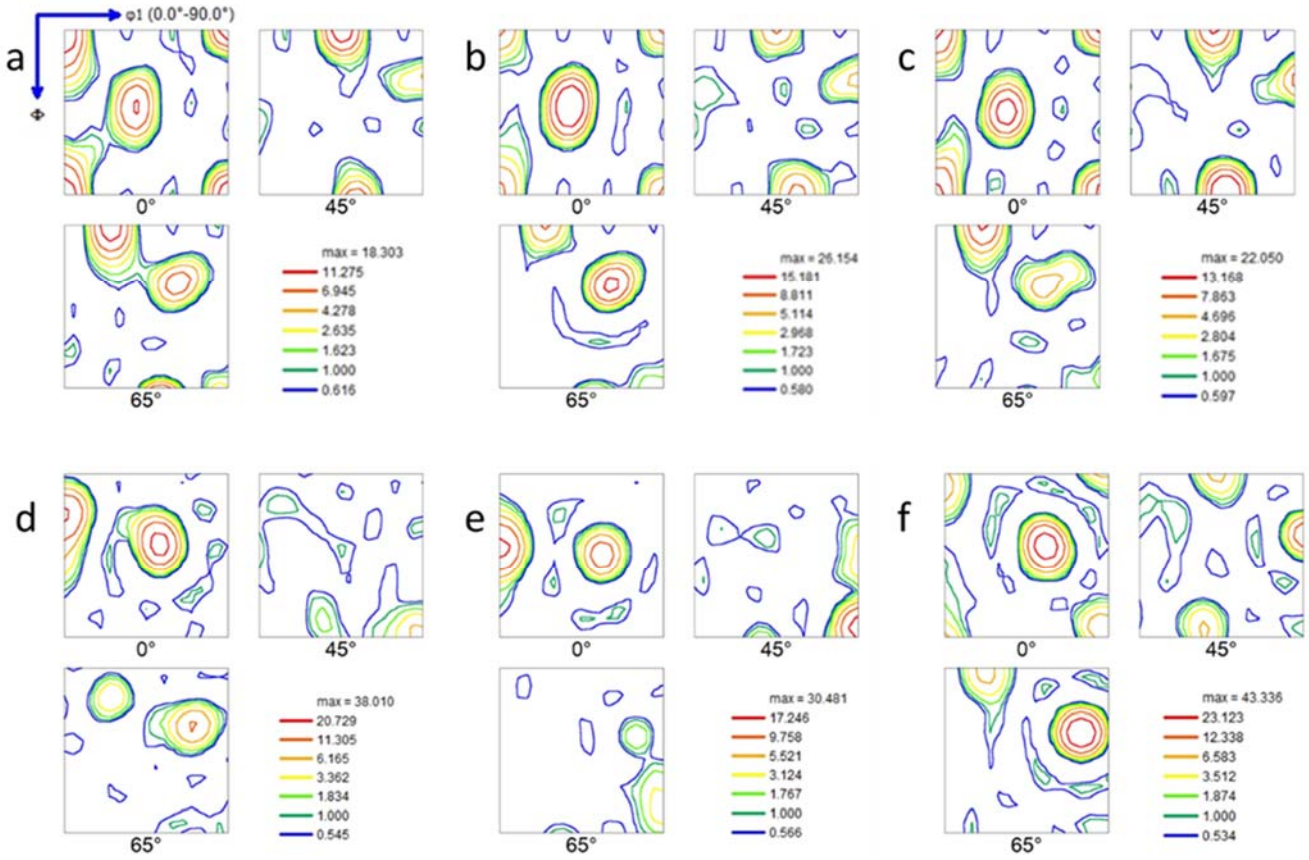

Fig 8.3 ODF sections (φ2 = 0°, 45° and 65°) of the flat bar after a) pre-ageing, b) stretching and c) post-ageing and the medium round bar after d) pre-ageing, e) stretching and f) post ageing.

Table 8.2 Volume fraction of the main texture components after each step of aDA.

Sample	Brass {110}<112>	Copper {112}<111>	S {123}<634>	Cube {001}<100>	Goss {011}<100>	CG26.5 {021}<100>	P {011}<122>
Flat bar Pre-aged	17	2.7	30	16.8	0.2	12.8	-
Flat bar Stretched	32	6.8	33	10	0.7	5.6	-
Flat bar Post-aged	33	9.5	21	16.3	0.4	5.3	-
Round bar Pre-aged	R(20^{o})29.9	5.7	1.948	0.5	6.4	8.688	0.1
Round bar Stretched	R(20^{o})11	29.6	0.1	0.1	20.8	12.8	3.1
Round bar Post-aged	R(20^{o})24.8	32.3	2.9	0.2	0.1	3.4	7.5

8.4 Mechanical properties of extrusion subjected to various stages of aDA process

The yield strength of the medium round bar was in general higher than that of the flat bar after each stage of aDA process, as shown in Fig 8.4. At the pre-aged stage, the yield strength of medium round bar was found to be 288.66 ± 3.64 MPa as compared to the flat bar with a yield strength of 237.02 ± 1.32 MPa. After stretching, the yield strength of medium round bar and flat bar increased to 384.47 ± 7.45 MPa and 328.75 ± 0.43 MPa, respectively. After post-aging, the yield strength of medium round bar and flat bar increased again to 432.65 ± 0.72 MPa and 409.53 ± 0.84 MPa, respectively. Overall, for both profiles, the improvement of strength from stage to stage in aDA was similar (80-95 MPa). However, the strength improvement (48.2 MPa) of the round bar was the least when comparing the stretching and post-aging stage. The yield strength of both profiles after aDA was found to be higher than after T6 treatment (180 ºC for 12 h), with increase of 6.01% and 12.94% for the medium round bar and flat bar respectively. In addition, the yield strength of T4 condition is also presented in Fig 8.4.

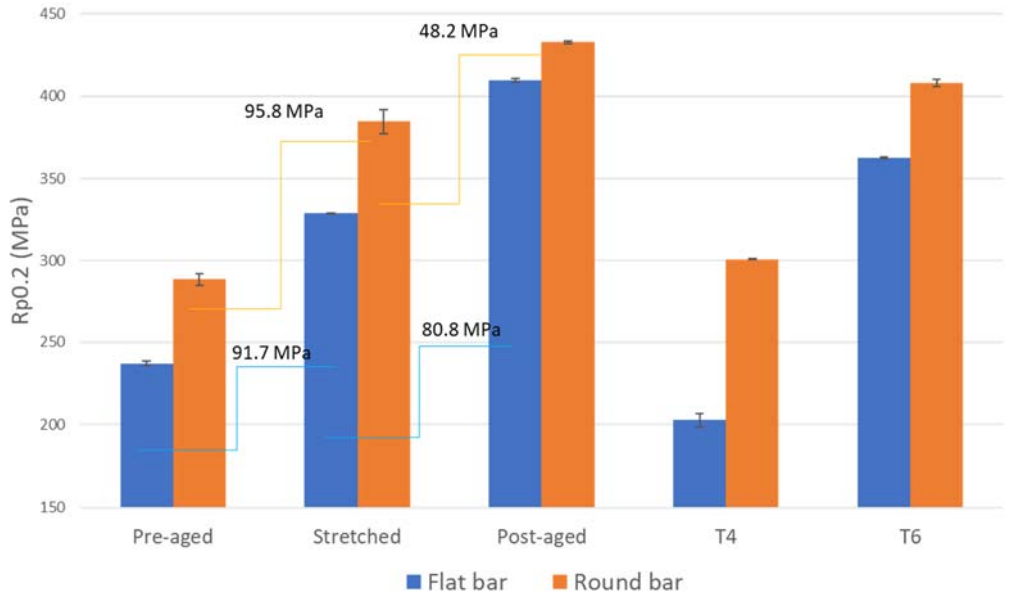

Fig 8.4 Yield strength of flat and round bar after the pre-aging, stretching, post-aging and comparison with T4 and T6 condition.

8.5 Discussion

As shown in Table 8.1, the grain morphology did not change significantly during the different aDA steps, for both extruded shapes, with the grains remaining elongated through the extrusion direction. However, the grain size had a decrease after stretching, 19.17% and 34.5% for flat and round bar respectively. After the final aging the grain size increased by 5.16% and 29.17% for flat and round bar respectively. During stretching the grains elongate further through the extrusion direction, which is the same direction of stretching and naturally the mean grain size will reduce. After the final ageing the mean grain size will increase due to grain growth and reduction of work hardening. Also, after the full aDA an increase of the HAGB by 11.41% and 17.05% for the flat and round bar respectively, and a decrease of the LAGB by 21.24% and 29.1%.

Based on the previously presented results the flat bar had a Brass-S-Cube texture, which didn't change during the thermomechanical processing. The investigation of the HAGB and LAGB showed that after the stretching both new grains and sub-grains were formed. Moreover, after the final heat treatment the amount of the LAGB decreased by 21.24%, indicating a reduction of recrystallization, while a 11.41% increase of the HAGB was reported.

During the stretching part of the aDA severe deformation was introduced, activating the multiple {111}<110> slip system of FCC aluminium matrix. Consequently, the evolution of Brass {110}<112> texture was amplified. That was reflected to the volume fraction of Brass that almost doubled from the pre-aging to the after stretching step. Severe deformation (hot rolling) has been reported to enhances Brass component, by rotating other orientations towards Brass [111-114].

The heat treatments activate the dislocations, formed both during extrusion and stretching, to start moving and cross-slip. This activate the recovery and recrystallization, which might enhances the {100}<001> texture.

The round bar had a strong, extruded Brass-Cu texture, during the whole thermomechanical processing. After the stretching the HAGB had a small decrease (4.91%), while the LAGB increased by 39% indicating the formation of recrystallized grains and sub-grains. After the final heat treatment, the HAGB increased by 17.05% and the LAGB decreased by 2.1% suggesting grain growth.

Brass texture component showed a 63% decrease from pre-aging step to stretched. At the same time Goss increased by 3.25 times. Wang et al. reported similar

transformation of Brass component into Goss with the increase of deformation [115]. Copper increased by 5.19 times.

Yang et al. showed that for an extruded Al-Mg-Si-Cu sheet, LAGB were increased with Brass {110}<112> texture component while for the HABG Cube {100}<001> texture component was mainly responsible [116]. A similar trend is not clear in our case. The observed Cube fibre, mainly Goss and CG26.5, should be attributed to the lower deformation at the centre of the round bar. This comes in agreement with other studies [117,118].

For both profiles, the formation of dislocations after stretching was beneficial for the strength. Similar improvement of mechanical properties after deformation has been reported for aluminium alloys [115,119]. For both profiles the increase of yield strength seemed to be linear, 80-95 MPa improvement after each step. Only for the final aging step of the round bar the yield strength increase was lower, 48.2 MPa. The lower improvement of round bar's strength can be attributed to the presence of recrystallization P {011}<122> component. P component exhibits high Δr values (planar anisotropy) [120]. The drop of Brass's volume fraction and increase of Goss after the stretching did not reflect on the yield strength. This was attributed to the important increase (5.2 times) of Copper component.

8.6 Conclusions

- The two profiles exhibited different texture, which overall remained similar after each aDA step. The flat bar had Brass-S and Cube fibre texture, while the round Brass-Copper.
- After stretching, Brass component had a different reaction for the two profiles. For the flat bar, Brass volume fraction increased by 88%, while for round bar decreased by 63%.
- For the round bar after stretching, the initial predominant Brass component transformed into Goss, and Copper increased by 5.2 times.

Chapter 9 Conclusions and further work

9.1 Conclusions

1. The extrusion exit temperature was found to have an effect on microstructure, texture, and tensile properties. The average grain size increased as the exit speed and temperature increased and resulted to tensile strength improvement. The overall texture was not affected by the speed change but, a significant increase of S and decrease of Cube fibre volume fractions was noticed by increasing the extrusion speed.

2. The extrusion geometry significantly affected the texture. Between four profiles with different geometries and extrusion ratios, a grouping of those with high ER and those with low ER was achieved, both for microstructure and texture. The high ER profiles exhibited thin elongated grains, with a lot of recrystallization, while the low ER profiles exhibited a microstructure with thick grains and areas of recrystallization.

3. The profiles with high ER had Brass-S-Cube fibre texture, while the low ER profiles Copper-Brass-Cube fibre. The strong Copper component of the low ER profiles enhanced the tensile properties of these profiles, which exhibited maximum 45 MPa difference of yield strength from the high ER.

4. For a given round profile, the average grain size as a function of ER increased from high ER to similar size for both medium and low ER. Different strain and temperature distributions resulted to these changes.

5. For a given round profile, ER did not significantly affect the overall texture. All the three round bars exhibited strong <111> and <100> fibre texture, with Copper being the predominant texture component. However, the amount of <111> increased at the expense of Cube <100> fibre texture with increasing ER.

6. Between the three round bars, with different ER small changes of mechanical properties were noticed. That comes in agreement with the texture observations.

7. Between ER and geometry, the latter one was found to affect stronger the microstructure and texture. A small round bar and a flat bar, with similar ER, showed different grain size and texture. Specifically, rolling texture of Brass-S-Cube was found in flat bar and extrusion texture of Cu-Brass-Cube was found in small round bar.

Moreover, a 41 MPa difference was noticed between the stronger round bar and the flat bar, which comes in agreement with the texture differences.

8. From the investigation of a complex profile it was shown that texture is not a solely indicator of the mechanical properties. Top and bottom sides consisted of a mixture of deformation (Brass-S-Copper) and recrystallisation texture (Cube-Goss-GC), while the right- and left-hand side fins consisted of only deformation texture (Brass-S-Copper). At the same time top and bottom had slightly higher average grain size. Strength was found to be higher for top and bottom, regardless the higher amount of recrystallization.

9. The effect of aDA on the mechanical properties cannot be attributed to crystallographic texture. It was shown that texture underwent over small changes after each step of aDA, with the most critical for texture being the deformation part.

9.2 Further work

9.2.1 Shape complexity

Many extrusion variables of simply geometries were studied in the current work. In industry more complex profiles are produced. Shape complexity factor is correlated to the metal flow, die and tooling design and the extrusion parameters already studied here. Investigation of shape complexity factor can give as a better understanding of microstructure and texture relationship with mechanical properties and boost productivity and high quality of products.

9.2.2 Hardness cross-section maps

The deviation of texture through cross-section was studied in this work. Hardness maps of the cross-sections can give a better correlation of local texture components and mechanical properties variation within a given extrusion profile.

9.2.3 Simulation of strain path and distribution modelling

Further to hardness maps, modelling can enhance the understanding of texture development. Moreover, simulation of strain paths could explain the differences in material flow, hence the different microstructure and texture of different profiles.

9.2.3 Dispersoids analysis

The investigation of the chemical composition was not included in this study. Dispersoids have an important role in recrystallization and texture development of 6xxx Al alloys. This role could be investigated. The types of dispersoids and their distribution can be studied with transmission electron microscopy (TEM).

9.2.5 Synchrotron X-ray and neutron diffraction

Neutron diffraction and synchrotron X-ray are the state-of-the-art techniques for texture measurement. With these techniques a quantitative, non-distractive, characterization of texture can be achieved. Its one has different characteristics, making them useful in different occasions. For large samples and materials with large grains neutron diffraction is preferred while for small samples and in situ experiments synchrotron diffraction. Neutron diffraction could be used for texture characterization of larger parts of the extruded products, avoiding any material's preparation interference.

References

[1] S. Kalpakjian, S. R. Schmid, Manufacturing Engineering and Technology, 6th ed., Pearson Ed Asia, 2009.

[2] J. Hirsch, Recent development in aluminium for automotive applications, Trans. Nonferrous Met. Soc. China, 24 (2017) 1995–2002. https://doi.org/10.1016/S1003-6326(14)63305-7

[3] P. Mukhopadhyay, Alloy Designation, Processing, and Use of AA6XXX Series Aluminium Alloys, ISRN Metall. 2012, (2012) 1–15. https://doi.org/10.5402/2012/165082

[4] J. Hirsch, T. Al-Samman, Superior light metals by texture engineering: Optimized aluminum and magnesium alloys for automotive applications, Acta Mater. 61 (2013) 818–843. https://doi.org/10.1016/j.actamat.2012.10.044

[5] B. Simhachalam, K. Srinivas,C. L. Rao, Energy absorption characteristics of aluminium alloy AA7XXX and AA6061 tubes subjected to static and dynamic axial load, Int. J. Crashworthiness, 19 (2014) 139-152. https://doi.org/10.1080/13588265.2013.878974

[6] H. Ford, Aluminium in cars. Unlocking the light-weighting potential.

[7] Ducker Frontier, 2020 North America Vehicle Aluminum Content. https://1pp2jy1h0dtm6dg8i11qjfb1-wpengine.netdna-ssl.com/wp-content/uploads/2020/08/DuckerFrontier-Aluminum-Association-2020-Content-Study-Summary-Report-FINAL.pdf

[8] O. Engler and V. Randle, Introduction to Texture Analysis, Macrotexture, Microtexture, and Orientation Mapping, 2nd ed., CRC Press, 2009.

[9] I. J. Polmear, Light Alloys, Metallurgy of the Light Metals, 4th ed., Butterworth-Heinemann, 2005.

[10] D. G. Eskin, J. Mi, Solidification Processing of Metallic Alloys Under External Fields, 1st ed. (2018).

[11] R. Nadella, D.G. Eskin, Q. Du, L. Katgerman, Macrosegregation in direct-chill casting of aluminium alloys, Progr. Mater. Sc. 53 (2008) 421-480. https://doi.org/10.1016/j.pmatsci.2007.10.001

[12] D.G. McCartney, Grain Refining of Aluminium and Its Alloys Using Inoculants, Int. Mater. Reviews, 34 (1989) 247-260. http://dx.doi.org/10.1179/imr.1989.34.1.247

[13] T. Sheppard, Extrusion of Aluminium Alloys. Springer US, (1999).

[14] S. Støren, The theory of extrusion-Advances and challenges, Int. J. Mech. Sci., 35 (1993) 1007–1020. https://doi.org/10.1016/B978-0-444-89991-0.50016-0
[15] K. Huang, R. E. Logé, A review of dynamic recrystallization phenomena in metallic materials, JMADE, 111 (2016) 548–574. http://dx.doi.org/10.1016/j.matdes.2016.09.012
[16] K. K. Alaneme, E. A. Okotete, Recrystallization mechanisms and microstructure development in emerging metallic materials: A review, Journal of Science: Advanced Materials and Devices, 4 (2019) 19-33. https://doi.org/10.1016/j.jsamd.2018.12.007.
[17] F.J. Humphreys, M. Hatherly, Recrystallization and Related Annealing Phenomena, 2nd ed., Elsevier Science Ltd., 2004.
[18] X. W. Chen, Y. Y. Fan, Texture evolution of 01570 aluminum alloy sheet, IOP Conf. Ser. Mater. Sci. Eng. 170 (2017) 120013. DOI:10.1088/1757-899X/170/1/012013
[19] M. Kuroda, Effects of Texture on Mechanical Properties of Aluminum Alloy Sheets and Texture Optimization Strategy, (2005) 445–450. https://doi.org/10.1063/1.2011260
[20] J. Hirsch, K. Lucke, Mechanism of Deformation and Development of Rolling Textures in Polycrystalline F.C.C. Metals. I. Description of Rolling Texture Development in Homogeneous CuZn Alloys, Acta metall. 36.11 (1988) 2863-2882.
[21] I. Dillamore, W. Roberts, Metall. Rev., (1965) 10, 271.
[22] I. G. Palmer, R. E. Lewis, D. D. Crooks, Proc. 1st Int. Conf. on Aluminium-lithium alloys, 241 (1981) The Metallurgical Society of AIME.
[23] R. Fortunier, J. H. Driver, Grain reorientations in rolled aluminum sheet: comparison with predictions of continuous constraints model. Acta Metall, (1987) 35 (6) 1355–1366.
[24] R. Fortunier, J. H. Driver, Continuous constraint model for large grain deformations. Acta Metall, (1987) 35(2) 509–517
[25] P. Lipinski, M. Berveiller, A. Hihi, P. Sainfort, P. Meyer, J. Phys. (Paris), (1987) 48, 677
[26] S. Fox, D. S. McDarmaid, H. M. Flower, Aluminium Technology (1986), 327 London, The Institute of Metals.
[27] A. K. Vasudevan, W. G. Fricke, M. A. Pryztupa, S. Panchanadeeswaran, Textures of materials, Proc. ICOTOM8, (1988) The Metallurgical Society of AIME.
[28] H. Weiland, Microtexture determination and its application to materials science, JOM, 46 (1994) 37–41. https://doi.org/10.1007/BF03222581
[29] S. Suwas, R. K. Ray, Crystallographic Texture of Materials, Springer London, 2014.
[30] K. P. Shah, Means of Strengthening, (2018). http://practicalmaintenance.net/?p=1618.

[31] R. E. Smallman, A. H. W. Ngan, Chapter 4 - Introduction to Dislocations, Modern Physical Metallurgy (Eighth Edition), (2014) 121-158 https://doi.org/10.1016/B978-0-08-098204-5.00004-3.]
[32] S. V. Kailas, Material Science, Chapter 7. Dislocations Strength. Mech.
[33] N. Hansen, Hall-Petch relation and boundary strengthening, Scr. Mater. 51 (2004) 801–806. https://doi.org/10.1016/j.scriptamat.2004.06.002
[34] F. J. Humphreys, M. Hatherly, Recrystallization and Related Annealing Phenomena, 2nd ed., Pergamon, 2004.
[35] D. A. Porter, K. E. Easterling, Phase Tranformations in Metals and Alloys, 3rd ed. CRC Press, 2009.
[36] E. Hornbogen, Hundred years of precipitation hardening, J. Light Met. 1 (2001) 127–132. https://doi.org/10.1016/S1471-5317(01)00006-2
[37] O. Pekguleryuz, K. U. Kainer, A. A. Kaya, Fundamentals of magnesium alloy metallurgy, 1st ed., Woodhead, 2013.
[38] S. Pogatscher, H. Antrekowitsch, H. Leitner, D. Pöschmann, Z. L. Zhang, P. J. Uggowitzer, Influence of interrupted quenching on artificial aging of Al–Mg–Si alloys, Acta Mater. 60 (2012) 4496–4505. https://doi.org/10.1016/j.actamat.2012.04.026
[39] L. K. Murty, C. Indrajit, An Introduction to Nuclear Materials: Fundamentals and Applications, John Wiley & Sons, 2013.
[40] C. D. Marioara, S. J. Andersen, T. N. Stene, H. Hasting, J. Walmsley, A. T. J. Van Helvoort, R. Holmestad, The effect of Cu on precipitation in Al–Mg–Si alloys, Philos. Mag. 87 (2007) 3385–3413. https://doi.org/10.1080/14786430701287377
[41] M. Werinos, H.Anterkowitsch, T Ebner, R, Prillhofer W. A. Curtin, P. J. Uggowitzer, S. Pogatscher, Design strategy for controlled natural aging in Al–Mg–Si alloys, Acta Mater. 118 (2016) 296–305. https://doi.org/10.1016/j.actamat.2016.07.048
[42] J. G. Kaufman, Understanding Wrought and Cast Aluminum Alloys Designations, Intr. to Alum. Alloy. Tempers, (2000) 23–37, 2000. DOI:10.1361/iaat2000p023
[43] S. A. Court, H. D. Dundfeon, Improved performance in Al-Mg-Si (6xxx) extruded, structural alloys through microstructural control, Advances, 88 (2008) 179–180.
[44] S. C. Wang, M. J. Starink, Precipitates and intermetallic phases in precipitation hardening Al–Cu–Mg–(Li) based alloys, Int. Mater.Reviews, 50:4 (2005) 193-215. DOI: 10.1179/174328005X14357
[45] Y. J. Li, S. Brusethaug, A. Olsen, Influence of Cu on the mechanical properties and precipitation behavior of AlSi7Mg0.5 alloy during aging treatment, Scr. Mater. 54 (2006) 99–103. https://doi.org/10.1016/j.scriptamat.2005.08.044

[46] M. Murayama, K. Hono, W. F. Miao, and D. E. Laughlin, The effect of Cu additions on the precipitation kinetics in an Al-Mg-Si alloy with excess Si, Metall. Mater. Trans. A. 32 (2001) 239–246. https://doi.org/10.1007/s11661-001-0254-z

[47] D. Chakrabarti, D. Laughlin, Phase relations and precipitation in Al–Mg–Si alloys with Cu additions, Prog. Mater. Sci. 49 (2004) 389–410. doi:10.1016/S0079-6425(03)00031-8

[48] A. Sverdlin, Properties of Pure Aluminum, Handb. Alum. Vol.1 - Phys. Metall. Process. (2003) 33–79.

[49] V. Fallah, A. Korinek, N. Ofori-Opoku, B. Raeisinia, M. Gallerneault, N. Provatas, S. Esmaeili, Atomic-scale pathway of early-stage precipitation in Al–Mg–Si alloys, Acta Mater. 82 (2015) 457–467. 1407.6412

[50] S. Esmaeili, X. Wang, D. J. Lloyd, W. J. Poole, On the precipitation-hardening behavior of the Al−Mg−Si−Cu alloy AA6111, Metall. Mater. Trans. A. 34 (2003) 751–763. 10.1007/s11661-003-1003-2

[51] L. Ding, Z. Jia, Y. Liu, Y. Weng, Q. Liu, The influence of Cu addition and pre-straining on the natural aging and bake hardening response of Al-Mg-Si alloys, J. Alloys Compd. 688 (2016) 362–367. http://dx.doi.org/10.1016/j.jallcom.2016.07.066

[52] J. Buha, R. N. Lumley, A. G. Crosky, Precipitation and solute distribution in an interrupted-aged Al-Mg-Si-Cu alloy, Philos. Mag. 88 (2008) 373–390. 10.1080/14786430701847949

[53] Z. Wang, H. Li, F. Miao, B. Fang, R. Song, Z. Zheng, Improving the strength and ductility of Al–Mg–Si–Cu alloys by a novel thermo-mechanical treatment, Mater. Sci. Eng. A. 607 (2014) 313–317. https://doi.org/10.1016/j.msea.2014.04.009

[54] M. Murayama, K. Hono, Pre-precipitate clusters and precipitation processes in Al-Mg-Si alloys, Acta Mater. 47 (1999) 1537–1548. https://doi.org/10.1016/S1359-6454(99)00033-6

[55] A. K. Gupta, D. J. Lloyd, S. A. Court, Precipitation hardening in Al–Mg–Si alloys with and without excess Si, Mater. Sci. Eng. A. 316 (2001) 11–17. https://doi.org/10.1016/S0921-5093(01)01247-3

[56] A. Perovic, D. Perovic, G. Weatherly, D. Lloyd, Precipitation in aluminum alloys AA6111 and AA6016, Scr. Mater. 41 (1999) 703–708. 10.1016/s1359-6462(99)00204-3

[57] S. Pogatscher, H. Antrekowitsch, M. Werinos, F. Moszner, S. S. A. Gerstl, M. F. Francis, W. A. Curtin, J. F. Löffler, P. J. Uggowitzer, Diffusion on Demand to Control Precipitation Aging: Application to Al-Mg-Si Alloys, Phys. Rev. Lett. 112 (2014) 225701. https://doi.org/10.1103/PhysRevLett.112.225701

[58] Z. Jia, L. Ding, Y. Weng, Z. Wen, and Q. Liu, Effects of high temperature pre-straining on natural aging and bake hardening response of Al-Mg-Si alloys, Trans. Nonferrous Met. Soc. China, 26 (2016) 924–929.

[59] K. Teichmann, C.D. Marioara, S.J. Andersen, K.O. Pedersen, S. Gulbrandsen-Dahl, M. Kolar, R. Holmestad, K. Marthinsen, HRTEM study of the effect of deformation on the early precipitation behaviour in an AA6060 Al–Mg–Si alloy, Philos. Mag. 91 (2011) 3744–3754. https://doi.org/10.1080/14786435.2011.593577

[60] J. D. Bryant, The effects of preaging treatments on aging kinetics and mechanical properties in AA6111 aluminum autobody sheet, Metall. Mater. Trans. A, 30 (1999) 1999–2006. https://doi.org/10.1007/s11661-999-0010-3

[61] Y. Birol, Reversion treatment to improve bake hardening response of a twin-roll cast 6016 automotive sheet, 5th Int. Conf. Process. Manuf. Adv. Mater. THERMEC2006, 539–543 (2007) 345–350 2007. DOI:10.4028/www.scientific.net/MSF.539-543.345

[62] P. Trivedi, D. P. Field, and H. Weiland, Alloying effects on dislocation substructure evolution of aluminum alloys, Int. J. Plast. 20 (2004) 459–476. 10.1016/S0749-6419(03)00097-4

[63] B. Mirzakhani, Y. Payandeh, Combination of sever plastic deformation and precipitation hardening processes affecting the mechanical properties in Al–Mg–Si alloy, Mater. Des. 68, (2015) 127–133. DOI:10.1016/j.matdes.2014.12.011

[64] J. A. Österreicher, A. Schiffl, G. Falkinger, and G. R. Bourret, Microstructure and mechanical properties of high strength Al-Mg-Si-Cu profiles for safety parts, IOP Conf. Ser. Mater. Sci. Eng.119 (2016) 120-128. DOI:10.1088/1757-899X/119/1/012028

[65] O. Engler, C. Schäfer, O. R. Myhr, Effect of natural ageing and pre-straining on strength and anisotropy in aluminium alloy AA 6016, Mater. Sci. Eng. A. 639 (2015) 65–74. https://doi.org/10.1016/j.msea.2015.04.097

[66] K. O. Pedersen, O.-G. Lademo, T. Berstad, T. Furu, and O. S. Hopperstad, Influence of texture and grain structure on strain localisation and formability for AlMgSi alloys, J. Mater. Process. Technol. 200 (2008) 77–93. doi:10.1016/j.jmatprotec.2007.08.040

[67] C. M. Cepeda-Jiménez, P. Hidalgo, M. Carsí, O. A. Ruano, and F. Carreño, Microstructural characterization by electron backscatter diffraction of a hot worked Al–Cu–Mg alloy, Mater. Sci. Eng. A. 528 (2011) 3161-3168.
https://doi.org/10.1016/j.msea.2010.12.045

[68] C. Zhang, G. Zhao, Z. Chen, H. Chen, F. Kou, Effect of extrusion stem speed on extrusion process for a hollow aluminum profile, Mater. Sci. Eng. B. 177 (2012) 1691-1697. https://doi.org/10.1016/j.mseb.2011.09.041.

[69] I. Flitta, T. Sheppard, Effect of pressure and temperature variations on FEM prediction of deformation during extrusion, Mater. Sc. and Tech. 21:3 (2005) 339-346, DOI: 10.1179/174328405X29221

[70] S. Kaneko, K. Murakami, T. Sakai, Effect of the extrusion conditions on microstructure evolution of the extruded Al–Mg–Si–Cu alloy rods, Mater. Sci. Eng. A. 500 (2009) 8–15, https://doi.org/10.1016/j.msea.2008.09.057

[71] S.S. Park, B.S. You, D.J. Yoon, Effect of the extrusion conditions on the texture and mechanical properties of indirect-extruded Mg–3Al–1Zn alloy, Journal of Mater. Proc. Tech. 209 (2009) 5940-5943. 10.1016/j.jmatprotec.2009.07.012

[72] S. Karabay, M. Zeren, M. Yilmaz, Investigation extrusion ratio effect on mechanical behaviour of extruded alloy AA-6063, Jour. of Mater. Proc. Tech., 135 (2003) 101-108. https://doi.org/10.1016/S0924-0136(02)01110-X.

[73] A. Aytaç, B. Daşçılar, M. Usta, The effect of extrusion speed on the structure and corrosion properties of aged and non-aged 6063 aluminum alloy, Mater. Chem. and Ph. 130 (2011) 1357-1360. 10.1016/j.matchemphys.2011.09.029

[74] S. N. Ab Rahim, M. A. Lajis, S. Ariffin, Effect of extrusion speed and temperature on hot extrusion process of 6061 aluminum alloy chip, ARPN Journal of Eng. and Appl. Sc. 11 (2016) 2272-2277.

[75] C. Zhang, C. Wang, Q. Zhang, G. Zhao, L. Chen, Influence of extrusion parameters on microstructure, texture, and second-phase particles in an Al-Mg-Si alloy, Journal of Mater. Proc. Tech. 270 (2019) 323-334. https://doi.org/10.1016/j.jmatprotec.2019.03.014.

[76] X. Wang, T. Shi, Z. Jiang, W. Chen, M. Guo, J. Zhang, L. Zhuang, Y. Wang, Relationship among grain size, texture and mechanical properties of aluminums with different particle distributions, Mater. Sci. Eng. A. 753 (2019) 122 134. https://doi.org/10.1016/j.msea.2019.03.034.

[77] L. Zhang, Y. Wang, X. Yang, K. Li, S. Ni, Y. Du, M. Song, Texture, Microstructure and Mechanical Properties of 6111 Aluminum Alloy Subject to Rolling Deformation, Mat. Res. 20 (2017)
https://doi.org/10.1590/1980-5373-MR-2017-0549

[78] S. Mishra, M. Kumar, A. Singh, Evolution of rotated Brass texture by cross rolling: implications on formability, Mater. Sc. and Tech., 36:12, (2020) 1272-1281, DOI: 10.1080/02670836.2020.1773036

[79] G. Tempus, W. Calles, G. Scharf, Influence of extrusion process parameters and texture on mechanical properties of Al-Li extrusions, Mater. Sc. Tech. 7:10 (1991) 937-946. https://doi.org/10.1179/mst.1991.7.10.937

[80] S-H. Hong, D. N. Lee, The evolution of the cube recrystallization texture in cold rolled copper sheets, Mater. Sci. Eng. A. 351 (2003) 133-147. https://doi.org/10.1016/S0921-5093(02)00834-1
[81] G. E. Dieter, D. J. Bacon, Mechanical metallurgy, London: McGraw-Hill, 1988.
[82] OIM Analysis Tutorial
[83] L. Saraf, Kernel Average Misorientation Confidence Index Correlation from FIB Sliced Ni-Fe-Cr alloy Surface. Microscopy and Microanalysis, 17(S2) (2011) 424-425. doi:10.1017/S1431927611002996
[84] D. P. Field, P.B. Trivedi, S. I. Wright, M. Kumar, Analysis of local orientation gradients in deformed single crystals. Ultramicroscopy,103(1) (2005) 33–39. https://doi.org/10.1016/j.ultramic.2004.11.016
[85] J. Wang, X. Yuan, J. Peipeng, Z. Yunpeng, L. Mingyue, The influence of extrusion temperature on the structures and mechanical properties of Mg–Al–4Y alloys, Mater. Res. Expr. 7 (2020). Mater. Res. Express. DOI:10.1088/2053-1591/aba217
[86] F.J. Humphreys, M. Hatherly, Recrystallization and related annealing phenomena, 2nd ed., Oxford: Pergamon, 2004.
[87] L. Donati, A. Segatori, M. El Mehtedi, L. Tomesani, Grain evolution analysis and experimental validation in the extrusion of 6XXX alloys by use of a lagrangian FE code, Intern. Journal of Plasticity. 46 (2013) 70-81. 10.1016/j.ijplas.2012.11.008
[88] F. Parvizian, A. Jäger, H-G. Lambers, B. Svendsen, A. Tekkaya, H. Maier, Modeling of dynamic microstructure evolution of EN AW-6082 alloy during hot forward extrusion, Comp. Mater. Science. 50 (2011)1520-1525. 10.1016/j.commatsci.2010.12.009.
[89] X. Duan, X. Velay, T. Sheppard, Application of finite element method in the hot extrusion of aluminium alloys. Mater. Sci. Eng. A. 369 (2004) 66-75. DOI:10.1016/j.msea.2003.10.275
[90] H.O. Asbeck, H. Mecking, Influence of friction and geometry of deformation on texture inhomogeneities during rolling of Cu single crystals as an example, Mater. Sci. Eng. 34 (1978) Pages 111-119. https://doi.org/10.1016/0025-5416(78)90041-1
[91] H. Inoue, N. Nakazu, H. Yamamoto, Development of recrystallization texture in drawn aluminum wire, Nagashima S., Proceedings ICOTOM 6 Tokyo, Japan: The Iron and Steel Institute of Japan. (1981) 591
[92] D. N. Lee, Y. H. Chung, M. C. Shin, Preferred orientation in extruded aluminun alloy rod, Scripta Metall. 17 (1983) 339-342. https://doi.org/10.1016/0036-9748(83)90169-2.
[93] F. Barlat, Crystallographic texture, anisotropic yield surfaces and forming limits of sheet metals, Mater. Sci. Eng. 91 (1987) 55-72. https://doi.org/10.1016/0025-5416(87)90283-7.

[94] J. Dickson, T. Sanders, Crystallographic texture development in extruded AA 2195 and AA 7075. Mat. Charact. 160 (2020) 110-121. 10.1016/j.matchar.2020.110121.
[95] J. Jung, J. I. Yoon, D. N. Lee, H. S. Kim,Numerical analysis on the formation of P-orientation near coarse precipitates in FCC crystals during recrystallization, Acta Mater. 131 (2017) 363-372, https://doi.org/10.1016/j.actamat.2017.04.020.
[96] K. Huang, K. Zhang, K. Marthinsen, R.E. Logé, Controlling grain structure and texture in Al-Mn from the competition between precipitation and recrystallization, Acta Mater. 141 (2017) 360-373, https://doi.org/10.1016/j.actamat.2017.09.032.
[97] Y. Hu, Z. Liu, Q. Zhao, S. Bai, F. Liu, P-Texture Effect on the Fatigue Crack Propagation Resistance in an Al-Cu-Mg Alloy Bearing a Small Amount of Silver, Materials. (2018) 11 2481. https://doi.org/10.3390/ma11122481
[98] M. Khadyko, S. Dumoulin, O.S. Hopperstad, Texture gradients and strain localisation in extruded aluminium profile, Inter.l Journal of Solids and Struct.,97–98 (2016) 239-255. https://doi.org/10.1016/j.ijsolstr.2016.07.024.
[99] Y. Wu, H. Liao, K. Zhou, J. Yang, Effect of texture evolution on mechanical properties of near eutectic Al–Si–Mg alloy with minor addition of Zr/V during hot extrusion, Materials & Design. 57 (2014) 416-420. https://doi.org/10.1016/j.matdes.2013.12.068.
[100] D. N. Lee, The evolution of recrystallization textures from deformation textures, Scripta Metall. Mater. 32 (1995) 1689-1694, https://doi.org/10.1016/0956-716X(95)00256-U.
[101] D. N. Lee, H. N. Han, Recrystallization Textures of Metals and Alloys, http://dx.doi.org/10.5772/54123
[102] A. Godfrey, D. Juul Jensen, N. Hansen, Measurement of orientation dependent stored energy of deformation on a local scale. In G. Gottstein, & D. A. Molodov (Eds.), Recrystallization and grain growth. Proceedings. Springer Verlag, 2 (2001) 843-848.
[103] G. Gottstein, D.A. Molodov, Recrystallization and Grain Growth Springer-Verlag (2001).
[104] D.N. Lee, Relationship between deformation and recrystallisation textures of fcc and bcc metals, Phil. Mag. 85 (2005) 297–322. 10.1080/14786430412331315734
[105] S. Z. Qamar, J. C. Chekotu, S. B. Qamar, Effect of Shape Complexity on Ram Pressure and Metal Flow in Aluminum Extrusion, JOM. 71(12) (2019) 4378-4392. https://doi.org/10.1007/s11837-019-03748-6
[106] K. Laue, H. Stenger, Extrusion: Processes, Machinery, Tooling, 1st ed., AMS Intern., 1981.

[107] S. Z. Qamar, J. C. Chekotu, M. Al-Maharbi, Shape Complexity in Metal Extrusion: Definitions, Classification, and Applications. Arab J Sci Eng. 44 (2019)7371–7384. https://doi.org/10.1007/s13369-019-03886-8

[108] T. Kayser, B. Klusemann, H. G. Lambers, H. J. Maier, B. Svendsen, Characterization of grain microstructure development in the aluminum alloy EN AW 6060 during extrusion. Mater. Sc. and Eng. A, Struct. Mater.: Prop., Microstr. and Proces. 527 (24-25) (2010) 6568-6573. doi:101016/jmsea201006050

[109] L. Donati, L. Tomesani, Grain Size Prediction in AA6060 Profile Extrusion.

[110] M. Schikorra, L. Donati, L. Tomesani, A. Tekkaya, Microstructure analysis of aluminum extrusion: Grain size distribution in AA6060, AA6082 and AA7075 alloys, Journal of Mech. Sc. and Tech. 21 (2007) 1445-1451. 10.1007/BF03177357.

[111] W.C. Liu, J.G. Morris, Effect of hot and cold deformation on the b fiber rolling, Scripta Materialia. 52 (2005) 1317–1321.
https://doi.org/10.1016/j.scriptamat.2005.02.031.

[112] A. Duckham, R. D. Knutsen, O. Engler, Influence of deformation variables on the formation of copper-type shear bands in Al–1Mg, Acta Mater. 49(14) (2001) 2739–2749. https://doi.org/10.1016/S1359-6454(01)00166-5

[113] G Sarma, B. Radhakrishnan, T. Zacharia, Modelling the deformation of face centred cubic crystals to study the effect of slip on {110} planes, Modelling Simul. Mater. Sci. Eng. 7 (1999) 1025. https://doi.org/10.1088/0965-0393/7/6/308

[114] P.S Bate, Y Huang, F.J Humphreys, Development of the “brass” texture component during the hot deformation of Al–6Cu–0.4Zr, Acta Mater. 52 (2004) 4281-4289. https://doi.org/10.1016/j.actamat.2004.05.044.

[115] Y. Wang, L. Zhang, X. Yang, K. Li, S. Ni, Y. Du, M. Song, Texture/Microstructural Evolution and Mechanical Properties of a Hot and Cold Rolled Al-Mg-Si-Cu Alloy. Journal of Minerals and Materials Characterization and Engineering. 05 (2017) 209-222. 10.4236/jmmce.2017.54018.

[116] W. Yang, Z. Li, M. Wang, Grain boundary precipitation induced by grain crystallographic misorientations in an extruded Al–Mg–Si–Cu alloy, Journal of Alloys and Compounds 624 (2015) 27-30. 10.1016/j.jallcom.2014.10.206.

[117] X. Wang, M. X. Guo, L. CAO, J. LUO, J. ZHANG, L. Zhuang, Linzhong, Influence of thermomechanical processing on microstructure, texture evolution and mechanical properties of Al-Mg-Si-Cu alloy sheets, Transactions of Nonferrous Metals Society of China (English Edition) 25 (2015) 1752-1762. 10.1016/S1003-6326(15)63780-3.

[118] O. Engler, K. Lücke, Mechanisms of recrystallization texture formation in aluminium alloys. Scripta Metall. Mater. 27(11), (2003) 1527–1532. https://doi.org/10.1016/0956-716X(92)90139-6

[119] Y. Lang, G. Zhou, L. Hou, J. Zhang, L. Zhuang, Significantly enhanced the ductility of the fine-grained Al-Zn-Mg-Cu alloy by strain-induced precipitation. Materials & Design. 88 (2015) 10.1016/j.matdes.2015.09.023.
[120] J. Sidor, A. Miroux, R. Petrov, L. Kestens, Microstructural and crystallographic aspects of conventional and asymmetric rolling processes, Acta Mater. 56 (2008) 2495-2507. 10.1016/j.actamat.2008.01.042.